THERMOELASTICALLY ACTUATED ACOUSTIC PROXIMITY SENSOR WITH INTEGRATED ELECTRICAL THROUGH-WAFER INTERCONNECTS

By

VENKATARAMAN CHANDRASEKARAN

A DISSERTATION PRESENTED TO THE GRADUATE SCHOOL
OF THE UNIVERSITY OF FLORIDA IN PARTIAL FULFILLMENT
OF THE REQUIREMENTS FOR THE DEGREE OF
DOCTOR OF PHILOSOPHY

UNIVERSITY OF FLORIDA

2004

To my parents and my wife, Anu.

ACKNOWLEDGEMENTS

Financial support for the project was provided by the Office of Naval Research (contract #N00014-00-1-0343) monitored by Dr. Kam Ng.

I would like to express my sincere gratitude to my advisor, Mark Sheplak, for giving me the opportunity to work at the Interdisciplinary Microsystems Group. His guidance over the years has been invaluable. His penchant for good quality research and his aggressive approach to it have had a very positive influence on me. I would like to thank Professors Toshikazu Nishida, Louis N. Cattafesta, Bhavani V. Sankar and Wei Shyy for their help and valuable insights on different aspects of this multidisciplinary project and for serving on my committee. I would also like to thank Professor David Hahn for his help with the thermal modeling.

My thanks go to all my colleagues at IMG over the past years, especially Anthony Cain, David Arnold, Stephen Horowitz, Sunil Bhardwaj, Karthik Kadirvel and Anurag Kasyap. It has been a pleasure to have worked with them. Their company made the innumerable hours spent at the lab a lot more interesting, memories of which I will carry for the rest of my life.

I would like to thank Mr. Ken Reed from TMR Engineering for his excellent and prompt services. His help in fabricating the experimental set-up and the sensor package is greatly appreciated.

I would like to thank Professor Thomas Kenny and his students, especially Eugene Chow, for all their help and insights during the fabrication of the sensors.

Most of all, I would like to thank my family. My parents have always wanted the best for me and their endless support and guidance throughout my life are beyond words and will always be cherished. I hope to fulfill all their dreams. I am forever grateful to my wife, Anu, for her love and understanding during my years as a graduate student. She continues to bring out the best in me.

TABLE OF CONTENTS

LIST OF TABLES

Table Page

LIST OF FIGURES

Figure page

LIST OF SYMBOLS

a	radius of the composite diaphragm
b	radius of the diffused resistive heater
H_i	axial distance from reference axis of the composite diaphragm
ω	angular frequency
$\bar{V}$	dc voltage (V)
V'	ac voltage (V)
R_{arc}, R_{taper}	total resistance of the arc and tapered piezoresistors under zero load conditions (Ω)
$\Delta R_{arc}, \Delta R_{taper}$	change in resistance of the arc and tapered piezoresistors (Ω)
E_{ij}	elastic moduli (N/m^2)
Q_{ij}	elements of the material stiffness matrix (N/m^2)
ν	Poisson's ratio
φ	degree of anisotropy
k	thermal conductivity (W/mK)
$\alpha = \frac{k}{\rho C_p}$	thermal diffusivity (m^2/sec)
∇^2	axisymmetric Laplacian operator
ε_m	radial-direction spatial eigenvalues (m^{-1})
λ_{nm}	temporal eigenvalues (s^{-1})
g_o	internal heat source (W/m^3)
J_o, J_1	Bessel function of first kind
I_o	modified Bessel function of the first kind
N_o	initial in-plane compressive load (N/m)

$N_{r,\theta}^{T}$	radial and circumferential thermal force (*N/m*)
$M_{r,\theta}^{T}$	radial and circumferential thermal moment (*N*)
ρ_A	areal-density of the composite diaphragm (kg/m^2)
A_{ij}	elements of the extensional-stiffness matrix (*N/m*)
B_{ij}	elements of the flexural-extensional coupling matrix (*N*)
D_{ij}	elements of the flexural-stiffness matrix (*N m*)
γ	coefficient of thermal expansion ($^oC^{-1}$)
δ	delta function
ρ_i	elements of the resistivity tensor (Ωm)
π_{ij}	elements of the piezoresistive tensor (Pa^{-1})
$\sigma_{r,\theta}$	radial and circumferential stress components (N/m^2)
$\varepsilon_{r,\theta}$	radial and circumferential strain components
$\kappa_{r,\theta}$	radial and circumferential curvatures (m^{-1})
$G\left(r,z,t\middle\vert r',z',\tau\right)$	Green's function
r',z'	location of the source (*m*)
r,z	location of the observer (*m*)
u_o	radial displacement of the reference plane (*m*)
w	transverse displacement of the plate (*m*)

Abstract of Dissertation Presented to the Graduate School
of the University of Florida in Partial Fulfillment of the
Requirements for the Degree of Doctor of Philosophy

THERMOELASTICALLY ACTUATED ACOUSTIC PROXIMITY SENSOR WITH INTEGRATED ELECTRICAL THROUGH-WAFER INTERCONNECTS

By

Venkataraman Chandrasekaran

May 2004

Chair: Mark Sheplak
Major Department: Mechanical and Aerospace Engineering

The development of micromachined acoustic proximity sensors for real-time cavity monitoring of underwater high-speed supercavitating vehicles is presented. Low-resistance polysilicon-based electrical through-wafer interconnects have been integrated with the sensor/actuator to enable backside contacts for drive and sense circuitry. The sensor and interconnects were fabricated in a complementary metal-oxide-semiconductor compatible process using deep reactive ion etching, producing a 1 *mm*-diameter, variable thickness (5-10 μm) composite diaphragm and 20 μm-diameter high-aspect ratio through-wafer vias on a silicon-on-insulator wafer. The diaphragm incorporates a central resistive heater for thermoelastic actuation and diffused piezoresistors for sensing acoustic pressure perturbations. The polysilicon through-wafer interconnects facilitate a rugged "bump-bonded" sensor package suitable for the harsh sea-water application.

A coupled thermomechanical model for thermoelastic actuation of circular composite diaphragms has been developed to optimize the sound-radiation characteristics

of the acoustic transducer. Specifically, a closed-form solution for the 2-D, axisymmetric temperature distribution in the composite diaphragm due to dynamic Joule heating of the diffused central heater was obtained using Green's functions and Hankel transforms. Next, a closed-form solution for the thermoelastically-forced vibration of the composite diaphragm was obtained using Kirchoff's plate theory.

Electrical, mechanical and acoustic characterization of the device indicates a transmitter source level of 50 *dB* (ref 20 μPa) at an operating frequency of 60 *kHz*, a receiving sensitivity of 0.98 $\mu V/(V\ Pa)$, a flat frequency response over the measured range of 1-20 *kHz*, a linear response from 60-140 *dB*, negligible leakage current for the junction-isolated diffused piezoresistors (< 14 *pA* at -10 *V*), low interconnect resistance of 14 Ω, and a minimum detectable signal of 36.5 *dB* for a 1 *Hz* bin centered at 60 *kHz*, at a bias of 9 *V*.

CHAPTER 1
INTRODUCTION

The goal of this research effort is to develop a microelectromechanical systems (MEMS)-based measurement system to monitor the state and thickness of the gaseous cavity surrounding an underwater high-speed, supercavitating vehicle (HSSV). The high velocity of the HSSV is enabled by supercavitation, a phenomenon in which a gaseous cavity envelops the majority of the vehicle, thereby considerably reducing the wetted friction drag (Lecoffre 1999). However, to ensure the stability of the gaseous cavity as the vehicle maneuvers through the water requires knowledge of the cavity thickness at all times. Thus a real-time measurement of the overall cavity thickness is required for vehicle guidance and control. The development of a cavity-sensing technology represents a significant challenge due to the complex nature of supercavitating flows (Senocak 2002) and the associated harsh sea-water environment. This study is part of a larger effort to combine multi-domain design methods, novel MEMS structures and advanced digital signal processing (DSP) techniques to develop a distributed acoustic based cavity-monitoring system to provide feedback information to an active cavity flow control system. This chapter presents an overview of supercavitation and the motivation for developing a cavity monitoring system using MEMS-based acoustic transducers.

Cavity Physics

As flow is accelerated over the body of a high-speed underwater vehicle the local pressure drop is inversely proportional to the square of the velocity (Batchelor 1967). At very high velocities, as the pressure continues to decrease, a point is reached where the

pressure in the flow becomes less than the vapor pressure of the fluid. This causes a phase change in the fluid resulting in the formation of gas or gas/vapor cavities (Batchelor 1967). The shape of the cavity is determined by several factors including the body creating it, the cavity pressure and gravitational force (Batchelor 1967). Cavitation causes severe damage to hydrodynamic structures such as pitting of turbine blades, but it also has beneficial applications such as drag reduction in hydrofoil boats and supercavitating vehicles. Supercavitation is an extreme version of the cavitation phenomenon characterized by the formation of a single bubble enveloping the moving object either partially or completely. Typically, at velocities of over 50 *m/s*, blunt-nosed cavitators and tip-mounted gas-injection systems produce these low-density gas pockets, encapsulating the vehicle and thus greatly reducing wetted friction drag (Ashley 2001).

Cavitating flows in most engineering systems are turbulent. The associated dynamics of the cavity interface is governed by the complex interactions between the liquid and gas phases. Senocak (2002) provides a computational model for qualitative and quantitative prediction of the features of turbulent cavitating flows along with a comprehensive review of the previous work in the field.

A simplified schematic of the gaseous cavity surrounding the HSSV is shown in Figure 1-1 and serves merely as a guideline for the sensor development. The interface can be roughly classified into three regimes, ranging from a smooth/well-defined structure, typically close to the cavitator (Figure 1-1: Region 1), to an unstable wavy profile resulting from the high-density gradients in the gas/water interface (Figure 1-1: Region 2) and ultimately degrading to a complex, multiple-bubble, two-phase flow (Figure 1-1: Region 3).

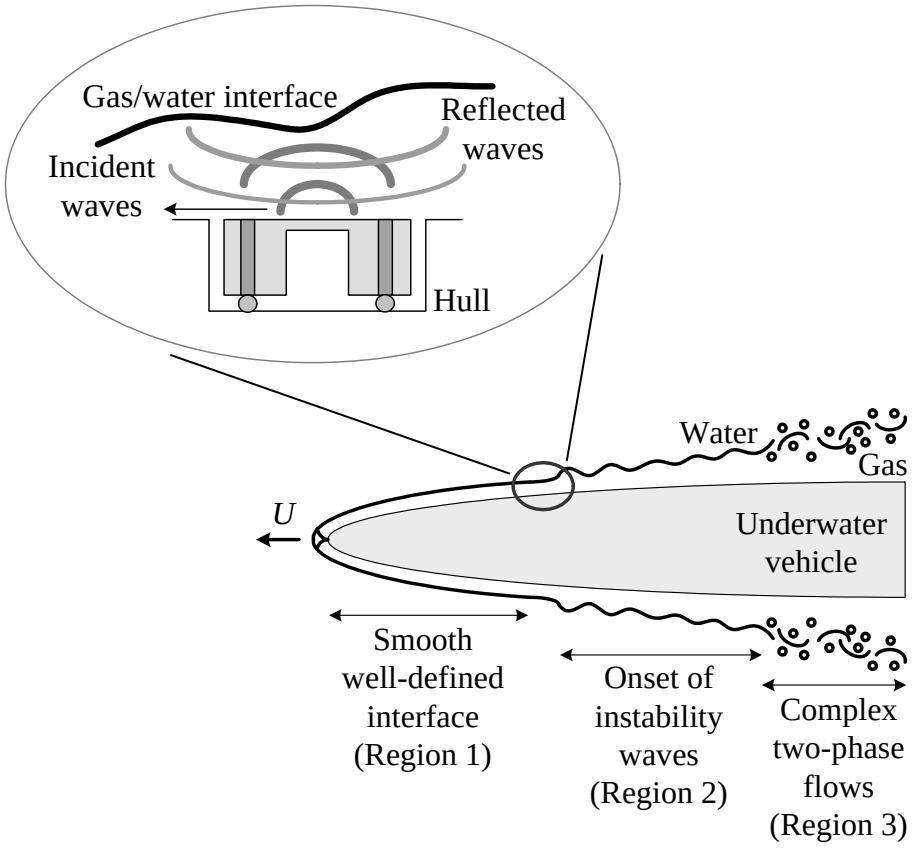

Figure 1-1: Schematic of a bump-bonded sensor package placed on the hull of an underwater supercavitating vehicle for monitoring the state and thickness of the gas/water interface.

Cavity Sensing Issues

There are several ways of measuring the interface distance, all of which involve the radiation of energy from the hull towards the gas/water interface, the subsequent reflection of the incident wave at the interface, and the detection of the reflected wave (Figure 1-1). The unstable nature and poor electromagnetic (EM) reflection coefficient (< 2 %) of the gas/water interface are some of the disadvantages of using laser or EM-based techniques (Antonelli et al. 1999). In contrast, acoustic techniques possess good signal-to-noise characteristics due to the sound hard nature of the interface with a unity reflection coefficient. In addition, as the cavity structure begins to degrade and the interface possesses waviness or bubble regions, the specular reflection assumption is

strongly dependent on the interface roughness relative to the wavelength (λ) of the radiated energy. If the interface roughness is larger than a quarter wavelength of the radiated energy ($l > \lambda/4$), the incident radiation will be scattered at the wavy interface and may not be redirected to the fixed receiver location (Tolstoy and Clay 1987). In these regions, acoustic-based techniques provide an advantage because it is possible to fabricate compact devices that radiate acoustic energy with wavelengths on the order of several millimeters (Brand et al. 1997). Furthermore, laser-based techniques may not be able to differentiate between a wavy interface and multiple-bubble regions. Acoustic techniques may be able to distinguish the two regions due to resonant scattering of acoustic waves from bubble surfaces (Williams 1999). Since the scattering cross-sections and resonant frequencies are a function of the bubble size, information regarding the presence and size of bubbles may be provided to the flow control system. Thus acoustic techniques present a potentially efficient way of measuring the interface proximity as well as discerning the nature of the interface. However, a disadvantage of the technique is that the acoustic velocity is a function of temperature and the medium of propagation (Blackstock 2000), both of which may vary within the gaseous cavity.

From a reliability perspective, the measurement system must be able to withstand the harsh environment associated with supercavitating flows. This necessitates a sensor possessing a hydrophobic barrier and backside electrical connections to drive and sense circuitry for increased robustness and protection against the corrosive sea-water environment. The sensor system would have to be a distributed network to provide feedback information about the entire cylindrical cavity structure and would have to provide fast parameter updates (> 50 *Hz*) due to the continuously changing interface

conditions. This ideally requires multiple sensors with matched characteristics for faster and more efficient signal processing. These requirements may be addressed by MEMS-based transducers that offer several potential advantages over conventional technology in terms of system performance and integration. In particular, the batch fabrication process employed for MEMS-based transducers yields devices with matched characteristics due to identical process conditions (Madou 1997).

Scope

The goal of this research effort is to design, fabricate, and characterize a prototype MEMS-based acoustic proximity sensor for monitoring the state and thickness of the cavity surrounding the HSSV. The system should be capable of measuring cavity thickness ranging from 1 to 10 *cm*, provide fast parameter updates (>50 *Hz*), and be capable of operating in a harsh sea-water environment. The contributions of this effort in the areas of transducer design, fabrication and packaging are listed below.

Research Contributions

- Development of a MEMS-based acoustic proximity sensor capable of generating and detecting acoustic waves with wavelengths on the order of several millimeters.
- Development of an electrical through-wafer interconnect (ETWI) technology, and its integration with the sensor/actuator to enable a rugged bump-bonded transducer-packaging scheme.
- Development of a novel analytical model for the thermoelastic actuation of composite diaphragms to optimize the sound radiation characteristics of the transducer.

Dissertation Organization

This dissertation is organized into 7 chapters. Chapter 1 provides the background, motivation and objectives of the research effort. Chapter 2 provides a review of the published work on micromachined acoustic resonators. Chapter 3 describes the first-generation acoustic proximity sensor developed for the cavity monitoring application

with details of the device fabrication process. Chapter 4 presents the theoretical development of the thermoelastic actuation and the piezoresistive detection schemes employed for the generation and detection of acoustic waves. Chapter 5 provides a description of the experiments used to characterize the sensor/actuator, and Chapter 6 presents the results of the characterization. Chapter 7 offers concluding remarks and scope for future work in areas of sensor modeling and fabrication for performance enhancement of the second-generation proximity sensor.

CHAPTER 2
LITERATURE REVIEW

This chapter provides a review of the published work on micromachined ultrasonic resonators based on both conservative and non-conservative transduction schemes and their potential advantages over conventional transducers.

Conventional Ultrasonic Transducers

Acoustic proximity sensors are used for a wide range of non-contact distance measurement applications (Massa 1999). Conventional transducers use the pulse-echo technique to measure the distance to a target. In this method, the transducer is excited by a burst of pulses, which are transmitted towards the target and are subsequently reflected. The time of arrival of the reflected pulse is then estimated via schemes like threshold detection or sliding window techniques (Barshan 2000). The time-delay together with the knowledge of the acoustic velocity in the medium provides an estimate of the distance. Several transduction schemes have been used for the generation of acoustic waves at ultrasonic frequencies, but for industrial applications, circular piezoceramic transducers (e.g., lead zirconium titanate - PZT) vibrating in the thickness mode are most commonly used (Manthey et al. 1992). These resonant acoustic transducers exhibit the behavior of an underdamped second-order system, in which the response to a sharp pulse input is characterized by a *ring*, or in other words, there is finite decay time for the transmitter vibrations. Thus, for a single transmitter/receiver this creates a “dead-zone” in the vicinity of the transmitting surface where objects cannot be detected, creating a lower bound on the measurable distance (Manthey et al. 1992). Usually, an additional

quarter-wave matching layer made of a low-density polymer is deposited over the transmitting surface for better impedance matching with a gas medium and improved radiation efficiency (Mockl et al. 1990). The matching layer results in higher sound pressure level due to larger vibration amplitude and the higher damping of the low-density polymer reduces the transmitter decay time improving the distance resolution of the transducer over a limited frequency range.

MEMS-based proximity sensors have been fabricated by combining standard semiconductor processing techniques with bulk and surface micromachining (Madou 1997) to produce thin, compliant diaphragms on a silicon substrate. MEMS-based transducers offer several potential advantages over their conventional counterparts, including lower impedance and a wider bandwidth of operation. Micromachined transducers utilizing a thin, compliant diaphragm as the acoustic source provide a better impedance match with air compared to solid piezoceramic elements. Their small size translates to better spatial and temporal resolution and makes them effective for measuring very small distances. The batch fabrication process yields sensors with matched characteristics, which would be invaluable for a distributed network of sensors, and significantly lower cost per device (Arnold et al. 2002). The technology also lends itself to a compact “flip-chip” type sensor packaging scheme with backside contacts for drive and sense electronics making it rugged and more suitable for the harsh sea-water environment (Al Sarawi et al. 1998, Heschel et al. 1998).

Several different actuation and sensing mechanisms have been reported in the literature for the generation as well as detection of acoustic waves utilizing micromachined diaphragms as the acoustic source and sensor. Reciprocal actuation

mechanisms (piezoelectric, capacitive) are based on conservative power exchange and energy storage and can also be used for sensing. Irreversible schemes such as electro- and opto-thermal actuation are based on energy dissipation and are usually used in conjunction with irreversible detection schemes, such as piezoresistive detection and others based on optical methods or tunneling currents (Hornung and Brand 1999). The type of sensor and operating principle used will depend to a large extent on the end application, and is based on factors such as measurement environment, frequency range of interest, achievable actuation force, detection sensitivity and signal-to-noise ratio. System issues such as power consumption and integration with support electronics also play an important role, in addition to manufacturing cost and complexity. A comprehensive review of silicon resonant sensors has been presented by Stemme (1991) and Brand and Baltes (1997).

Micromachined Ultrasonic Transducers

The following section presents an outline of the various silicon micromachined acoustic transducers reported in the literature.

Brand et al. (1993, 1994) and Hornung et al. (1997, 1998) have developed transducers operating around 70-90 *kHz*. This is a released diaphragm-type transducer created using potassium hydroxide (KOH) etching of the bulk silicon substrate with an electrochemical etch stop to define the diaphragm thickness (Figure 2-1).

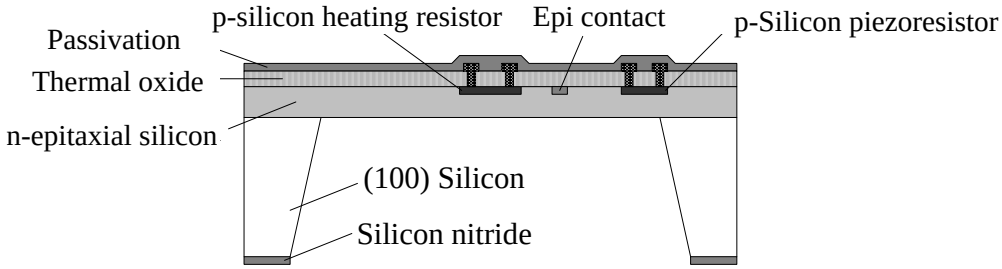

Figure 2-1: Cross-sectional schematic of a 1 *mm* x 1 *mm* thermally actuated membrane resonator (adapted from Brand et al. 1997).

The diaphragm is set into vibration via electro-thermal heating of an integrated heater on the diaphragm. The heating establishes a temperature gradient across the layered composite diaphragm causing it to deflect. The diaphragm vibration is detected using piezoresistors placed at the edges. The sensors were operated at their fundamental resonant frequency maintained by a positive feedback circuit. For an average heating power of 100 *mW*, maximum vibration amplitudes of 300-400 *nm* and sound pressure levels of 81.9 *dB* (at a distance of 50 *mm*) were obtained. The piezoresistors are arranged in a Wheatstone bridge configuration with a detection sensitivity of 0.4 $\mu V/V\ mPa$ at resonance.

Jin et al. (1998, 1999) reported the fabrication and characterization of surface micromachined capacitive ultrasonic transducers (cMUT) for use in the megahertz range. The operating principle is based on electrostatic excitation and capacitive detection and the devices were fabricated on a single wafer using sacrificial layer techniques. A typical transducer measures 1.75 *mm x* 1.75 *mm* and is formed from an array of 50 *x* 50 capacitive cells. Each cell consists of a 30 μm-diameter and 0.53 μm-thick diaphragm, forming a parallel plate capacitor with a sealed cavity (Figure 2-2).

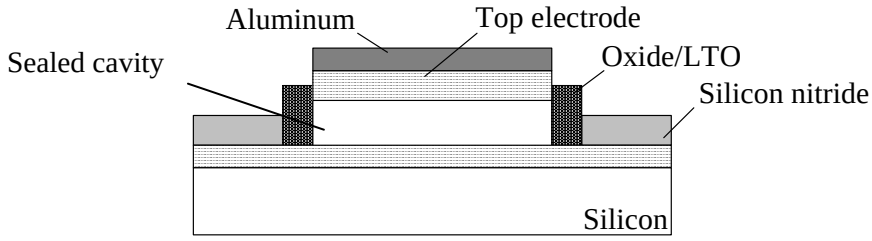

Figure 2-2: Cross-section of a capacitive micromachined ultrasonic transducer element (adapted from Jin et al. 1998).

Maximum diaphragm displacement of 230 *Å/V* was reported. Different types of membranes (silicon nitride and polysilicon) as well as vacuum sealing techniques were

investigated. Vacuum sealing of the cavity reduces the effects of cavity stiffening (Rossi 1988) associated with operation in air. The disadvantage of electrostatic actuators is that they require very narrow gaps between the electrodes in order to produce large excitation forces, adding to the fabrication complexity of the device. In addition, during underwater operation, the pressure of the water can cause a static deflection of the diaphragm which would be difficult to compensate with a sealed cavity and a narrow gap between electrodes.

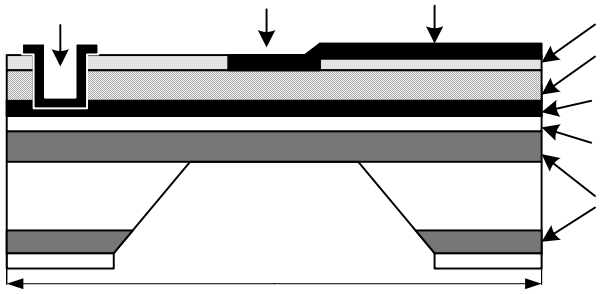

Figure 2-3: Cross-section of a ferroelectric transducer (adapted from Bernstein et al. 1997).

Bernstein et al. (1996, 1997, 1999, 2000) have designed diaphragm-based ferroelectric ultrasound transducers for high-frequency imaging applications (up to 2 *MHz*). Ferroelectric monomorph sonar transducers with diaphragm sizes ranging from 0.2 *mm* to 2 *mm* were built using sol-gel PZT on micromachined silicon wafers. When the PZT extends due to an applied voltage, the diaphragm is forced into vibration. And similarly, any deflection of the diaphragm caused by acoustic waves creates a voltage in the PZT. A cross-sectional schematic of the completed transducer is shown in Figure 2-3. A modified sol-gel process yielded crack-free PZT films up to 12 μm in thickness, improving the sensitivity of certain classes of sensors and producing larger output forces

for actuators. The measured sensitivity for a 260 μm *x* 260 μm device without correcting for the effects of stray capacitance was reported to be 1.4 $\mu V/Pa$.

Sleva et al. (1994, 1996) have developed sensors fabricated by spin casting P(VDF-TrFE) onto a silicon membrane which is backfilled with epoxy (Figure 2-4). Transducers measuring 2 *mm* in diameter and operating at 31 *MHz* were fabricated. The epoxy provides for a soft boundary condition on the backside of the piezo element and yields a wide-band, half-wavelength resonant device suitable for pulse-echo applications.

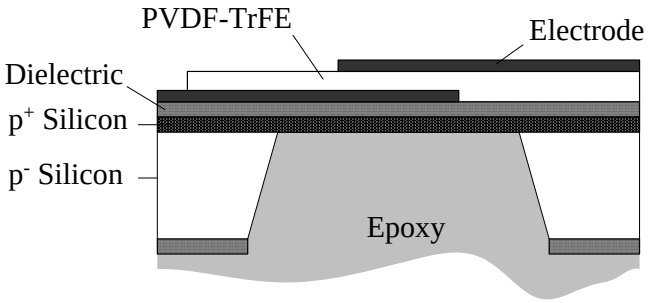

Figure 2-4: Cross-sectional schematic of the P(VDF-TrFE)/silicon-based transducer (adapted from Sleva et al. 1996).

However, the use of P(VDF-TrFE) material resulted in a transducer with very low sensitivity. A dynamic range of 40 *dB* and an insertion loss of 48 *dB* were reported.

Lynnworth et al. (1997) describe the use of solid piezoceramic elements for air-coupled transducers in the 50 *kHz* to 500 *kHz* range. Solid piezoceramics are good because they are robust and can handle temperatures from -40 °*C* to +125 °*C*. A quarter-wave impedance matching layer is needed to make these transducers suitable for applications in air. One drawback, however, is that similar to conventional ultrasonic proximity sensors, these transducers are highly underdamped, which limits the use of the pulse-echo proximity sensing scheme for measuring small distances.

For the cavity monitoring application, piezoelectric and electrostatic transducers were not chosen because of their high impedance that makes integration with ETWI more

difficult due to the effects of parasitic capacitance (Scheeper et al. 1994). Thermoelastic actuation and piezoresistive sensing provide the best compromise among performance, low cost, durability, ease of fabrication and simpler interface electronics (Hornung and Brand 1999). Since the device relies on a resistive element for both sensing and actuation, it inherently possesses lower impedance compared to capacitive or piezoelectric schemes. Thermoelastic actuators also scale favorably with micro-miniaturization. The amount of thermal mass (inertia) decreases with the volume of the structure, which directly translates to a faster response time. Vibration of micromachined structures (beams, diaphragms) using electro-thermal excitation have been demonstrated up to frequencies in the megahertz range (Lammerink et al. 1992, Brand et al. 1997). Secondly, the percentage of thermal energy lost via conduction into the bulk substrate reduces with decreasing thickness of the structures, while maintaining a high force per unit area. Thus, the low impedance of the devices coupled with favorable scaling of the achievable actuation forces and dissipation losses with miniaturization makes them a suitable choice for the cavity monitoring application.

CHAPTER 3
ACOUSTIC PROXIMITY SENSOR

This chapter presents a detailed description of the first-generation acoustic proximity sensor. Details of the integrated acoustic transducer/ETWI structure, transduction schemes used for the generation and detection of acoustic waves and device fabrication process are described.

The transducer consists of a thin single crystal silicon membrane as the acoustic source/sensor for improved impedance matching with the gas medium. The transceiver structure integrates diffused resistors for thermoelastic actuation and piezoresistive detection and boron-doped polysilicon electrical through-wafer interconnects (ETWI) for backside contacts. Figure 3-1 shows a top view optical image of the sensor/actuator, and a cross-sectional schematic is shown in Figure 3-2. The device structure consists of a 1 *mm*-diameter, variable thickness (5-10 μm) circular diaphragm, created using a deep reactive ion etch (DRIE) backend process. This process combined with a silicon-on-insulator (SOI) wafer as the substrate allows for strict geometry control in terms of thickness and diameter of the diaphragm. Two semicircular diffused heaters (60 μm-diameter and 0.46 μm-junction depth) are located in the center for thermoelastic actuation of the diaphragm. Four diffused p-type piezoresistors are located at the edge of the diaphragm for piezoresistive detection of the transverse vibrations.

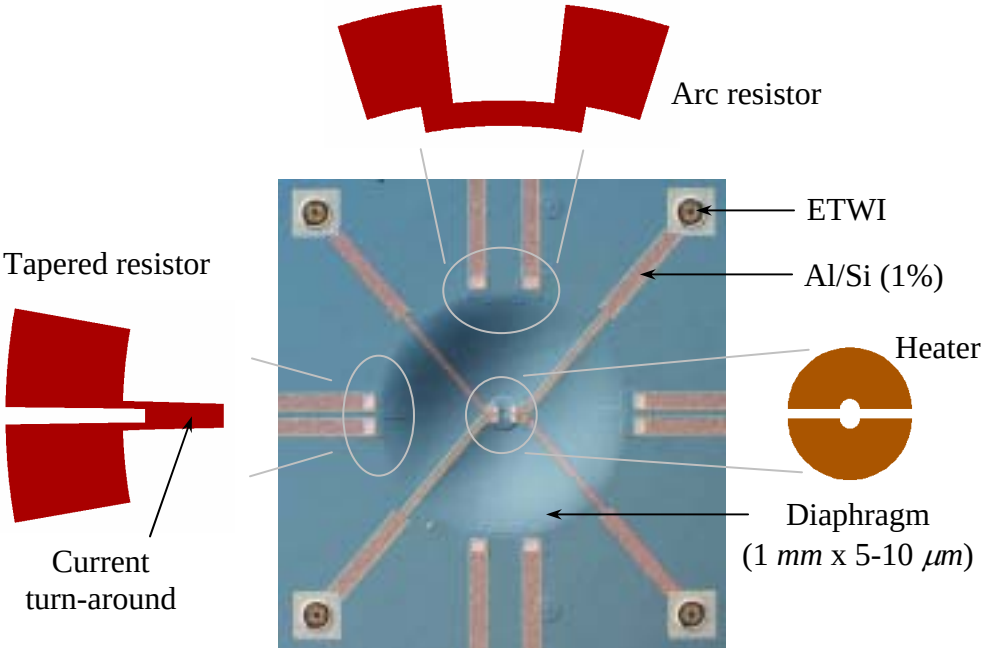

Figure 3-1: Top view microscopic (diffraction interference contrast) image of the acoustic proximity sensor with integrated through-wafer interconnects.

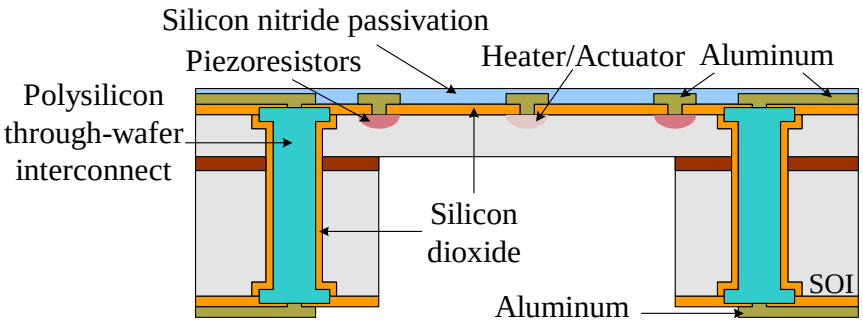

Figure 3-2: Cross-sectional schematic of the acoustic proximity sensor.

The use of single-crystal silicon provides maximum sensitivity and a lower noise floor compared to polycrystalline devices (Brysek et al. 1988). In the case of the tapered piezoresistors, two resistors are connected in series via a current "turn-around" as shown in Figure 3-1 (Sheplak et al. 1998). The dimensions of the turnaround are designed such that its contribution to the total resistance is negligible (< 3 %). This arrangement eliminates additional metal lines on the diaphragm.

The intended application of the sensor necessitates a rugged package capable of withstanding the harsh seawater environment. Therefore, polysilicon-based ETWI measuring 20 μm in diameter have been integrated with the sensor/actuator (Chandrasekaran et al. 2001, Chow et al. 2002) as shown in Figure 3-2. The use of p-type (boron-doped) ETWI enables direct ohmic contact to p-type piezoresistors employed for the acoustic transducer (Pierret 1996). The ETWI thus enables an integrated "bump-bonded" sensor packaging scheme with the drive and sense circuitry hidden from the harsh cavity environment (Figure 3-3).

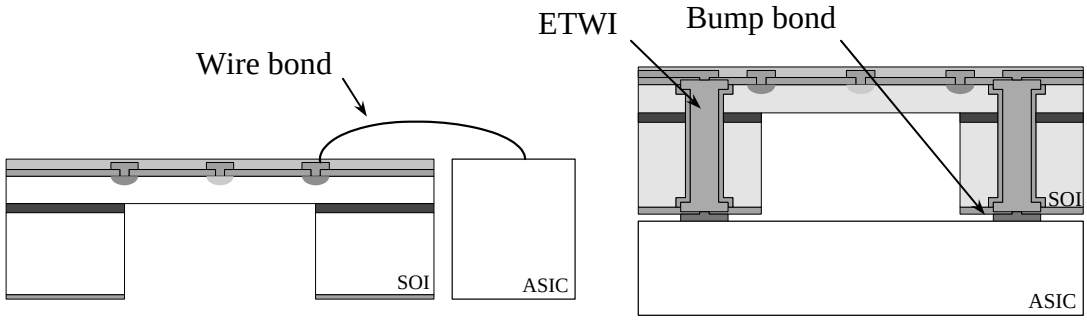

Figure 3-3: Traditional wire-bonded sensor package versus the more compact and rugged bump-bonded package.

The thermoelastic heater and piezoresistors are connected to the ETWI via 75 μm-wide, 1.4 μm-thick aluminum (1% Si) traces. A 7000 $\AA$-thick silicon dioxide film is thermally grown on top of the silicon layer to provide compressive stress to the diaphragm in addition to serving as a dielectric passivation for the piezoresistors. The in-plane compressive loading provided by the thermal oxide layer together with the aspect ratio of the diaphragm may be used to optimize the device sensitivity. A 3500 $\AA$ low-stress, plasma enhanced chemical vapor deposited (PECVD) silicon nitride passivation layer provides a protective moisture barrier on the top surface of the device. In the

following sections, the transduction schemes used for the generation and detection of acoustic waves as well as the device fabrication process are discussed.

Operating Principles

Thermoelastic Actuation

Dynamic Joule heating of the diffused central resistors creates a time-varying two-dimensional temperature distribution across the diaphragm. The non-uniform temperature profile through the thickness of the diaphragm generates integrated thermal forces and moments resulting in the transverse vibration of the diaphragm. The flexural-extensional coupling is further enhanced by the asymmetrical composite structure of the diaphragm. Thus, by applying a time-varying instantaneous voltage signal, the diaphragm is forced into vibration. The temperature distribution in the diaphragm is a function of the driving frequency of the signal and depends on the depth of penetration of the thermal waves, governed by Fourier's law of heat conduction (Ozisik 1993). The harmonic Joule heating excites the diaphragm at the driving frequency, ω and additionally at twice that frequency, 2ω, and at dc. This is due to the non-linear nature of thermoelastic actuation, where the input power has a quadratic dependence on the excitation voltage, causing the power to be redistributed into two other frequency bins (i.e., 0 and 2ω). By adding a conditioning dc voltage the ratio of power between the three frequency bins can be controlled as shown by the following equation:

$$\left(\bar{V} + V' \sin \omega t\right)^2 = \bar{V}^2 + \frac{V'^2}{2}\left(1 - \cos 2\omega t\right) + 2\bar{V}V' \sin \omega t. \qquad (3.1)$$

However, adding an offset voltage to the harmonic signal adds a static temperature distribution, which consequently changes the in-plane stress field and the resonant frequency of the diaphragm.

The heater is designed with a shallow junction depth of 0.46 μm (5-10 % of the diaphragm thickness) in order to create a temperature gradient across the diaphragm cross-section at the given operating frequencies (< 100 *kHz*). Additionally, the circular shape and central placement of the heating resistor pair ensure that the fundamental mode of diaphragm is excited and maximum vibration amplitude is achieved (Lammerink et al. 1990). The theoretical development of the thermoelastic actuation scheme using an analytical thermomechanical model will be discussed in Chapter 4.

Piezoresistive Detection

Piezoresistivity is defined as the change in the resistivity of a material due to a change in the mobility (or number of charge carriers) induced by a mechanical strain to the material (Smith 1954). For an anisotropic solid, the resistance modulation is a function of the applied stress and the piezoresistive coefficients of the material.

Electromechanical transduction of the diaphragm vibration is thus achieved via four diffused silicon piezoresistors located at the edge of the diaphragm in a fully active Wheatstone bridge configuration. This configuration provides a linear relation between the bridge voltage output and the input pressure perturbation provided that the mean resistances in all four legs are equal and that the resistance modulation in each resistor of a given leg is equal in magnitude, but of opposite signs. For the first-generation transducer the arrangement consists of two tapered and two arc-shaped piezoresistors as shown in Figure 3-4. The choice of arc and tapered resistors is dictated by the circular geometry of the diaphragm (Sheplak et al. 1998). The piezoresistors are designed such that they possess the same nominal resistance $(R_{arc} = R_{taper})$ and equal but opposite resistance modulation $(\Delta R_{arc} = -\Delta R_{taper})$. Thus for an undeflected diaphragm, the output

of the Wheatstone bridge is ideally zero, but a deflection caused by an acoustic wave produces a differential voltage output across the bridge.

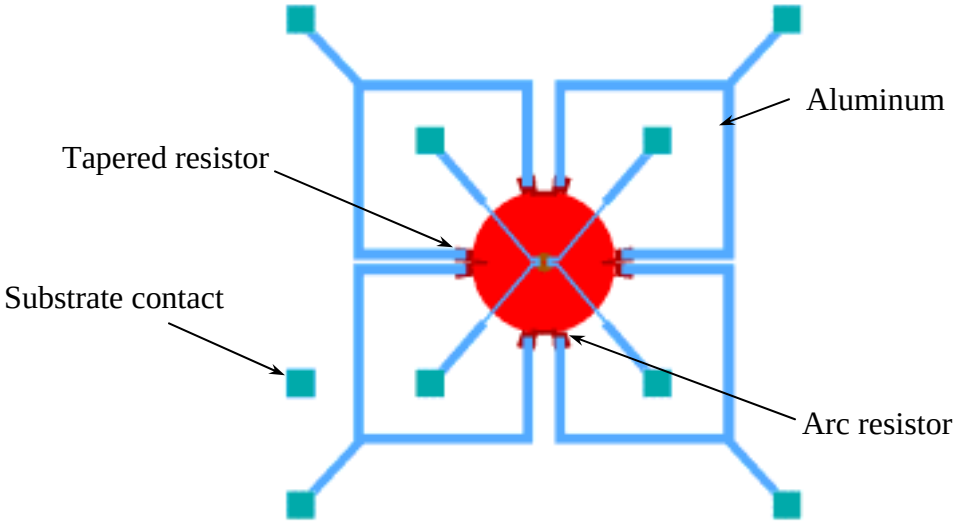

Figure 3-4: Schematic of the arc and tapered piezoresistors arranged in a Wheatstone bridge configuration.

The theoretical development of the piezoresistive detection scheme for sensing acoustic pressure perturbations is presented in Chapter 4. The remainder of this chapter describes the processing techniques used for the fabrication of the integrated acoustic transducer/ETWI.

Device Fabrication

The fabrication process begins with the creation of the electrical through-wafer interconnects. After the wafer with ETWI is planarized, the ETWI wafer provides the substrate for the subsequent backend complementary metal-oxide-semiconductor (CMOS) process to fabricate the acoustic proximity sensor. The interconnects were fabricated using a variation of the polysilicon-based ETWI technology demonstrated by Chow et al. (2002) for easier integration with the p-type piezoresistors used for the acoustic transducer. A detailed process traveler is provided in Appendix A.

Electrical Through-Wafer Interconnect

In the previous chapter, the need for electrical through-wafer interconnects to enable a rugged "flip-chip" type bump-bonded transducer package was described. Several different technologies have been employed for creating the ETWI. However, most of these techniques are incompatible with standard CMOS processing. Anisotropic wet chemical etching is a commonly used technique for fabricating through-wafer vias, but this technique results in large chip sizes and impedes the subsequent processing with many etching, metallization and lithography equipment (Goldberg et al. 1994, Linder et al. 1994, Christensen et al. 1996). Copper electroplating methods have also been combined with DRIE to form ETWI for RF applications (Chow et al. 1998, Soh et al. 1999, Wu et al. 2000). DRIE has also been combined with chemical vapor deposited (CVD) tungsten for cantilever array applications (Chow et al. 2000). Metal-filled DRIE-etched vias permit a smaller chip size, relative to the wet-etched contacts, but the metals used in the interconnects are not always compatible with high temperature processing, thus limiting the commercial use of these techniques.

The technology to create high density, polysilicon-based electrical through-wafer interconnects using DRIE was demonstrated by Chow et al. (2002). Using this technique, 20 μm-diameter vias with an aspect ratio of ~25:1 were achieved. Phosphorus-doped polysilicon forms the conducting layer, which is isolated from the substrate with a *2* μm-thick thermal oxide layer. This technique is CMOS compatible and possesses the following advantages: ETWI fabrication prior to device fabrication, the capability to withstand subsequent high temperature thin-film deposition, and low resistance/capacitance suitable for most MEMS applications.

The ETWI fabrication process begins with a 450 μm-thick double side polished n-type SOI wafer as illustrated in Figure 3-5 (A). A 2 μm thermally grown silicon dioxide layer acts as the mask for the through-wafer via etch (B). In order to maintain a high aspect ratio (25:1) structure, the vias were created by etching through both sides of the wafer. A front-to-back aligner was used to create the aligned two-sided pattern on the wafer and additionally an infra-red camera was used to inspect the alignment. A slight misalignment would result in a reduction of the via diameter, causing it to prematurely plug during the deposition of the polysilicon thin films. DRIE was then performed from the front and the back-side of the wafer for roughly equal durations to etch the via through the wafer (Figure 3-5 (B)).

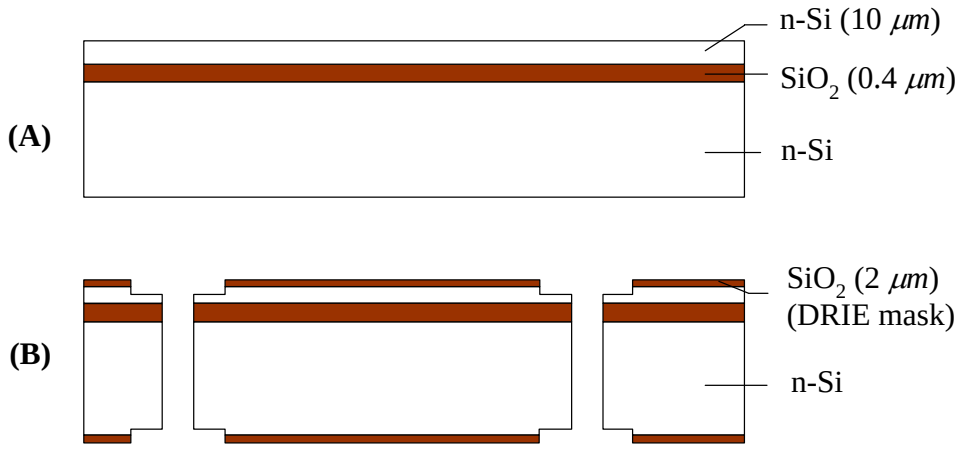

Figure 3-5: A schematic of the fabrication process illustrating the creation of the through-wafer vias.

The etcher uses the Bosch process alternating between etching and passivation to create a high-aspect ratio structure. Once the vias were etched completely through the wafer, helium used for cooling flowed through the vias slowing the etch. By monitoring the helium flow, the etch progress was estimated. A small degree of lateral etching resulted in a tapered via profile illustrated in Figure 3-6. A timed (30 minutes) overetch was

performed from the frontside of the wafer using an etch recipe with higher passivation to smooth and straighten the via profile. A support wafer was used during the overetch step to prevent helium flow from the wafer chuck into the vias. After the etching was complete, the oxide mask was stripped using buffered oxide etch (6:1 BOE).

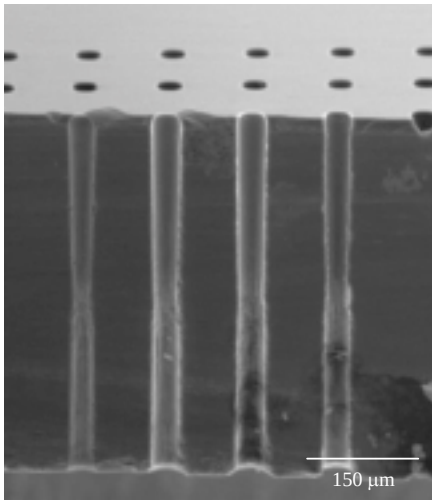

Figure 3-6: SEM cross-section after plasma etching vias through the wafer (Chow et al. 2002).

The etching of the via was followed by conformal thin film growth/deposition. To electrically isolate the interconnects from the bulk silicon substrate, a 2 μm thermal oxide layer was grown using a dry-wet-dry oxidation process (Figure 3-7 (C)). This process was used to ensure a high quality silicon-to-silicon dioxide interface.

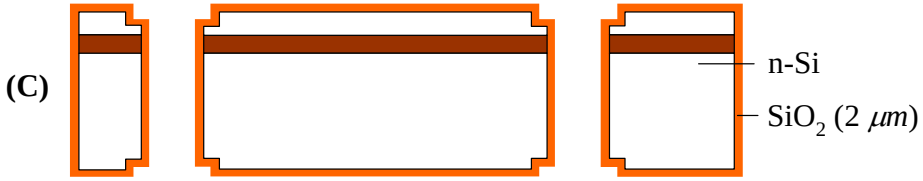

Figure 3-7: Fabrication sequence: Thermal oxide growth for electrical isolation of the interconnects from the silicon substrate.

For electrical conduction, 2 μm-thick polysilicon was deposited over the oxide using low-pressure chemical vapor deposition (LPCVD). This was followed by boron diffusion

doping of the polysilicon for 2 hours at 1000 ^{o}C and then an anneal at 1000 ^{o}C to fully drive the dopants through the polysilicon (Figure 3-8 (D)).

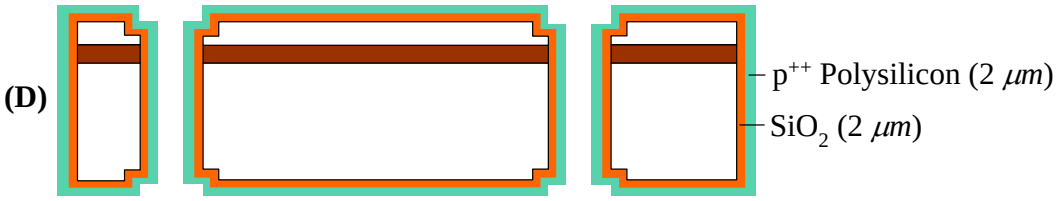

Figure 3-8: Fabrication sequence: Deposition and boron diffusion doping of polysilicon layers for electrical conduction.

The boron-doped polysilicon conduction layers enable direct ohmic interconnection to p-type piezoresistors employed for the acoustic transducer. However, the boron diffusion doping of polysilicon forms a non-conducting borosilicate glass, which is not easily removed using hydrofluoric acid. This is a critical difference between boron (p-type) and phosphorus (n-type) diffusion doping of polysilicon. The glass resulting from phosphorus doping of polysilicon is easily etched using hydrofluoric acid. However, in the case of polysilicon doping using boron, the glass must first be oxidized using wet oxidation at 1100 ^{o}C for 30 minutes, followed by 60 minutes in (6:1) BOE to etch the oxidized glass. The process of polysilicon deposition and boron diffusion doping was repeated two or three times to achieve a low resistance ETWI. The rest of the via was filled with polysilicon followed by boron diffusion doping and patterning of the top and bottom surfaces of the wafer (Figure 3-9 (E), Figure 3-10).

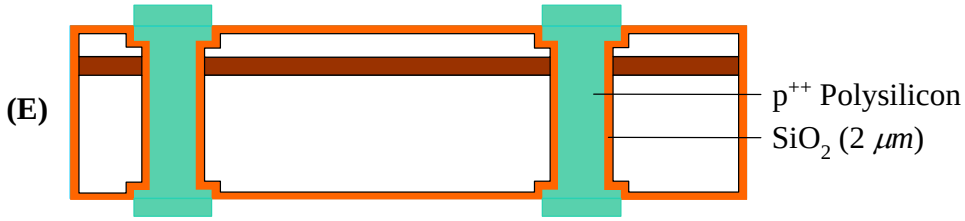

Figure 3-9: Fabrication sequence: Patterning the interconnects.

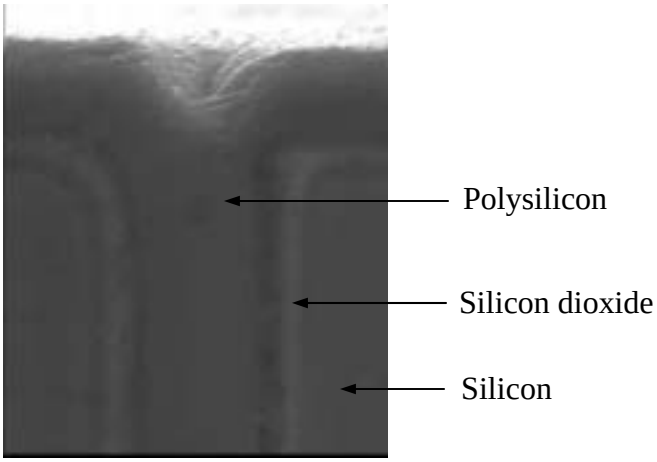

Figure 3-10: SEM illustrating the oxide insulation and the polysilicon conduction layers of the ETWI.

After patterning the ETWI, an isotropic plasma etch was performed on the doped polysilicon to planarize the interconnects and to produce a gradually sloping sidewall. This is critical for the integration of the ETWI with the sensor/actuator since it ensures proper metal coverage over the ETWI (Figure 3-11).

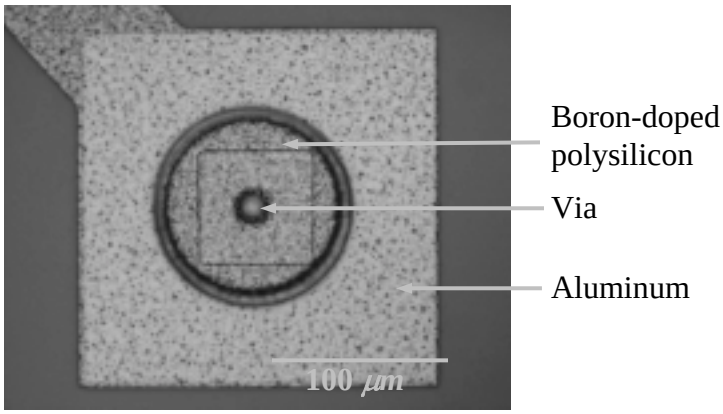

Figure 3-11: Through-wafer interconnect integrated with a metal bond pad.

Acoustic Sensor/Actuator

The SOI wafer with the patterned ETWI served as the substrate for the acoustic transducer fabrication process. A thin layer of oxide was grown and patterned to serve as a hard mask for the resistor implantations. Boron was implanted (energy: 170 *keV*, dose: 1E13 cm^{-2}) to achieve p^{++} regions with a concentration of 1E20 cm^{-3}. After implantation, the wafers were annealed at 1100 ^{o}C for 30 minutes to create a junction depth of 0.46 μm.

The wafers were then patterned with the piezoresistor mask and again implanted with boron (energy: 85 *keV*, dose: 8E13 cm^{-2}) to form p^{++} regions of similar concentration (Figure 3-12 (F)). After stripping the oxide mask, a 7000 *Å*-thick silicon dioxide layer was thermally grown at 950 ^{o}C to passivate the resistors and also to provide compressive stresses to the diaphragm in order to achieve the required sensitivity (Figure 3-12 (F)). The diffusion of the resistive heater and piezoresistors was simulated using FLOOPS® (Law and Cea 1998) (Appendix B) to account for the entire thermal budget of the process flow.

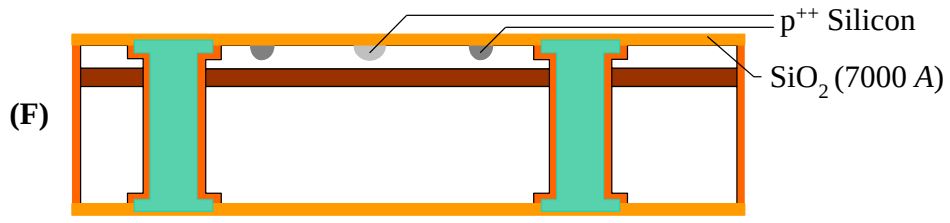

Figure 3-12: Fabrication sequence: Resistor implantation and thermal oxide growth.

A 1.4 μm-thick layer of aluminum with 1% silicon (to avoid spiking (Pierret 1996)) was sputtered and patterned, once the contact cuts in the oxide dielectric layer were made (Figure 3-13 (G)).

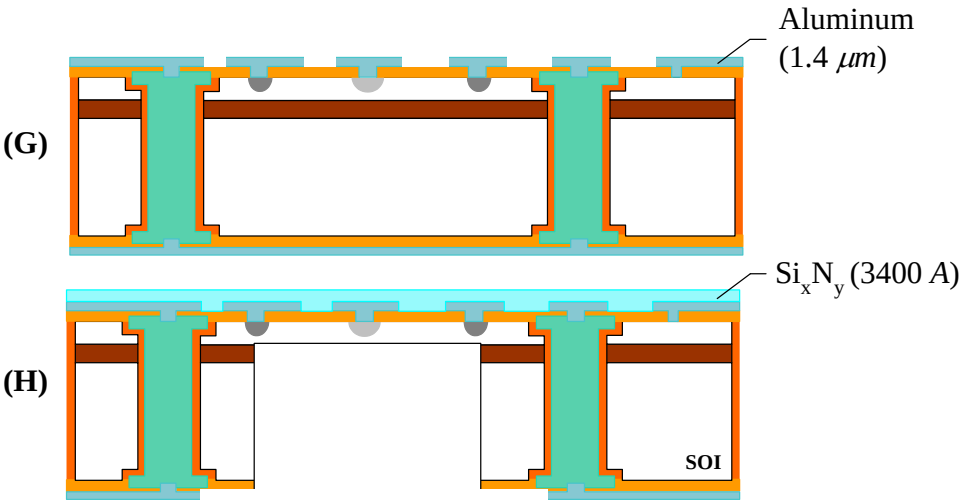

Figure 3-13: Fabrication sequence: Sputtering and patterning aluminum (1%-Si), silicon nitride deposition and DRIE to release the diaphragm.

Low-stress nitride (3500 *Å*) was then deposited using plasma-enhanced chemical vapor deposition to form a protective moisture barrier (Figure 3-13 (H)). The wafers were then patterned on the backside with front-to-back alignment to create the diaphragm. The relative alignment of the piezoresistors and the diaphragm is critical to ensure piezoresistor placement at the edge of the diaphragm. DRIE was performed from the backside of the wafer up to the buried oxide layer (Figure 3-13 (H)) and the buried oxide layer was removed using 6:1 BOE. A schematic of the integrated acoustic sensor/ETWI is illustrated in Figure 3-14.

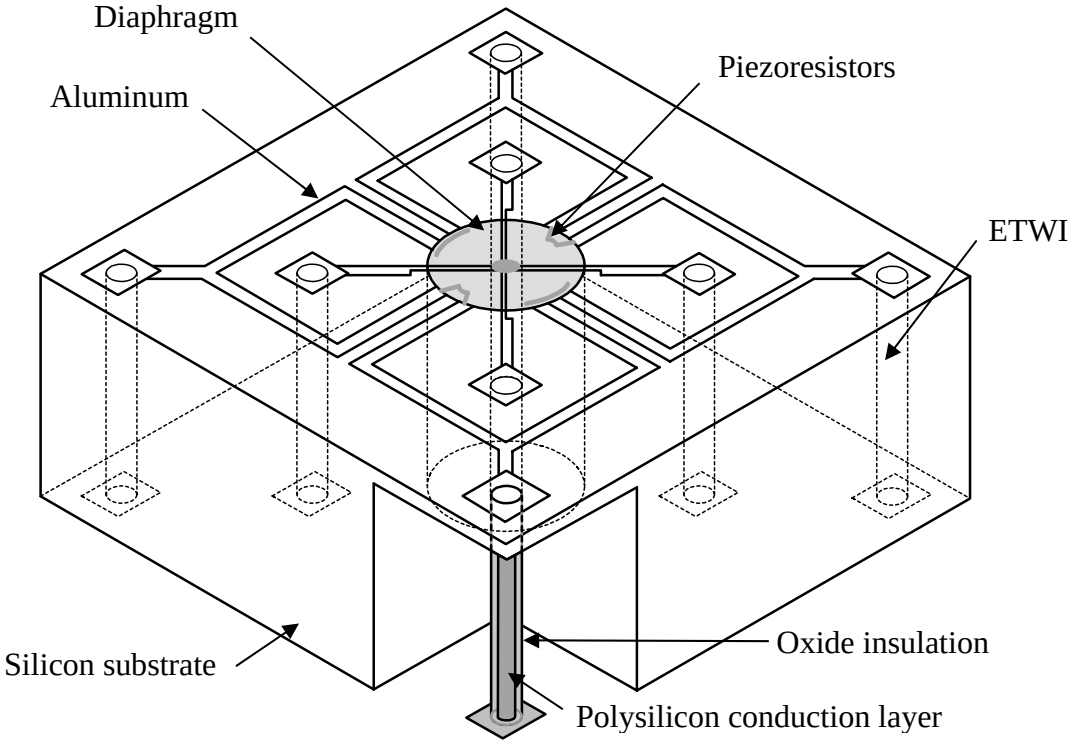

Figure 3-14: 3-D schematic of the integrated acoustic sensor/ETWI.

CHAPTER 4
DEVICE MODELING

The design of an acoustic proximity sensor in terms of sound radiation characteristics as well as sensitivity to acoustic pressure perturbation requires a thorough understanding of the overall system behavior. In particular, the influence of design parameters such as geometry, material properties and fabrication-induced stresses on the forced vibration characteristics of the resonating diaphragm needs to be investigated. This chapter presents the theoretical development of the transduction schemes employed for the proximity sensor and the various design considerations for optimizing the device performance. The first section describes an analytical model for the thermoelastic actuation of circular composite diaphragms that was developed to enable the optimization of the sound-radiation characteristics of the acoustic transducer. The second section focuses on the optimization of the piezoresistive-sensing scheme for maximum sensitivity to acoustic pressure perturbation and a low noise floor.

Thermoelastic Actuation

The operating principle of the thermoelastic actuation scheme and its suitability to micromachined transducers were presented in Chapter 2. Due to a significant number of design parameters including diaphragm radius, thickness of the individual layers, heater geometry, input power, operating frequency and in-plane stress, design and optimization based solely on finite element analysis is not practical due to computational time constraints. This necessitates the development of analytical models, since an analytical

expression of the diaphragm deflection provides scaling relations with the different design parameters, enabling quick identification of vibration characteristics over a range of input values. In addition, non-dimensional groups of the input parameters can be formed to reduce the number of dependencies, and the analytical model can be better integrated with formal optimization tools (Papila et al. 2003).

Issues for MEMS Transducers

In order to develop accurate analytical models applicable to MEMS-based thermal actuators, certain key aspects of the micromachined transducers namely multiple material layers, in-plane heat conduction and fabrication induced stresses have to be considered in the analysis. The composite nature of the vibrating structure is quite important since released cantilevers or diaphragms rarely consist of a single material. For example, in the case of thermoelastic actuators (Brand et al. 1997, Chandrasekaran et al. 2002), in addition to the silicon structural layer, thin films of silicon dioxide and silicon nitride are used for dielectric passivation and to provide a hydrophobic moisture barrier. Piezoelectric actuators (Bernstein et al. 1997) are comprised of PZT and electrode layers deposited over the silicon diaphragm. The electrical, mechanical and thermal properties of the various layers can be significantly different, altering the overall dynamic behavior of the transducer. Another important consideration, specifically for micromachined thermal actuators, is that the diffused resistor typically covers a small area of the diaphragm and the diffusion of heat from the resistor is both in the in-plane and thickness direction. As will be shown later in the chapter, neglecting the effects of in-plane heat conduction will severely over-predict the vibration amplitude of the diaphragm. Finally, the transducer fabrication process imparts significant in-plane stresses (compressive or tensile) that alter the vibration characteristics of the diaphragm.

Thermally-induced vibration of beams and plates by a time-harmonic heat flux on one surface have been analyzed by several authors including Irie and Yamada (1978), Lammerink et al. (1992) and Paul and Baltes (1999). However, there are several limitations to the models proposed by these authors. The analyses by Irie and Yamada (1978) and Lammerink et al. (1992) are restricted to homogenous structures. Paul and Baltes (1999) included varying material properties in their plate analysis, however, their thermal analysis was simplified to a homogenous beam with a surface heat flux. Furthermore, the in-plane heat conduction effects of the actuating heater have not been considered in any of the analyses.

In this section, a thermomechanical model that incorporates the composite nature of the diaphragm in both the thermal and mechanical analysis is presented. The diffused heater used for actuation is more accurately represented as an internal heat source rather than a surface flux and the analysis also includes the effects of in-plane heat conduction from the edge of the central heater.

2-D Thermomechanical Model

The analytical model consists of an axisymmetric composite diaphragm comprised of three transversely isotropic layers with different thermal and elastic properties as shown in Figure 4-1. The assumption of transversely isotropic elastic properties for silicon is a simplification based on its moderate degree of anisotropy $(\varphi = 1.57)$. For a cubic crystal, such as silicon, the degree of anisotropy is defined as

$$\varphi = \frac{2E_{44}}{E_{11} - E_{12}}, \tag{4.1}$$

where E_{ij} are the independent elastic moduli. For an isotropic material φ has a value of 1 (Brantley 1973). In addition, the angular variation of the elastic constants (< 30%) in

the (100) plane has also been neglected in the plate analysis. An axisymmetric diaphragm is a sufficiently accurate representation of the sensor since it is operated below its fundamental resonant frequency. The layers are assumed to have isotropic thermal properties and in perfect thermal contact with continuity of temperature and heat flux across the interfaces. The edge of the diaphragm is assumed to be clamped and at ambient temperature. This temperature boundary condition is based on the high operating frequencies (60-80 *kHz*) at which the diffusion length scale in silicon ($\approx 30\ \mu m$) is significantly smaller than the radius of the diaphragm (500 μm). The clamped boundary condition represents the released diaphragm with its circumference built-in to the silicon substrate. This is an approximation, however, and does not account for the finite compliance of the built-in edge (Gerlach et al. 1996), which can be incorporated in the model if required.

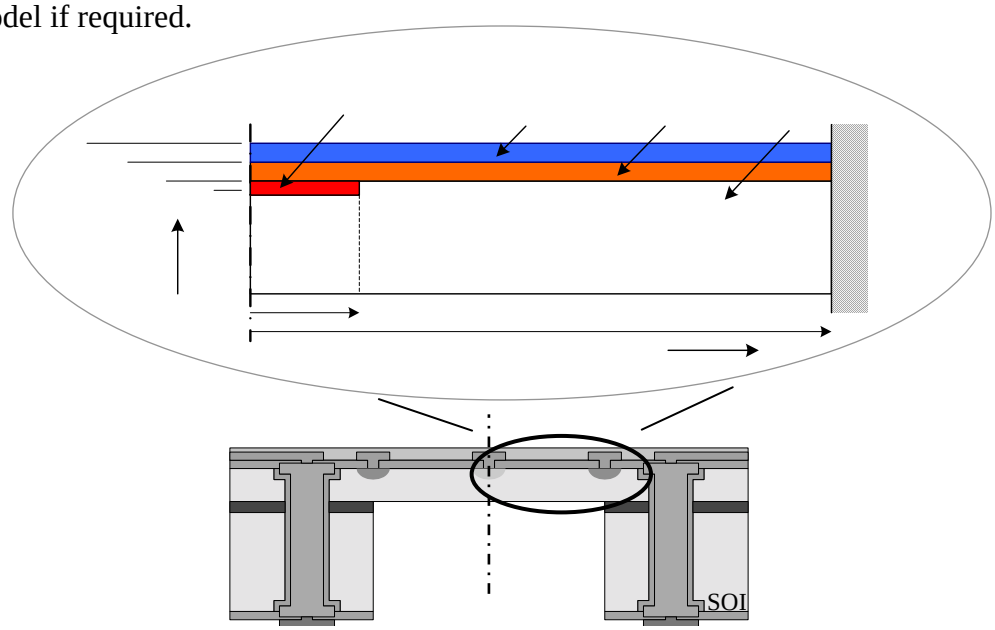

Figure 4-1: Axisymmetric model of the composite diaphragm consisting of three transversely isotropic layers and a diffused resistive heater (H_1, H_2, H_3 and H_{Heat} represent axial distances from the reference plane. The piezoresistors are not represented in the analytical model).

The resistive heater (Figure 4-1) is represented by a time-harmonic internal source of heat generation

$$g(r,z,t) = g_o \int_0^b \delta(r)\, dr \int_{H_{Heat}}^{H_1} \delta(z)\, dz\, \cos(\omega t), \qquad (4.2)$$

where g_o (W/m^3) is the magnitude of the heat source, ω is the angular frequency and δ represents the Dirac delta function. The heater creates a dynamic two-dimensional temperature distribution across the diaphragm. The non-uniform temperature profile through the thickness of the diaphragm generates a thermal force and a moment that results in the transverse vibration of the diaphragm. The flexural-extensional coupling is further enhanced by the composite structure of the diaphragm. Assuming an internal heat source that is an arbitrary function of space allows for a more accurate representation of the exact heater geometry, including the doping profile of the diffused resistor. This was not possible using previous models where the heater was represented by a surface heat flux (Irie and Yamada 1978, Paul and Baltes 1999).

In the following sections, the 2-D temperature distribution in the composite diaphragm is calculated using the Fourier heat conduction model that is then used to derive the thermoelastic forcing functions. The plate governing equations are then formulated using the equations of motion and the linear thermoelastic constitutive relations.

Heat Conduction Model

The governing equation for heat conduction in the i^{th} layer of a multilayered composite diaphragm (Figure 4-1) based on Fourier's law is given by (Ozisik 1993)

$$\alpha_i \left(\nabla^2 T_i(r,z,t) + \frac{1}{k_i} g_i(r,z,t) \right) = \frac{\partial T_i(r,z,t)}{\partial t}, \quad i = 1,2,3 \qquad (4.3)$$

where α_i and k_i represent the thermal diffusivity and the thermal conductivity of the individual layers, $g_i(r,z,t)$ represents an internal heat source within a layer and ∇^2 is the axisymmetric Laplacian operator in cylindrical coordinates,

$$\nabla^2 = \frac{1}{r}\frac{\partial}{\partial r}\left(r\frac{\partial}{\partial r}\right)+\frac{\partial^2}{\partial z^2}. \tag{4.4}$$

Each layer of the composite must satisfy two radial boundary conditions and two transverse boundary conditions. The diaphragm is assumed to be thermally insulated on the top and bottom surfaces,

$$\left.\frac{\partial T_1}{\partial z}\right|_{z=0} = 0 \text{ and } \left.\frac{\partial T_3}{\partial z}\right|_{z=H_3} = 0. \tag{4.5}$$

This is a simplification based on the low free-convective coefficient of air. Additionally, the heat conduction in the diaphragm is assumed to be symmetric about the center, and the edges are maintained at ambient temperature,

$$\left.\frac{\partial T_i}{\partial r}\right|_{r=0} = 0 \text{ and } T_i|_{r=a} = T_\infty. \tag{4.6}$$

The layers are assumed to be in perfect thermal contact denoted by the continuity of temperature and heat flux,

$$T_1 = T_2 \; ; \; k_1\frac{\partial T_1}{\partial z} = k_2\frac{\partial T_2}{\partial z} \text{ at } z = H_1 \tag{4.7}$$

and

$$T_2 = T_3 \; ; \; k_2\frac{\partial T_2}{\partial z} = k_3\frac{\partial T_3}{\partial z} \text{ at } z = H_2. \tag{4.8}$$

The solution to the two-dimensional, transient heat conduction problem described above is obtained using Green's functions and Hankel transforms (details of the derivation are provided in Appendix C)

$$T_i(r,z,t) = \mathrm{Re}\left(\sum_m\sum_n g_o\frac{b}{\varepsilon_m}J_1(\varepsilon_m b)\int_{H_{heat}}^{H_1} Z_1(z')\,dz'\,\frac{2J_o(\varepsilon_m r)}{a^2 J_1^2(\varepsilon_m a)}\,\frac{Z_i(z)}{N(\lambda_{nm})}\left(\frac{e^{j\omega t}}{\lambda_{nm}^2 + j\omega}\right)\right) \tag{4.9}$$

where *a* and *b* are the radius of the diaphragm and the heater respectively, H_1 and H_{Heat} are axial distances from the reference plane to the top and the bottom of the heater, J_o and J_1 are Bessel functions of the first kind, ω is the frequency of the time-harmonic heat source,

$$Z_i(z) = A_i \sin\sqrt{\left(\frac{\lambda_{nm}^2}{\alpha_i} - \varepsilon_m^2\right)}\, z + B_i \cos\sqrt{\left(\frac{\lambda_{nm}^2}{\alpha_i} - \varepsilon_m^2\right)}\, z, \qquad (4.10)$$

λ_{nm} and ε_m are eigenvalues, and *A*, *B* and $N(\lambda_{nm})$ are constants obtained from the boundary and interface continuity conditions. Once the unsteady temperature field is known, the integrated thermal forces and moments can be computed. In the following sections, the transverse vibration of the composite diaphragm resulting from the time-varying two-dimensional temperature distribution is derived.

Plate Equations

The following analysis is based on Kirchoff's plate theory assuming axisymmetric, small deflection and plane stress normal to the thickness direction. The governing equation describing the thermally-forced vibration characteristics of the composite diaphragm is given by (details of the derivation are provided in Appendix C)

$$D^*\nabla^4 w + N_o\nabla^2 w + \rho_A \ddot{w} = \frac{B_{11}}{A_{11}}\left(\nabla^2 N_r^T\right) - \left(\nabla^2 M_r^T\right), \qquad (4.11)$$

where $w(r,t)$ is the transverse deflection, $\ddot{w} = \partial^2 w/\partial t^2$, N_o is the initial in-plane compressive load, ρ_A is the areal density of the composite, $[A] = \int_z [Q]\, dz$ is the extensional stiffness matrix, $[B] = \int_z [Q]\, z\, dz$ is the flexural-extensional coupling matrix,

$[D]=\int_z [Q] z^2\, dz$ is the flexural stiffness matrix, $D^* = D_{11} - \frac{B_{11}^2}{A_{11}}$, N_r^T is the integrated thermal force

$$\begin{bmatrix} N_r^T \\ N_\theta^T \end{bmatrix} = \int_z \gamma\, T(r,z,t)[Q]\, dz, \tag{4.12}$$

M_r^T is the thermal moment

$$\begin{bmatrix} M_r^T \\ M_\theta^T \end{bmatrix} = \int_z \gamma\, T(r,z,t)[Q]\, z\, dz, \tag{4.13}$$

and $\gamma = \gamma_r = \gamma_\theta$ is the coefficient of thermal expansion. For a transversely isotropic material the stiffness matrix is

$$[Q] = \frac{E}{1-\nu^2}\begin{bmatrix} 1 & \nu \\ \nu & 1 \end{bmatrix}, \tag{4.14}$$

where *E* is the Young's modulus and ν is the Poisson's ratio distributions in the composite plate. Equation (4.11) is derived from the strain-displacement relationship, stress-strain relationship and the equations of motion. Although derived for an axisymmetric composite plate, the vector form of Equation (4.11) is the governing equation for the thermally induced vibration of both rectangular and circular plates (Reddy 1996). A flow chart illustrating the sequence of steps in the solution procedure is shown in Figure 4.2. The solution to Equation (4.11) for the case of an axisymmetric circular plate with clamped edges is (details of the derivation are provided in Appendix C)

$$w(r,t) = \mathrm{Re}\left(\left[c_1 J_o(\psi r) + c_3 I_o(\xi r) + \sum_m \sum_n \frac{1}{D^*} \frac{\zeta(\lambda_{nm}, \varepsilon_m)}{\varepsilon_m^4 - \frac{N_o}{D^*}\varepsilon_m^2 - \xi^2 \psi^2} J_o(\varepsilon_m r) \right] e^{j\omega t} \right), \tag{4.15}$$

where

$$\xi^2, \psi^2 = \frac{N_o}{2D^*}\left[\sqrt{1+\frac{4\rho_A \omega^2 D^*}{N_o^2}} \mp 1\right], \tag{4.16}$$

$$c_1 = -c_3\left(\frac{I_o(\xi a)}{J_o(\psi a)}\right) - \sum_m \sum_n \frac{1}{D^*}\left(\frac{\zeta(\lambda_{nm}, \varepsilon_m)}{\varepsilon_m^4 - \frac{N_o}{D^*}\varepsilon_m^2 - \xi^2\psi^2}\right)\left(\frac{J_o(\varepsilon_m a)}{J_o(\psi a)}\right), \tag{4.17}$$

and

$$c_3 = \sum_m \sum_n \frac{1}{D^*}\left(\frac{\zeta(\lambda_{nm}, \varepsilon_m)}{\varepsilon_m^4 - \frac{N_o}{D^*}\varepsilon_m^2 - \xi^2\psi^2}\right)\left(\frac{J_o(\psi a)\, J_1(\varepsilon_m a)\, \varepsilon_m - J_o(\varepsilon_m a)\, J_1(\psi a)\, \psi}{I_o(\xi a)\, J_1(\psi a)\, \psi + J_o(\psi a)\, I_1(\xi a)\, \xi}\right). \tag{4.18}$$

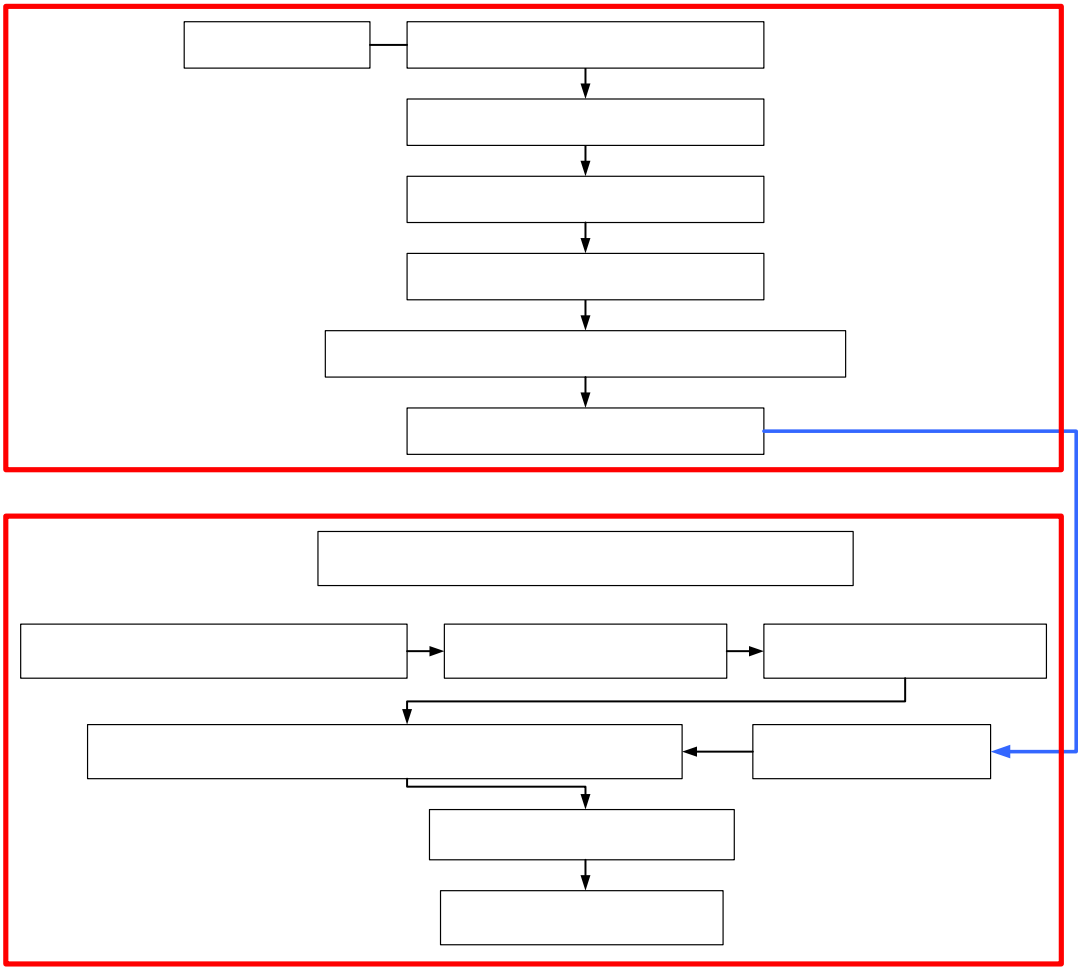

Figure 4-2: A flow chart of the solution procedure.

Results and Discussion

In this section, results from the analytical model are compared with a coupled thermal-mechanical finite element simulation for verification of the model. The material properties, geometry and input parameters used for comparison of the analytical and finite element model are given in Table 4-1. The initial and boundary conditions were identical in both the analytical and finite element model and the effect of static heating on the vibration characteristics of the diaphragm was neglected. The effect of static heating will be discussed later in the chapter.

Table 4-1: Material properties and geometry used in the analytical and finite element models (radius of the diaphragm: 500 μm, radius and thickness of the heater: 30 μm, 0.5 μm, input power: 20 mW at 50 kHz).

	H (μm)	α (10^{-6} m^2/s)	E (GPa), ν	ρ (kg/m^3)	γ (10^{-6} /K)
Silicon (1)	8	94.96	150, 0.27	2330	2.8
Silicon dioxide (2)	0.7	0.59	70, 0.17	2200	0.7
Silicon nitride (3)	0.3	0.90	270, 0.27	3000	2.3

The finite element analysis was performed in ABAQUS® using 8-noded axisymmetric thermally-coupled quadrilateral elements (CAX8T). A total of 60,720 elements were used in the model that represents a well refined mesh. Successive refinement varied the value of the plate vibration amplitude by < 0.1 %. Similarly, a sufficient number of terms were used in the analytical series solutions for temperature (Equation (4.9)) and transverse deflection (Equation (4.15)) to ensure a converged solution. Figure 4-3 shows a plot of the temperature calculated at a specific location (r, z) and time using Equation (4.9) versus the number of terms (m, n) used in the series. The convergence of the analytical solution can be observed for $m, n > 35$.

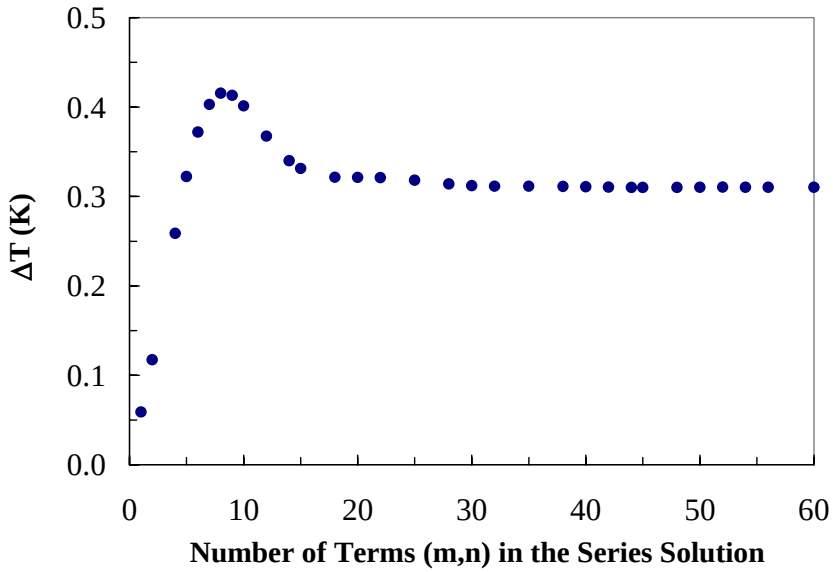

Figure 4-3: Plot illustrating the convergence of the analytical series solution for temperature (calculated at $r = 40\ \mu m$, $z = 4\ \mu m$ and $\omega t = 12\pi/5$)

The time-harmonic temperature distribution in the composite diaphragm obtained from the analytical and finite element models are plotted in Figure 4-4 and shows good agreement between the two models. The initial difference in the temperature is due to a transient effect captured by the finite element model that decays exponentially.

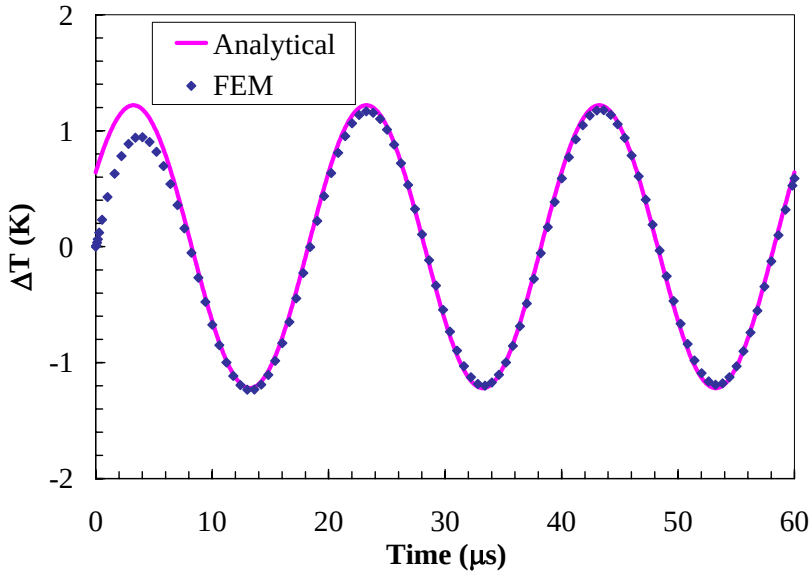

Figure 4-4: Temperature distribution in the composite diaphragm (at $r = 0$ and $H = 0$) as a function of time.

This effect can also be shown using the analytical model, however, the transient solution is based on the artificially forced ambient boundary condition at the edge of the diaphragm, which is an approximation based on a thermal wavelength argument. The correct transient solution will have to involve the surrounding substrate and a continuity (of heat flux) condition at the diaphragm edge. The goal of the analytical model is to study the steady-state response of the diaphragm which agrees well between the two models. In terms of computation time, the analytical model is significantly faster compared to a refined finite element model. For comparison, the time response (3 cycles) of the composite diaphragm to a sinusoidal heat flux input at a single frequency was calculated using the analytical and finite element models on a Pentium 4® processor running at 2.8 *GHz*. For a fixed geometry, the average computation time for the coupled thermal-mechanical finite element analysis is around 80 minutes whereas it takes less than 1 minute to execute the analytical code (in Mathcad®).

A plot of the temperature profile through the thickness of the composite diaphragm at $r = 0$ is shown in Figure 4-5, where the maximum temperature indicates the location of the diffused heater. The plot illustrates the effect of a composite structure on the thermal gradient across the diaphragm. The temperature gradient is largest across the oxide layer (8 – 8.7 μm) due to its poor thermal conductivity, which consequently leads to a larger thermal force and moment compared to a homogenous structure. The radial temperature distribution along the center of the silicon layer is shown in Figure 4-6. The plot indicates a finite slope for the temperature distribution across the diaphragm radius and this effect can be captured only by employing a 2-D heat conduction model. Previously reported thermomechanical models assumed a step profile for the temperature

distribution based on a 1-D heat conduction model and neglected the effects of in-plane heat conduction from the edge of the heater (Irie and Yamada 1978, Lammerink et al. 1992, Paul and Baltes 1999). The effect of in-plane heat conduction is discussed later in this section.

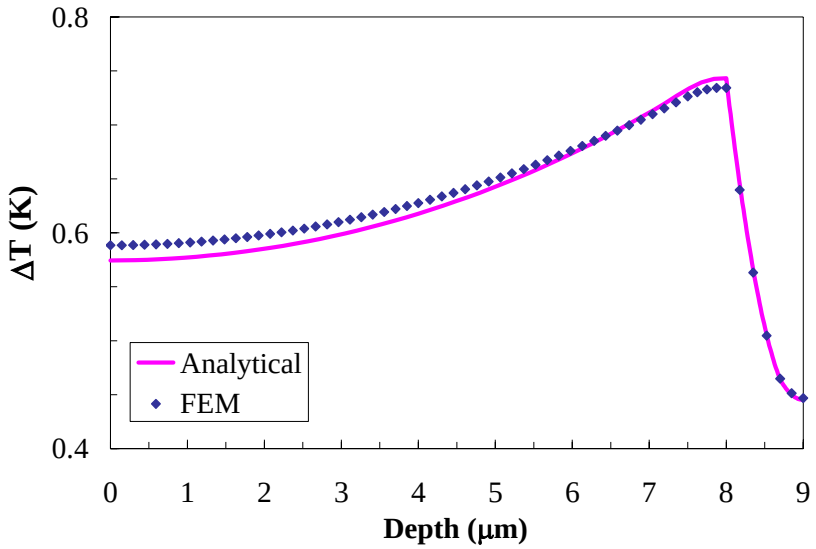

Figure 4-5: Non-uniform temperature profile through the thickness of the composite diaphragm (at $r = 0$).

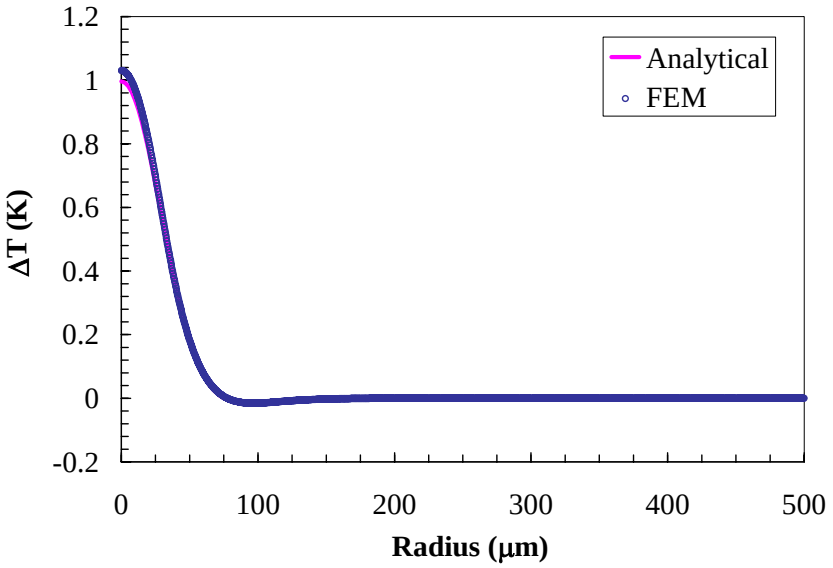

Figure 4-6: Radial temperature distribution in the composite diaphragm along the center of silicon layer.

Figure 4-7 and Figure 4-8 compare the vibration amplitude of the composite diaphragm with the finite element model plotted with respect to time and radius of the diaphragm, respectively. The close agreement between the models is a validation for the simplifying assumptions (Kirchoff's hypothesis, plane stress normal to the z-axis etc) made in the analytical plate model since the finite element model has no such inherent assumptions.

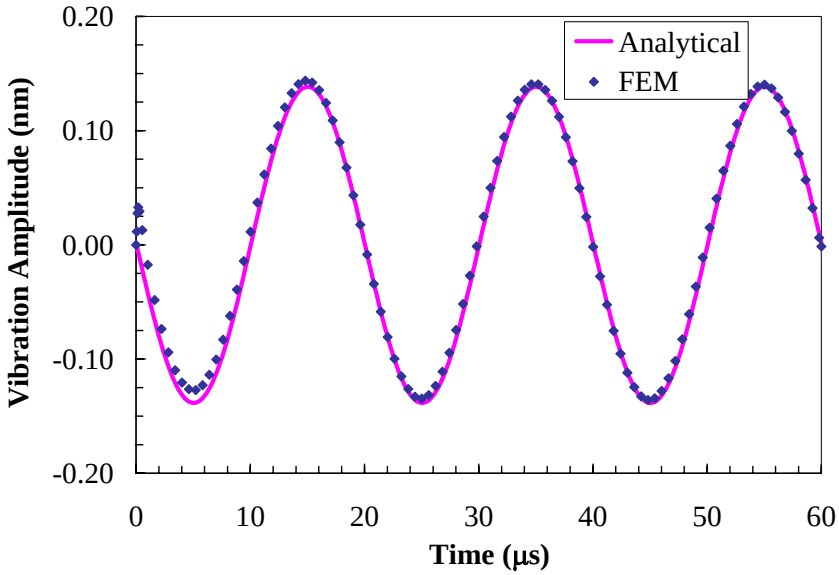

Figure 4-7: Vibration amplitude of the composite diaphragm (at $r = 0$ and $H = 0$) as a function of time.

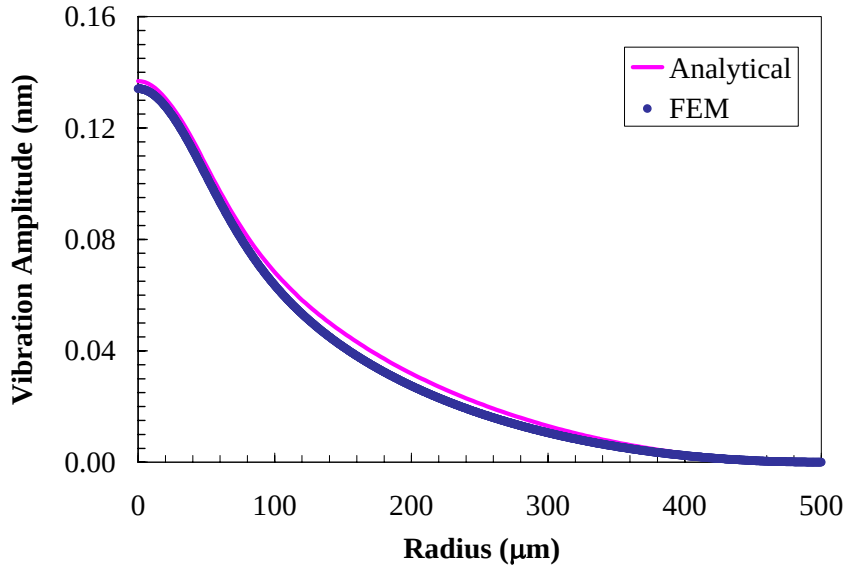

Figure 4-8: Radial variation of the vibration amplitude of the composite diaphragm.

A comparison of the analytical model with an experimental measurement of the diaphragm vibration amplitude is shown in Figure 4-9. The measured vibration amplitude is larger by a factor of 2.7 compared to the analytically predicted value. The observed difference may be attributed to several factors including uncertainties in the material properties, diaphragm aspect ratio, fabrication-induced stresses, temperature distribution in the diaphragm and the compliance of the built-in edge. However, the model still provides a good approximation of the vibration amplitude and may be further improved with more precise measurements of the device parameters.

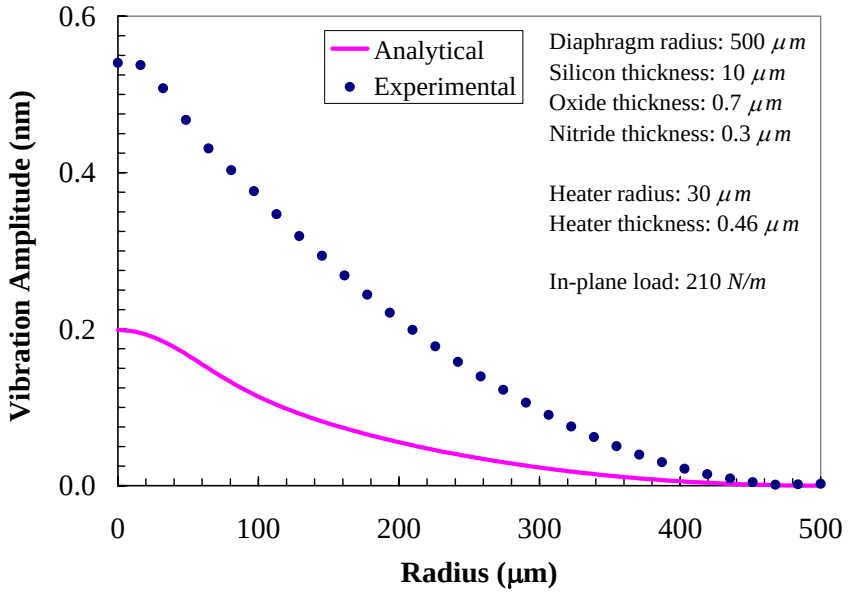

Figure 4-9: Comparison of the analytical model with an experimental measurement of the diaphragm vibration amplitude for an input power of 39 *mW* at 40 *kHz*.

Effect of in-plane heat conduction

While the non-uniform transverse temperature profile generates the integrated thermal force and moment, the in-plane heat conduction also has a significant effect on the vibration amplitude of the diaphragm. Equation (4.11) shows that the forcing functions are proportional to the radial slope and curvature of the thermal force and moment. Previously reported models (Lammerink et al. 1992, Paul and Baltes 1999)

neglected the radial edge effects of the actuating heater by assuming a step profile for the radial temperature distribution. This consequently leads to the use of a delta function (derivative of the step-function) for the slope and its derivative for the curvature. However, as shown by Equation (4.9) and illustrated in Figure 4-6 the temperature distribution in the diaphragm is not independent of the radius and possesses a finite slope and curvature.

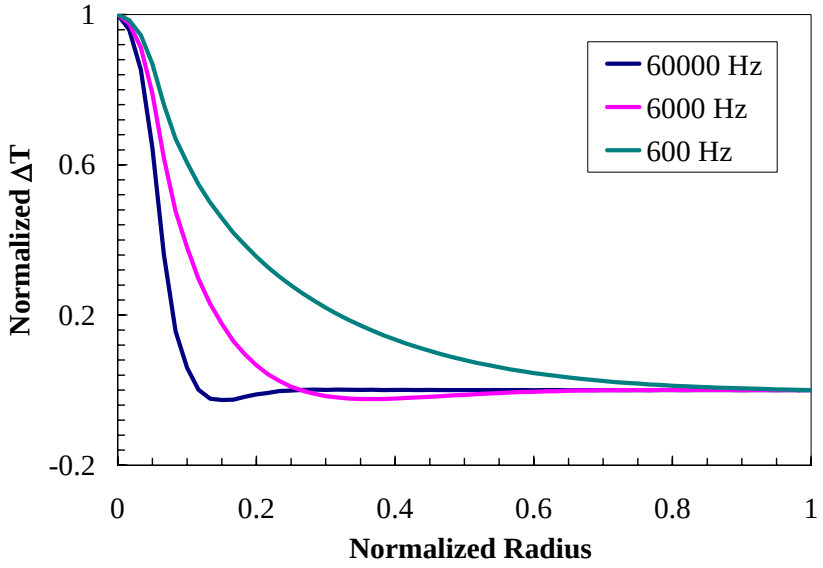

Figure 4-10: Normalized radial temperature distribution at the center of a homogenous silicon diaphragm (500 μm-diameter and 10 μm-thick) as a function of driving frequency.

Therefore, assuming a step function (with infinite slope) for the radial temperature distribution, is an over-simplification and severely over predicts (x500) the vibration amplitude of the diaphragm for a given heat flux input. The radial temperature distribution is also a function of the input frequency and the effect is more pronounced for lower driving frequencies where the variation is more gradual and spread out over a larger radius (Figure 4-10), thus deviating further from the step-profile assumption. The

diffusion length scale even at an operating frequency of 60 *kHz* is not negligible for silicon (~ 30 μm) compared to the heater size (30 μm).

Effect of static heating

As explained in the previous chapter the input power has three components at dc, ω and 2ω due to its quadratic dependence on the excitation voltage and the addition of a dc bias,

$$\left(\bar{V}+V'\sin\omega t\right)^2=\underbrace{\left(\bar{V}^2+\frac{V'^2}{2}\right)}_{P(dc)}+\underbrace{2\bar{V}V'\sin\omega t}_{P(\omega)}-\frac{V'^2}{2}\cos 2\omega t. \quad (4.19)$$

In the model presented above, the sinusoidal steady-state temperature distribution resulting from the dynamic input component at the operating frequency $P(\omega)$ was derived. The effect of the component at 2ω can be minimized by suitably selecting the ratio of the dc and ac voltages. In order to consider the effect of static heating $P(dc)$ the model would have to incorporate the substrate surrounding the diaphragm, which is beyond the scope of the analytical solution. However, the temperature distribution resulting from a combined static and dynamic input power was modeled using finite element techniques. The model used for the analysis is shown in Figure 4-11 and consists of a homogenous silicon diaphragm (500 μm-radius, 10 μm-thick) that is built into the surrounding silicon substrate (2 *mm*-wide and 500 μm-thick). Eight-noded axisymmetric thermally-coupled quadrilateral elements (CAX8T) were used similar to the finite element simulation used to verify the analytical model. The top surfaces of the diaphragm and the surrounding substrate were kept insulated. This is an approximation based on the low conductivity thin films (Table 4-1) deposited over the silicon structural layer. The bottom surface of the diaphragm as well as the sides of the substrate were

prescribed a free-convective boundary condition with a heat transfer coefficient of 5 W/m^2K and an ambient condition was prescribed at the base of the substrate.

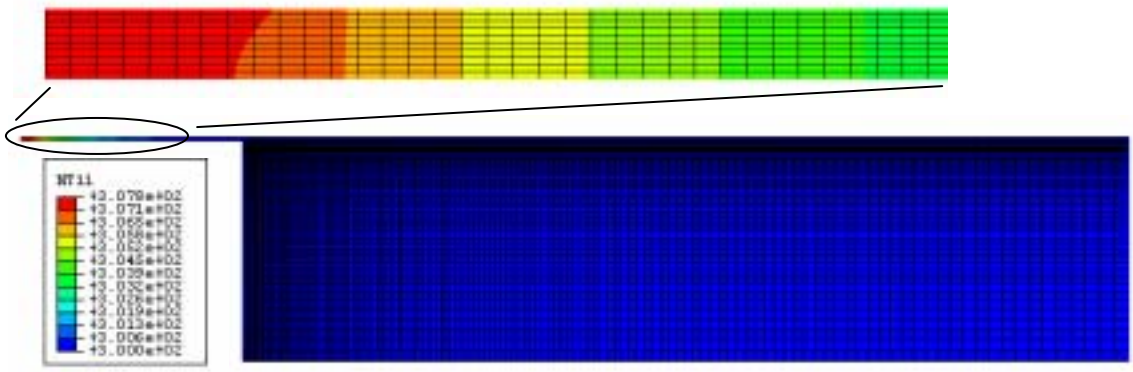

Figure 4-11: Axisymmetric finite element model of a released diaphragm (500 μm-radius, 10 μm-thick) with the surrounding substrate (500 μm-thick), illustrating the temperature distribution due to a combined dc (20 *mW*) and ac (20 *mW* at 50 *kHz*) input.

The structure was initially maintained at ambient temperature (300 *K*) and the subsequent temperature distribution due a combined dc (20 *mW*) and ac (20 *mW* at 50 *kHz*) input to the diffused heater (30 μm-radius, 0.5 μm-thick) was then calculated.

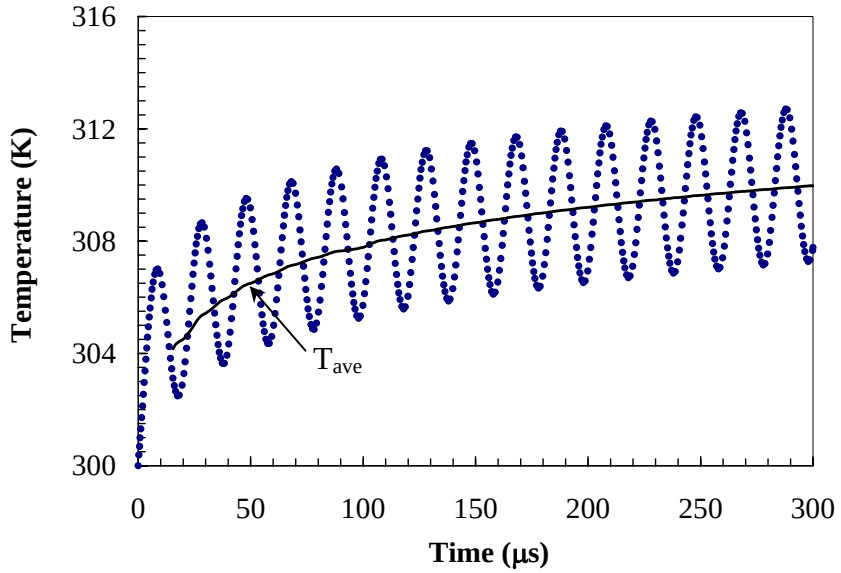

Figure 4-12: Plot of temperature as a function of time at the center of the diaphragm due to a combined dc (20 *mW*) and ac (20 *mW* at 50 *kHz*) input.

The results of simulation are plotted in Figure 4-12 that indicates an average temperature rise (T_{ave}) in addition to a sinusoidal variation with time. The sinusoidal temperature variation is the result of the dynamic power component $P(\omega)$ and the static component $P(dc)$ causes an average temperature rise (T_{ave}) until thermodynamic equilibrium is reached. Thus at steady state conditions, when the average temperature asymptotes to a fixed value, the net effect of the dc component is a static temperature elevation that leads to an increase in the overall compressive loading on the diaphragm and consequently affects its resonant frequency and vibration amplitude. This effect can be incorporated in the analytical model to the first order by appropriately adjusting the value of the in-plane load ($N_o \pm \Delta N_o$).

The analytical model presented in this chapter can also be used to predict the vibration characteristics of beam-type resonators and can be extended to transversely isotropic piezoelectric actuators by substituting the thermal force N^T and moment M^T with equivalent piezoelectric force and moment. The piezoelectric forcing functions are given by

$$\begin{Bmatrix} N_r^P \\ N_\theta^P \end{Bmatrix} = \int_z E_f \, [Q] \begin{Bmatrix} d_{31} \\ d_{31} \end{Bmatrix} dz \tag{4.20}$$

and

$$\begin{Bmatrix} M_r^P \\ M_\theta^P \end{Bmatrix} = \int_z E_f \, [Q] \begin{Bmatrix} d_{31} \\ d_{31} \end{Bmatrix} z \, dz, \tag{4.21}$$

where E_f is the transverse electric field and d_{31} is the piezoelectric coefficient.

In the following sections, the sound radiation from the vibrating diaphragm is investigated using the model of a piston in an infinite baffle.

Generation of Acoustic Waves

In order to determine the sound radiation characteristics of a vibrating microstructure, it is important to calculate the generated acoustic field directly from the forced vibration characteristics of the resonator. To describe the radiation of spherical waves from a region in space, the radiating region can be divided into elements each of which acts as a simple source or a point monopole (Blackstock 2000). The total radiation received at a point $\vec{r}$ is then the sum of radiations from the individual sources. If the radiating region is a bounded surface instead of a volume and the radiation is restricted to the hemisphere in front of the source plane such as a piston set in an infinite rigid baffle the pressure (in the frequency domain) is given by

$$p(\vec{r},\omega) = \iint_s \frac{jk\rho_o c_o\, u(x,y)\; e^{j(\omega t - kR)}}{2\pi R}\, dx\, dy, \qquad (4.22)$$

which is known as the Rayleigh's integral (Blackstock 2000). In Equation (4.22) $R = |\vec{r}' - \vec{r}|$, primed variables represent the location of the source and the unprimed variables represent a field point and $k = \omega/c$ is the wave number. For a circular piston vibrating with a uniform velocity $u(r,\theta) = u_o\, e^{j\omega t}$, the Rayleigh's integral is (Figure 4-13)

$$p(\vec{r},\omega) = \int_0^{2\pi}\int_0^{a} \frac{jk\rho_o c_o\, u_o e^{j(\omega t - kR)}}{2\pi R}\, \sigma\, d\sigma\, d\psi, \qquad (4.23)$$

where $$R = \sqrt{r^2 + \sigma^2 - 2r\sigma\sin\theta\cos\psi}\ . \qquad (4.24)$$

Although Equation (4.23) is an exact solution, it is difficult to integrate analytically. However, if we assume radiation in the far-field the problem is greatly simplified

$$R \approx r\sqrt{1-2\frac{\sigma}{r}\sin\theta\cos\psi+O\left(\frac{\sigma}{r}\right)^2} \approx r-\sigma\sin\theta\cos\psi \qquad (4.25)$$

and Rayleigh's integral reduces to (Blackstock 2000)

$$p(r,\theta,\omega)=\frac{ja\rho_o c_o u_o}{r}\frac{J_1(ka\sin\theta)}{\sin\theta}e^{j(\omega t-kr)}. \qquad (4.26)$$

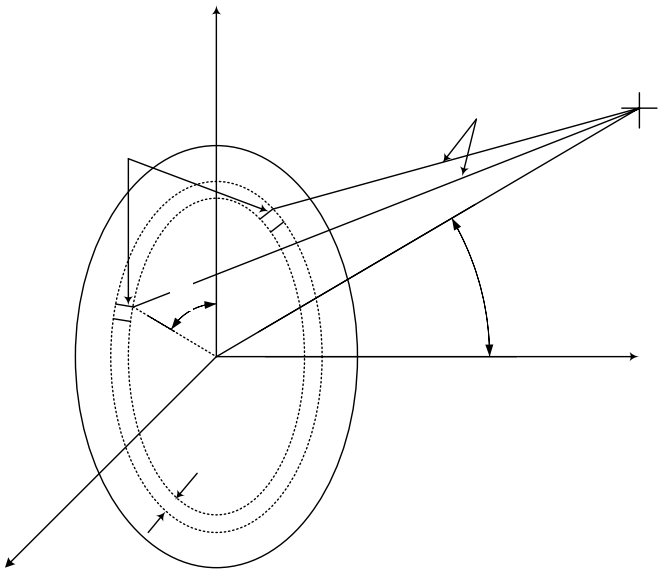

Figure 4-13: Radiation from a circular piston.

In the case of the thermoelastic resonator the transverse velocity is not uniform across the radiating surface. In order to study its sound radiation characteristics it can be modeled using a non-uniform piston. Non-uniform pistons are used to represent radiators that cannot vibrate with a uniform velocity e.g., radiators that are restricted at the edges. For an axisymmetric circular radiator that is clamped at the edge the normal velocity is given by (Blackstock 2000)

$$u_p = 3u_o^{av}\left(1-\frac{\sigma^2}{a^2}\right)^3 e^{j\omega t}, \qquad (4.27)$$

and the corresponding pressure in the far-field is

$$p(r,\theta,\omega)=j\frac{ka^2\rho_o c_o u_o^{av}}{2r}e^{j(\omega t-kr)}\frac{48\,J_3(ka\sin\theta)}{(ka\sin\theta)^3}, \qquad (4.28)$$

where σ is defined in Figure 4-13 and u_o^{av} is the average velocity amplitude. As shown in Figure 4-14 the clamped radiator is a good approximation for the normal velocity distribution of the thermoelastic resonator operated at its resonant frequency.

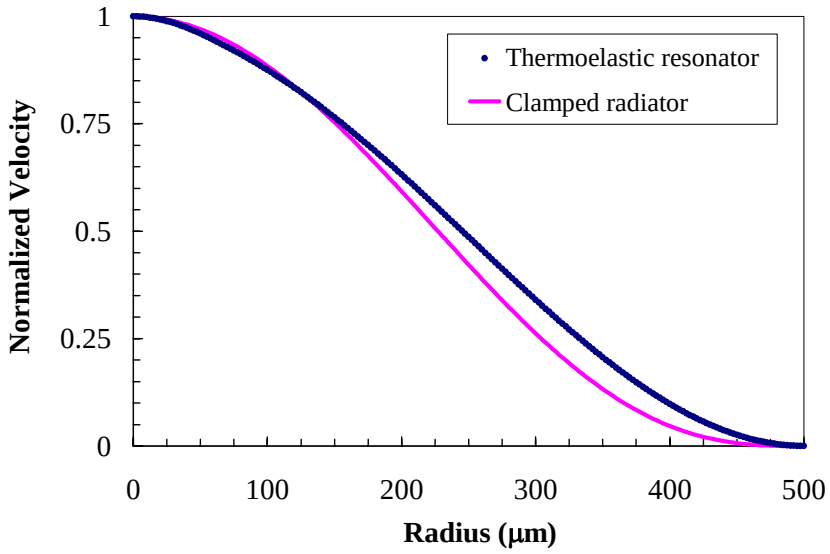

Figure 4-14: Comparison of the normal velocity distribution of the thermoelastic resonator operated at resonance and a clamped radiator.

The directivity of the radiated acoustic field is characterized by the amplitude directivity factor *D*, which is defined as the ratio of pressure at any angle θ to the pressure on the axis of the radiator (θ=0) for a fixed radial distance (Blackstock 2000)

$$D(\theta) = \frac{P(r,\theta)}{P(r,0)}, \tag{4.29}$$

where *P* is the pressure amplitude. For the case of a clamped radiator this results in

$$D(\theta) = \frac{48\, J_3(ka\sin\theta)}{(ka\sin\theta)^3}. \tag{4.30}$$

A graphical representation of the directional characteristics of the clamped radiator for different values of *ka* is shown in Figure 4-15. The plot indicates that the generated acoustic field is nearly omni-directional, if the acoustic wavelength is large compared to

the physical size of the transducer ($\lambda >> a$). With increasing *ka*, the acoustic field becomes more focused towards a small radial region around the axis of the radiator.

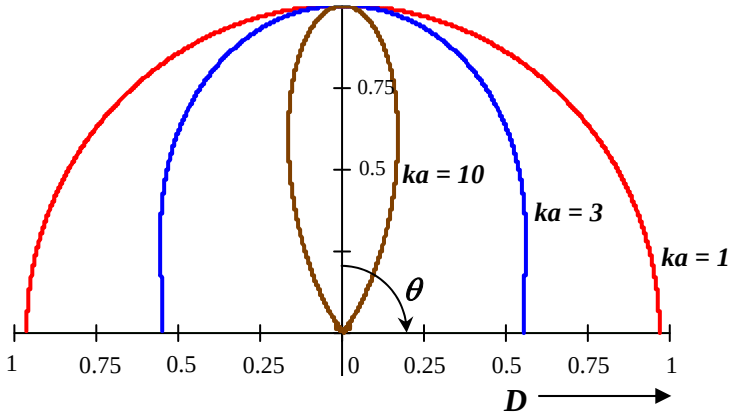

Figure 4-15: Polar plot of the amplitude directivity factor of a clamped circular radiator for different values of *ka*.

For a typical micromachined transducer with a lateral dimension of 1 *mm* and operating at frequencies less than a 100 *kHz*, the generated acoustic field is expected to be omni-directional. To obtain a more directional acoustic source, the lateral dimensions of the transducers can be increased. For example, to obtain 3 dB angle of 20^{o} for the main lobe, corresponding to $ka \approx 10$, a circular transducer operating at 100 *kHz* would need to have a radius of 5 *mm*.

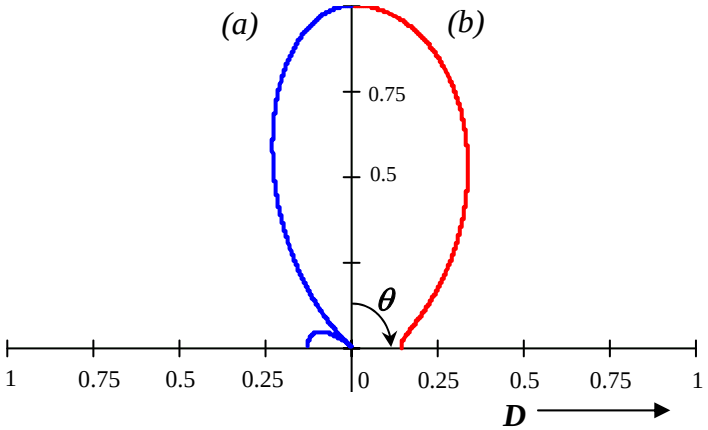

Figure 4-16: Comparison of the directional characteristics of two transducers ($ka = 5$): (a) radiator with uniform vibration amplitude, (b) radiator clamped at the edges.

A side effect of high-*ka* radiators is the presence of several secondary maxima or minor lobes in the radiation pattern (Blackstock 2000). However, non-uniform pistons especially radiators clamped at the edges demonstrate improved sidelobe suppression as indicated in Figure 4-16.

The rest of the chapter deals with the theoretical development of the piezoresistive sensing scheme employed for the detection of acoustic pressure perturbation.

Piezoresistive Sensing

Piezoresistivity is defined as the change in the resistivity of a material due to a change in the mobility (or number of charge carriers) induced by a mechanical strain to the material (Smith 1954). In a piezoresistive sensing scheme, the resistance variation is a linear product of the applied stress and the piezoresistive coefficients π, which are functions of the crystal orientation (Kanda 1982). The large piezoresistivity of monocrystalline silicon, compared to metals strain gauges and its excellent mechanical properties have led to use of piezoresistive silicon sensors to infer parameters such as force, pressure and acceleration.

The discovery of the piezoresistance effect in silicon and germanium (Smith 1954) marked the beginning of silicon-based transducers. Initially, these transducers utilized homogenously-doped silicon strips that were attached to a supporting structure to make use of the higher gage factor of silicon exclusively. The development of diffusion techniques for the fabrication of piezoresistive sensors using single crystal silicon (Pfann and Thurston 1961, Tufte et al. 1962) led to the use of silicon wafers in bending tests with diffused resistors to measure the maximum stress at the surface. The integration of strain gauges into the structure has several advantages (Sze 1994) including a perfect

transmission of strain and the process is extremely suitable for miniaturization and batch fabrication. Advances in bulk micromachining techniques led to the creation of thin compliant membranes by etching away part of the silicon resulting in devices with higher sensitivity. Majority of the commercially available pressure sensors today use silicon piezoresistors (Motorola 1998).

In this section, an overview of the transducer design based on the piezoresistive effect of monocrystalline silicon is presented. A more fundamental description of piezoresistivity including physical models like the many valley model can be found in several references (Kanda 1982, Sze 1994, Senturia 2001).

The normalized change in resistivity, $\Delta\rho/\rho$ for small strains (assuming linear piezoresistive effect) is related to the applied stress by the piezoresistive coefficients, π_{ij}. In crystals with cubic symmetry (e.g., silicon and germanium) the resistivity is a scalar and the piezoresistive coefficient matrix can be can be completely defined using three fundamental piezoresistive coefficients π_{11}, π_{12} and π_{44} (Smith 1954)

$$\frac{1}{\rho}\begin{pmatrix}\Delta\rho_1\\ \Delta\rho_2\\ \Delta\rho_3\\ \Delta\rho_4\\ \Delta\rho_5\\ \Delta\rho_6\end{pmatrix} = \begin{bmatrix}\pi_{11} & \pi_{12} & \pi_{12} & 0 & 0 & 0\\ \pi_{12} & \pi_{11} & \pi_{12} & 0 & 0 & 0\\ \pi_{12} & \pi_{12} & \pi_{11} & 0 & 0 & 0\\ 0 & 0 & 0 & \pi_{44} & 0 & 0\\ 0 & 0 & 0 & 0 & \pi_{44} & 0\\ 0 & 0 & 0 & 0 & 0 & \pi_{44}\end{bmatrix}\begin{pmatrix}\sigma_1\\ \sigma_2\\ \sigma_3\\ \tau_1\\ \tau_2\\ \tau_3\end{pmatrix}, \qquad (4.31)$$

where σ_1, σ_2 and σ_3 represent the normal stresses along the cubic crystal <100> axes and τ_1, τ_2 and τ_3 represent the shear stresses.

In most applications, two special cases of uniaxial stress applied to a long, relatively narrow resistor are utilized. The longitudinal piezoresistive coefficient describes the case of a uniaxial stress applied in the direction of the current and the

transverse coefficient describes the case of a stress applied perpendicular to the direction of the current. The longitudinal and transverse coefficients in terms of the fundamental piezoresistive coefficients and direction cosines are given by (Kanda 1982)

$$\pi_l(\theta) = \pi_{11} - 2(\pi_{11} - \pi_{12} - \pi_{44})(l_1^2 m_1^2 + m_1^2 n_1^2 + n_1^2 l_1^2) \qquad (4.32)$$

and

$$\pi_t(\theta) = \pi_{12} + (\pi_{11} - \pi_{12} - \pi_{44})(l_1^2 l_2^2 + m_1^2 m_2^2 + n_1^2 n_2^2), \qquad (4.33)$$

where (l_1, m_1, n_1) and (l_2, m_2, n_2) are the sets of direction cosines between the longitudinal resistor direction (subscript 1) and the crystal axis, and between the transverse resistor direction (subscript 2) and the crystal axis. The variation of piezoresistive coefficients as a function of orientation on the (100) plane of p-type silicon is shown in Figure 4-17. Using Equations (4.32) and (4.33) the longitudinal and transverse piezoresistive coefficients can be obtained for any orientation of the piezoresistors in the crystal plane.

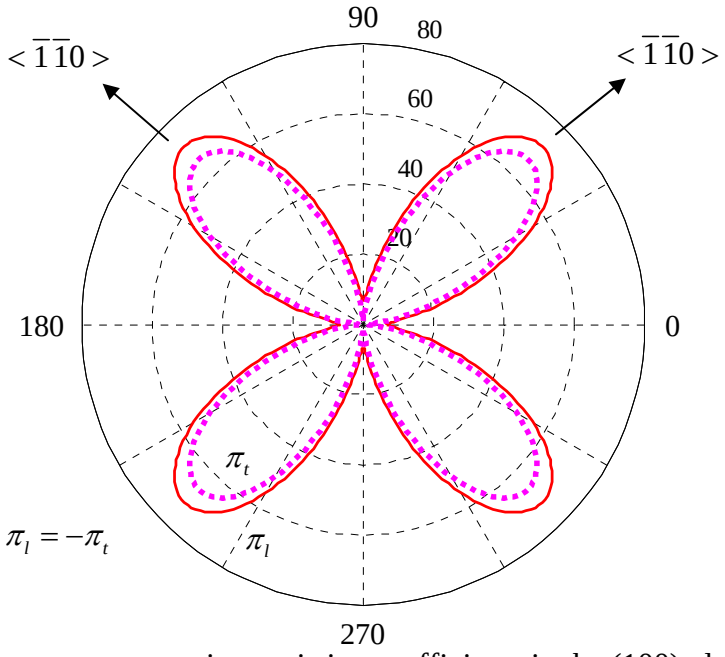

Figure 4-17: Room temperature piezoresistive coefficients in the (100) plane of p-type silicon (10^{-11} Pa^{-1}) (Kanda 1982).

For our particular sensor, p-type piezoresistors were chosen because of their higher sensitivity along the <110> direction (Figure 4-17).In addition, the longitudinal and transverse piezoresistive coefficients are equal in magnitude but opposite in sign along the <110> direction ($\pi_l \approx -1.08\ \pi_t$) making then better suited for full-bridge applications (Senturia 2001).

Typically, four piezoresistors are used in a fully active Wheatstone-bridge configuration driven by a constant voltage source. In such a configuration, the voltage output of the bridge can be linearly related to the acoustic pressure fluctuation provided that the mean resistances in all four legs are equal and that the resistance variation in each resistor of a given leg is equal in magnitude, but opposite in direction (Senturia 2001). For a polar geometry, these conditions are achieved by placing a tapered resistor opposite an arc-shaped resistor (Sheplak et al. 1998). The equations for resistance modulation of the tapered and arc-shaped resistors are given by

$$\frac{\Delta R}{R_{taper}} = \sigma_r(r)\pi_l(\theta) + \sigma_t(r)\pi_t(\theta) \tag{4.34}$$

and

$$\frac{\Delta R}{R_{arc}} = \sigma_t(r)\pi_l(\theta) + \sigma_r(r)\pi_t(\theta)\,, \tag{4.35}$$

where ΔR is the change in resistance of the piezoresistor with initial resistance R under zero load conditions and the subscripts r and t stand for radial and tangential directions respectively with respect to resistor orientation. However, for a resistor of finite dimensions the piezoresistive coefficients and the induced stresses will be different at each point depending on its orientation on the crystal plane and radial location on the diaphragm. In order to account for these variations the resistor has to be discretized and the resistance modulation at each point must be calculated using Equations (4.34) and

(4.35). The overall resistance modulation can then be obtained by adding the resistance changes of the individual elements either in series or in parallel depending on the geometry of the resistor (Sheplak et al. 1998). An iterative process is used to arrive at the optimum arc and tapered piezoresistor sizes that have equal mean resistance values and equal but opposite sign modulations for maximizing sensitivity (details of the procedure are provided in Appendix B).

In order to design diffused piezoresistors, the non-uniform doping profile of the resistor and the non-uniform stress distribution through the diaphragm thickness have to be taken into consideration in addition to surface orientation. According to Kanda (1982), any piezoresistive coefficient can be expressed as a product of the its low-doped room-temperature value π_o and a dimensionless piezoresistance factor *P(N,T)*, which is a function of doping concentration and temperature

$$\pi(N,T) = \pi_o.P(N,T). \qquad (4.36)$$

In the theoretical model proposed by Kanda (1982), the piezoresistive coefficients are weak functions of doping concentration for doping below 10^{19} cm^{-3} and then decrease drastically for higher doping levels (Figure 4-18). According to Harley and Kenny (2000), based on experimental data obtained from several authors, the model is reasonably accurate at low concentrations but substantially underestimates the p-type longitudinal piezoresistive coefficient π_l at higher doping concentrations. A comparison of the theoretical model proposed by Kanda (1982) and the experimental data (at room temperature) by Mason et al. (1962), Tufte and Stelzer (1963) and Kerr and Milnes (1963) is shown in Figure 4-18. For concentration above 10^{17} cm^{-3}, the data is approximated by a straight line on the semilog plot defined by

$$P = \log\left(\frac{b}{P}\right)^{a}, \qquad (4.37)$$

where $a = 0.2014$ and $b = 1.53\ E22\ cm^{-3}$. In designing the piezoresistors of the acoustic transducer, the calculations for the relation between the piezoresistive coefficients and doping concentration were based on the theoretical model by Kanda (1982).

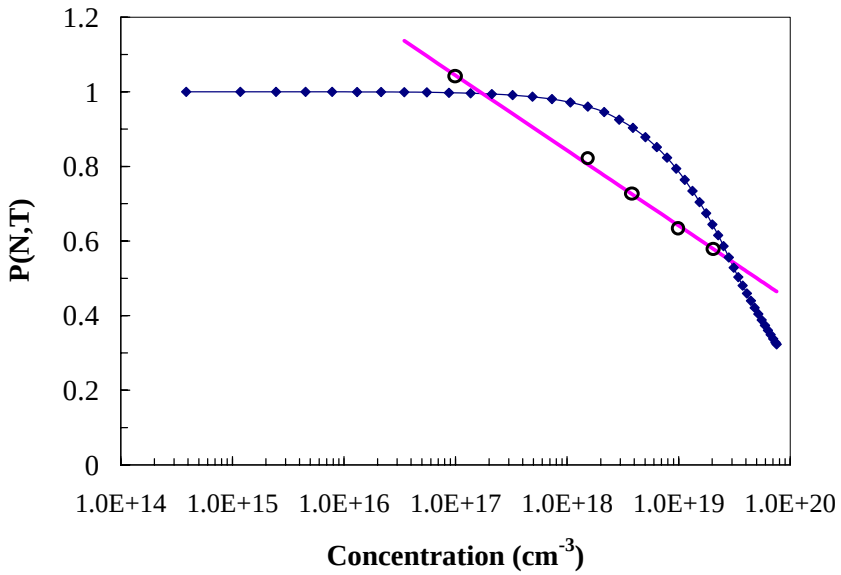

Figure 4-18: Plot of the piezoresistance factor *P(N,T)* as a function of impurity concentration for p-type silicon. The line is based on a theoretical model by Kanda (1982) and the points are experimental data (Harley and Kenny 2000).

In the case of diffused resistors the impurity concentration decreases with depth, ultimately reaching the background concentration. The depth at which the doping concentration of the piezoresistor reaches the background concentration of the substrate is defined as the junction depth. A plot of the doping profile of the piezoresistor with a surface concentration of $10^{20}\ cm^{-3}$ and a junction depth of 0.46 μm, obtained using FLOOPS® (Law and Cea 1998), is shown in Figure 4-19. Since the doping concentration decreases with depth, consequently for a diffused resistor the piezoresistance factor increases with depth as shown in Figure 4-20.

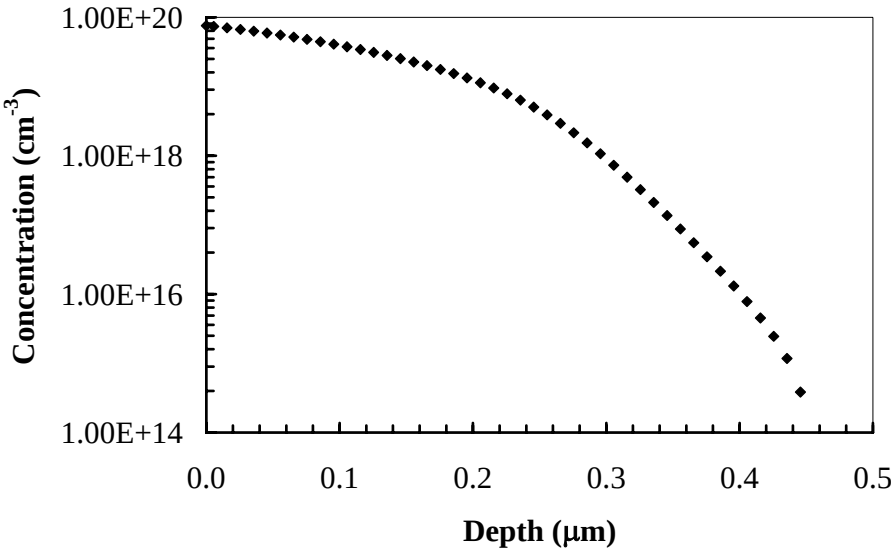

Figure 4-19: Piezoresistor doping profile with a junction depth of 0.46 μm obtained using FLOOPS®.

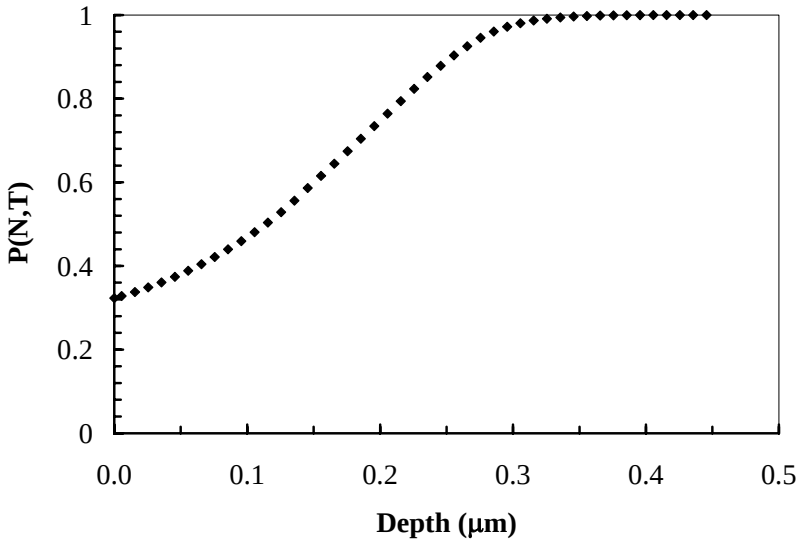

Figure 4-20: Plot of the piezoresistance factor as function of depth of the resistor.

An effective coefficient $\bar{\pi}$ that would yield the same electromechanical behavior as the piezoresistance profile $\pi(z)$ can be defined for the doping profile (Figure 4-19) using *P(N,T)* (Figure 4-17) and Equation (4.36). However, a higher contribution to the effective coefficient is from layers where the current flow is higher, which are near the surface as indicated by Figure 4-21. Therefore, the piezoresistance profile is weighted by

the local conductivity $\zeta(z)$ and the effective piezoresistive coefficient is defined by (Sze 1994)

$$\bar{\pi} = \int_0^{x_j} \pi(z)\sigma(z)\,dz \Big/ \int_0^{x_j} \zeta(z)\,dz, \qquad (4.38)$$

where x_j is the junction depth.

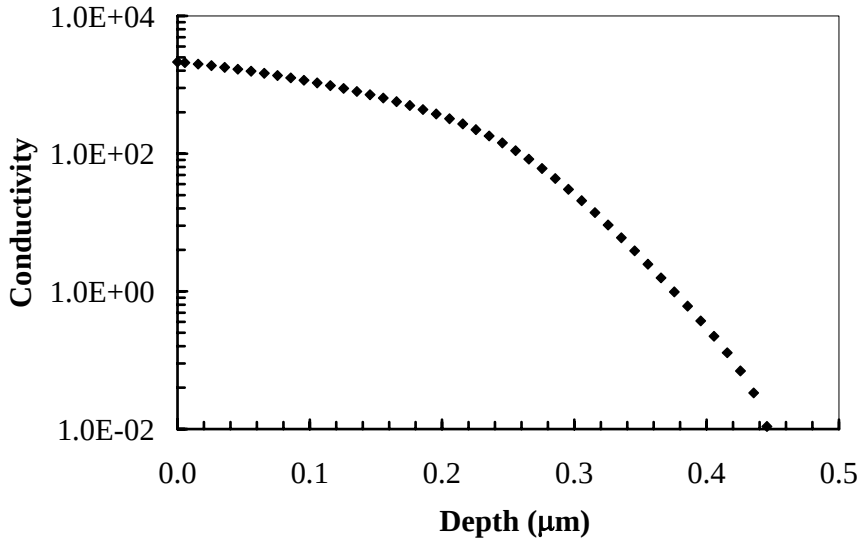

Figure 4-21: Conductivity variation through the thickness of the piezoresistor.

Table 4-2 compares the effective coefficients obtained for the doping profile shown in Figure 4-19 with a surface concentration of 10^{20} cm^{-3} and a background concentration of 10^{14} cm^{-3} with the piezoresistive coefficients of a uniformly low-doped p-type silicon, at room temperature.

Table 4-2: Comparison of the effective piezoresistive coefficients with that of a uniformly low-doped p-type silicon at room temperature (Smith 1954).

Units	10^{-11} Pa^{-1}	10^{-11} Pa^{-1}	10^{-11} Pa^{-1}
Doping profile (Figure 4-19)	$\bar{\pi}_{11} = 2.98$	$\bar{\pi}_{12} = -0.497$	$\bar{\pi}_{44} = 62.4$
Uniform doping	$\pi_{11} = 6.6$	$\pi_{12} = -1.1$	$\pi_{44} = 138.1$

The reduced sensitivity resulting from the high doping concentration is a tradeoff for decreased temperature sensitivity of the piezoresistors (Smith 1954). Since in addition to the dependence on doping levels, the piezoresistive coefficients also vary non-linearly

with temperature (Smith 1954, Tufte and Long 1963). However, at high doping concentrations, the temperature dependence of the piezoresistive coefficients reduces considerably. Tufte and Stelzer (1963) have shown that as doping concentration rises, particularly above $10^{20}\ cm^{-3}$, the piezoresistive coefficients become almost independent of temperature variations between 80 ^{o}C and 100 ^{o}C.

To calculate the resistance modulation of the arc and tapered piezoresistors (using Equations (4.34) & (4.35)) the stress distribution in the silicon diaphragm needs to be investigated. The mechanical behavior of the composite diaphragm is modeled using Kirchoff's plate theory described previously in the chapter. For axisymmetric, small deflections of a composite plate subjected to a combination of in-plane compressive load N_o and a uniform pressure load p, the governing equations in terms of in-plane (u_o) and transverse (w) displacement are (Gururaj 2003)

$$\frac{\partial^2 u_o}{\partial r^2}+\frac{1}{r}\frac{\partial u_o}{\partial r}-\frac{u_o}{r^2}=-\frac{B_{11}}{A_{11}}\frac{1}{D^*}r\left(\frac{p}{2}+\frac{N_o}{r}\frac{\partial w}{\partial r}\right) \tag{4.39}$$

and

$$\frac{\partial^3 w}{\partial r^3}+\frac{1}{r}\frac{\partial^2 w}{\partial r^2}-\frac{1}{r^2}\frac{\partial w}{\partial r}=-\frac{N_o}{D^*}\frac{\partial w}{\partial r}-\frac{pr}{2D^*}. \tag{4.40}$$

Equations (4.39) and (4.40) are solved analytically to obtain an expression for the in-plane and transverse plate displacements

$$u_o(r)=-\frac{B_{11}}{A_{11}}\frac{1}{D^*}\frac{p}{2}\frac{a^2}{k^2}\left(r-a\frac{J_1\left(\frac{kr}{a}\right)}{J_1(k)}\right) \tag{4.41}$$

and

$$w(r)=\frac{1}{D^*}\frac{pa^4}{4k^2}\left[\left(\frac{a^2-r^2}{a^2}\right)-\frac{2}{k}\left(\frac{J_o\left(\frac{kr}{a}\right)-J_o(k)}{J_1(k)}\right)\right], \tag{4.42}$$

where

$$k^2 = \frac{N_o a^2}{D^*} \tag{4.43}$$

is the compression parameter. The radial and circumferential stress components are

$$\sigma_{rr}(r,z) = \frac{E}{1-\nu^2}\left\{ -\frac{B_{11}}{A_{11}}\frac{1}{D^*}\frac{pa^2}{2k^2}\left(1+\nu+\frac{\frac{a}{r}J_1\left(\frac{kr}{a}\right)(1-\nu)-J_o\left(\frac{kr}{a}\right)k}{J_1(k)} \right)+ z\frac{p}{2N_o}\left(1+\nu+\frac{\frac{a}{r}J_1\left(\frac{kr}{a}\right)(1-\nu)-kJ_o\left(\frac{kr}{a}\right)}{J_1(k)} \right) \right\}$$

and (4.44)

$$\sigma_{\theta\theta}(r,z) = \frac{E}{1-\nu^2}\left\{ -\frac{B_{11}}{A_{11}}\frac{1}{D^*}\frac{pa^2}{2k^2}\left(1+\nu+\frac{(\nu-1)\frac{a}{r}J_1\left(\frac{kr}{a}\right)-\nu J_o\left(\frac{kr}{a}\right)k}{J_1(k)} \right)+ z\frac{p}{2N_o}\left(1+\nu+\frac{(\nu-1)\frac{a}{r}J_1\left(\frac{kr}{a}\right)-\nu k J_o\left(\frac{kr}{a}\right)}{J_1(k)} \right) \right\}. \tag{4.45}$$

The stress distribution in a clamped circular plate subjected to an in-plane compressive stress of 300 *MPa*, induced by the thermal oxide layer, and a uniform pressure load of 200 *Pa* is plotted in Figure 4-22. In order to achieve maximum sensitivity to acoustic pressure perturbations, the effective placement of the piezoresistors in regions of maximum strain is crucial. The plot indicates that the maximum radial stress is at the clamped edge and decreases towards the center of the diaphragm with the inflection point at ≈ 0.3 *mm*. The corresponding circumferential stress also has to be considered for equal and opposite resistance modulation of the arc and tapered resistors.

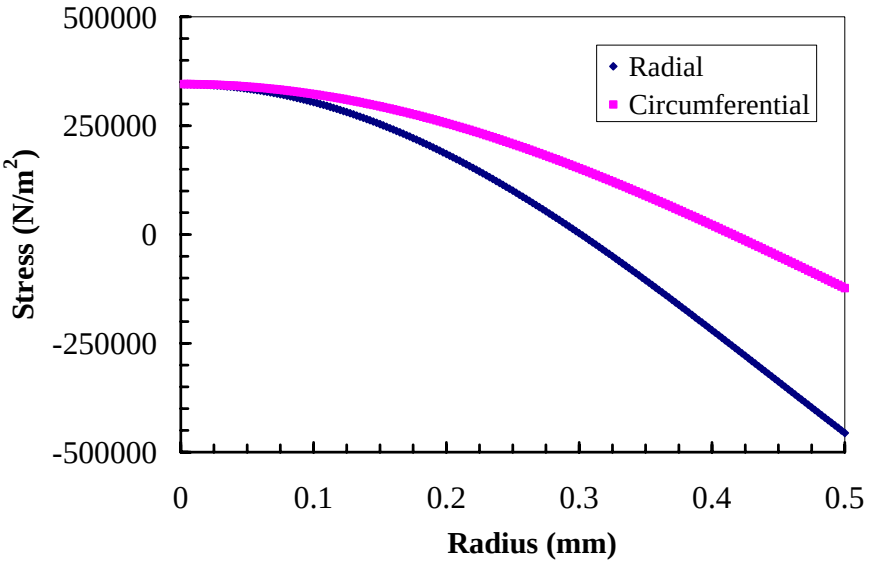

Figure 4-22: Radial and circumferential stress distribution in the composite diaphragm subjected to in-plane (300 *MPa*-compressive) and transverse (200 *Pa*) loading.

An iterative process is used to arrive at the final geometry and placement of the piezoresistors.

CHAPTER 5
EXPERIMENTAL CHARACTERIZATION

This chapter presents a detailed description of the experimental set-up used to characterize the acoustic proximity sensor and the electrical through-wafer interconnects. Device characterization included measurements of the current vs. voltage characteristics of the diffused piezoresistors and the ETWI, electrical isolation characteristics of the silicon dioxide layer surrounding the ETWI, overall noise floor, vibration and sound radiation characteristics and the response of the diaphragm to acoustic pressure perturbation. These measurements have been broadly classified as electrical, mechanical and acoustic characterization and are detailed in the following sections.

Electrical Characterization

Electrical characterization included current vs. voltage measurements to investigate the ohmic behavior of the diffused resistors and the ETWI, capacitance vs. voltage measurements to test the isolation characteristics of the silicon dioxide insulating the ETWI, and measurement of the overall device noise floor. To enable the electrical testing of the ETWI and to extract average properties, several test structures consisting of chains of interconnects connected by surface polysilicon lines were fabricated.

Current vs. Voltage Characteristics

Current vs. voltage (I-V) measurements were performed on the diffused resistors and on different ETWI chains to determine the resistance of the diffused piezoresistors and the average interconnect resistance. An interconnect chain consists of several ETWI (specifically 6, 22, 62 and 100) connected in series by surface polysilicon lines patterned

on the top and bottom surfaces of the wafer (Figure 5-1). Separate test structures were also fabricated to estimate the resistance of the surface polysilicon lines, which is later subtracted from the overall resistance of the chain to compute the average interconnect resistance.

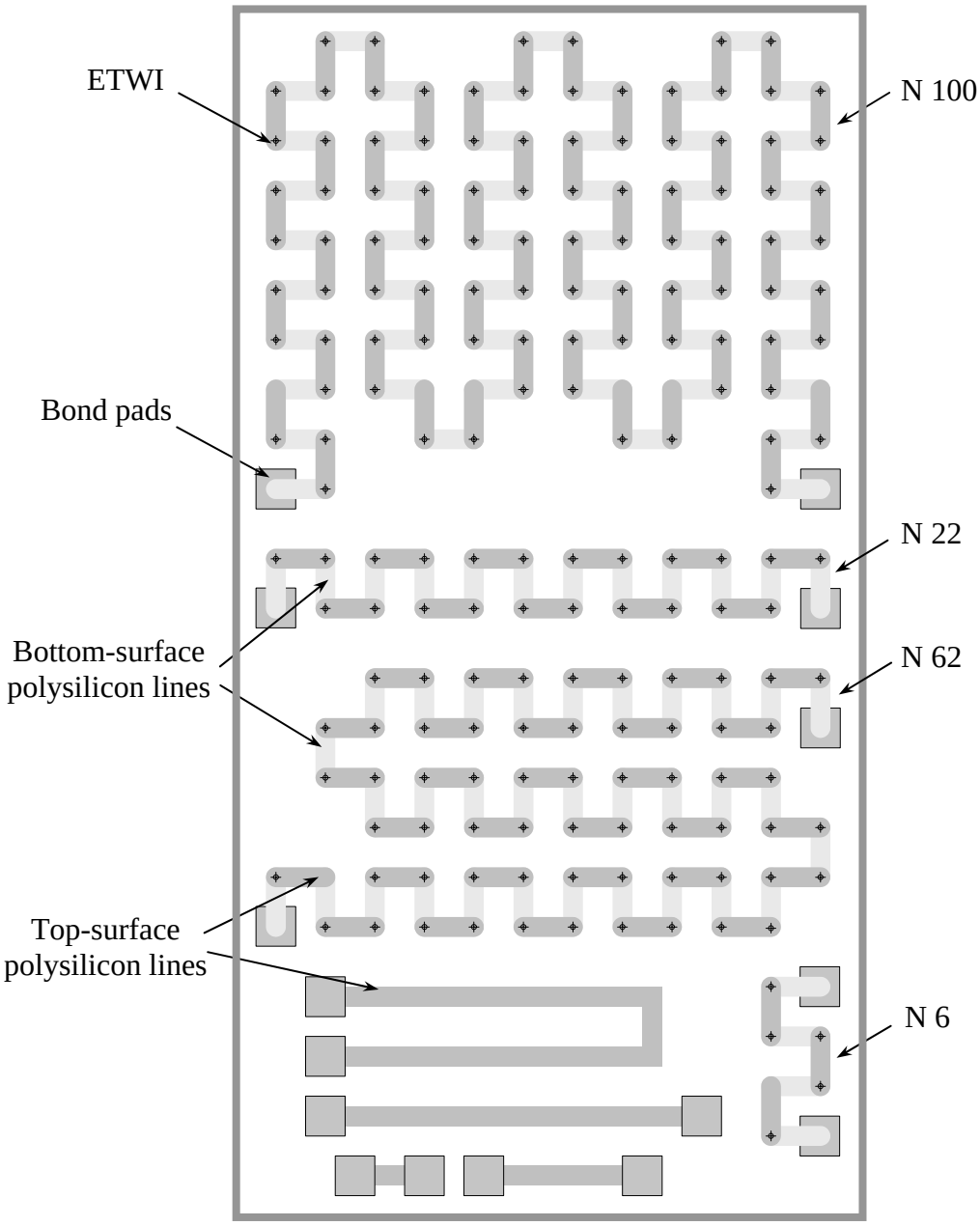

Figure 5-1: Chain of 6, 22, 62 and 100 ETWI connected in series via surface polysilicon lines (dark and bright lines indicate the top and the bottom surface of the wafer respectively).

In addition, I-V measurements were also obtained across the pn junction formed between the diffused resistors and the silicon substrate to obtain its forward and reverse bias characteristics. The reverse bias characteristics of the pn junction determine the leakage current from the junction-isolated resistors into the substrate. Minimal leakage is essential for effective Joule heating of the diaphragm and low piezoresistor noise floor. All measurements were made using a Hewlett Packard 4155B semiconductor parameter analyzer and a wafer level probe station using bias voltages ranging from –10 *V* to 10 *V* with 0.1 *V* increments, while monitoring the current at each voltage step.

Capacitance vs. Voltage Characteristics

Interconnect capacitance affects the propagation delay of signals as well as the capacitive loading of the sensor output. The p-type polysilicon interconnect dielectrically isolated from the n-type substrate forms a metal-oxide-semiconductor capacitor (MOSC) where the polysilicon acts as a metal gate and the silicon layer is the substrate. The voltage-dependent MOSC capacitance was characterized using a Hewlett Packard 4294A vector impedance meter with a 1 *MHz* small signal frequency. Similar to the I-V characterization, the bias voltage (in this case, across the ETWI and the substrate) was swept from –20 *V* to 20 *V* with 0.1 *V* increments, while monitoring the capacitance at each voltage step. An open and short circuit calibration, prior to the measurements, was performed with the vector impedance meter to eliminate the capacitive contribution of the connecting leads and the test setup.

Noise Floor Spectra

The study of the electrical noise floor of a device is required to determine the minimum detectable signal (MDS). Measurements of the noise power spectral density (PSD) were made in a Faraday cage (Figure 5-2) using low-noise test equipment. The

aim of the experimental setup was to isolate the random physical noise of the device under test from deterministic interference (Bhardwaj 2001). Deterministic sources arise from capacitive coupling of electromagnetic interference (EMI) to the device and cabling, with the ac power line being the major contributor (60 *Hz* and its harmonics). The purpose of shielding is to isolate the internal signal path by intercepting the capacitive current and shunting it to ground (Bhardwaj 2001). The Faraday cage considerably reduced the interference, permitting analysis of the noise PSD.

The sensor was configured similar to the operating conditions with a 9 *V* bias across the Wheatstone bridge. As illustrated in Figure 5-2, a battery powered Stanford Research Systems SR560 differential amplifier with specified noise voltage of 4 $nV/\sqrt{Hz}$ was used to amplify the differential voltage from the bridge with a gain of 10,000. This in conjunction with a battery (9 *V*) as the voltage source minimizes the 60 *Hz* line interference. The differential measurement technique rejects the common contamination signal in the two inputs.

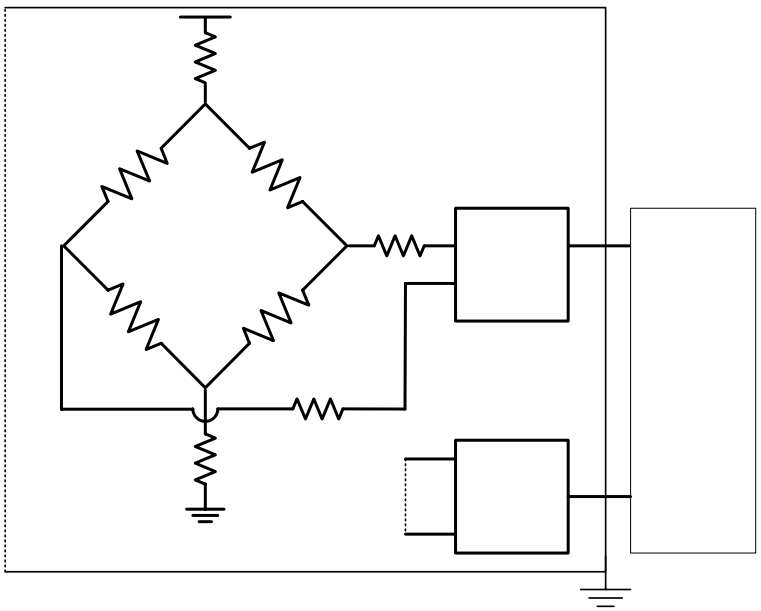

Figure 5-2: Schematic representation of the device noise measurement setup.

After proper grounding of all measurement equipment, the noise PSD was measured using a SR785 dynamic spectrum analyzer using 500 averages. In order to prevent any offset voltage the different grounds namely, the signal ground, the ground of the power supply and the ground of the instrumentation were maintained at the same potential. In order to maintain sufficient resolution at low frequencies, a low frequency range of 0-1.6 *kHz* with a 2 *Hz* bin was used. This frequency resolution effectively confines the 60 *Hz* power line interference and its harmonics to the measurement bins and prevents it from being spilled into adjacent frequency bins. Once isolated these samples can be filtered out, this technique is referred to as selective filtering. Larger frequency ranges of 25.6 *kHz* with 8 *Hz* bin were used for the higher frequencies. In order to extract the device noise floor, the set-up noise PSD was measured by shorting the differential outputs of the amplifier and was subtracted from the total noise PSD

$$PSD_{DUT} = \sqrt{PSD^2 - PSD_{EMI}{}^2}. \qquad (5.1)$$

Mechanical Characterization

Mechanical characterization involved investigating the effects of diaphragm geometry and fabrication induced stresses on the resonant frequency, vibration amplitude and buckling behavior of the diaphragm. Measurements of the mechanical characteristics of the diaphragm were obtained using optical interferometric techniques.

The sensors were excited using a combination of ac (7 V_{pk}) and dc (7 *V*) voltages. The vibration amplitude of the diaphragm was then measured using a Polytec PI scanning laser vibrometer (MSV 300) in combination with a Stanford Research Systems (SR785) spectrum analyzer. The laser vibrometer uses an optical interferometric technique to enable non-contact measurement of surface vibrations. The operation of the vibrometer

is based on a helium neon laser that is focused on the vibrating diaphragm and is subsequently scattered back and coupled into the interferometer. The interferometer compares the phase and frequency of the object beam (reflected from the vibrating surface) with that of the internal reference beam. The frequency difference corresponds to the instantaneous velocity and the phase difference is proportional to the instantaneous position of the vibrating surface. Measurements of the transverse vibration of the acoustic resonator were made by fitting the vibrometer onto an Olympus microscope with a 10x objective producing a laser spot size of 20 μm on the diaphragm surface and by scanning the laser across the entire diaphragm exact vibration mode shapes were obtained.

The compressive stresses generated in the thermal oxide layer (Madou 1997), due to a difference in the thermal expansion coefficients of silicon and silicon dioxide, can cause buckling of the thin diaphragms if the net in-plane load exceeds the critical buckling load (Leissa 1993, Soderkvist and Lindberg 1994). Buckling is characterized by a static deflection of the diaphragm and was observed for diaphragms below a thickness of 8 μm. The dependence of buckling height on the aspect ratio of the diaphragm, for a fixed value of the in-plane compressive stress, was characterized using a Wyko optical profilometer (NT1000)[€].

In addition, the static heating of the diaphragm induces additional compressive stresses that can alter its buckled height, resonant frequency and vibration amplitude. The effect of varying static power on the static and dynamic behavior of the diaphragm was also characterized using the vibrometer and the optical profilometer.

[€] The NT1000 is courtesy of University of Florida's Major Analytical Instrumentation Center (MAIC). URL: http://www.mse.ufl.edu/~maic/Wyko.htm.

Acoustic Characterization-Receiver

The dynamic response of the sensor to acoustic pressure perturbation was characterized in a plane wave tube (PWT) (Chandrasekaran et al. 2000). The PWT consists of a rigid-walled duct that supports planar (0,0 mode) acoustic waves propagating along the length of the duct. For linear lossless acoustic motion in a rigid-walled square duct, the fundamental mode (0,0) or the plane wave propagates at all frequencies. The higher order modes can propagate only when the width of the duct is greater than half the acoustic wavelength $\left(D < \lambda/2\right)$ (Rossi 1988). Therefore, below the first cut-on frequency ($f < c_o/2D$), the duct will propagate only plane waves and the higher order modes are evanescent. Thus, sensors placed at the same axial location from the acoustic driver sense the same acoustic pressure field. This permits the calibration of an acoustic sensor by comparing the output to a reference microphone with a known response.

The sensors were calibrated in two different PWTs, a 25.4 *mm* x 25.4 *mm* normal incidence PWT and an 8.5 *mm* x 8.5 *mm* grazing incidence PWT. The sensor and a reference microphone (Brüel and Kjær Type 4138) were flush mounted at the same axial distance from the acoustic driver. The sensor was biased at 9 *V*, and the differential output of the Wheatstone bridge was connected to a SR560 preamplifier. The amplified signal was then fed into a SR785 dynamic spectrum analyzer for data processing.

The low-frequency cut-on for the first non-planar (1,0), (0,1) mode is 20 *kHz* for the grazing incidence PWT and 6.7 *kHz* for the normal incidence tube. Thus, the usable bandwidth is limited to 20 *kHz* and 6.7 *kHz* respectively.

The normal incidence PWT was also used to measure the linear response of the sensor to varying sound pressure level. Measurement of the device linearity is required to determine the dynamic range of operation of the sensor. In a proximity-sensing scheme, the transmitter, typically an under-damped second-order system, can have a gain of greater than 40 *dB* at resonance and a linear response of the receiver over the entire range would be required for spectral analysis of the measured signal. A 1 *kHz* tone at varying amplitudes, monitored by the reference microphone, was used to excite the sensor, which was biased at 9 *V*. The rms output voltage of the sensor at each sound pressure level was recorded.

Acoustic Characterization-Transmitter

The end application requires an array of sensors to be used in a network to monitor the state of the entire cavity surrounding the HSSV. When used as an array, minimal cross-talk between the sensors is required for efficient real-time monitoring. Cross-talk refers to the portion of the acoustic radiation that reaches the receiver directly from the transmitter. The directional behavior of the generated acoustic field and the spacing between the sensors will determine the cross-talk. The acoustic field generated by the vibration of the thermoelastically actuated diaphragm was characterized in a free-field environment. In order to characterize the transmitted acoustic field, two sets of measurements were obtained. In both cases, the transmitting sensor was fixed and oriented such that the diaphragm surface is vertical. The transmitter was then excited with a combination of harmonic ac (9 V_{pk}) and dc (9 *V*) voltages. The acoustic field was measured using a Brüel and Kjær Type 4138 microphone. To measure the directionality of the generated acoustic field, the microphone was positioned at a fixed radial distance of 25 *mm* from the transmitter and a jig was constructed that allowed the microphone to

be revolved around the transmitter at the fixed radius. Sound pressure measurements were made at 2^o intervals, from 0^o to 90^o, averaged, and recorded.

To obtain the variation of sound pressure level with distance from the transmitter, the microphone was positioned directly opposite the transmitter on a single axis traverse with a precision of 1 μm. The initial position was set at 3 *mm* from the transmitting diaphragm and then varied to 50 *mm* along the axis of the diaphragm. At each position, sound pressure measurements were obtained using the microphone and a spectrum analyzer.

Proximity Sensing

A continuous-wave phase-shift technique (Li et al. 2002) was used to demonstrate proof-of-concept proximity sensing using the micromachined transducer as the acoustic transmitter. The transducer and a microphone (Brüel and Kjær Type 4138) were positioned on a 1-D traverse with a precision of 1 μm facing a sound hard boundary, which was initially set at a distance of 20 *mm*. The amplitude and phase of the acoustic waves generated by the transducer (operating at 69 *kHz*) and subsequently reflected from the boundary was recorded using the microphone, while altering the distance between the transducer/microphone and the boundary. The distance moved by the boundary is then calculated from the measured phase-shift after subtracting the cross-talk between the transducer and the microphone. In order to estimate the cross-talk the sound hard boundary was removed and the magnitude and phase of the acoustic radiation was measured using the microphone. The phase of the vector difference between the two measurements (with and without the boundary) corresponds to the phase of the reflected wave.

CHAPTER 6
RESULTS AND DISCUSSION

This chapter presents the results from the electrical, mechanical and acoustic characterization of the acoustic transducer/ETWI. These include current vs. voltage characteristics of the diffused resistors, resistor/substrate (pn) junction and the ETWI, capacitance vs. voltage characteristics of the oxide insulating the ETWI, overall device noise floor, diaphragm vibration characteristics as well as acoustic transmitting and receiving characteristics. Devices with varying diaphragm thicknesses and with front and backside contacts were tested (Table 6-1).

Table 6-1: List of devices used for the characterization (The thickness of the silicon dioxide and silicon nitride layers are 0.7 *!m* and 0.3 *!m* respectively).

Device label	Thickness of the silicon layer (*!m*)
C1 (front-side contacts)	10
C3 (with ETWI)	8
C9 (front-side contacts)	5

Electrical Characterization

Current vs. Voltage Characteristics

The reverse bias characteristics of the pn junction formed between the boron-doped piezoresistors and the n-type silicon substrate determines the leakage current from the resistors into the substrate. Minimal leakage is essential for effective Joule heating of the resistors as well as low piezoresistor noise floor. Results of the I-V characterization (Figure 6-1) indicate negligible leakage current (< 14 *pA*) up to a reverse bias voltage of 10 *V*. The small current value in the forward bias mode (deviating from the ideal diode

10 *V*. The small current value in the forward bias mode (deviating from the ideal diode behavior) is due to the large series resistance of the lightly doped silicon substrate. The reverse bias breakdown voltage for the pn junction is greater than 30 *V* as shown in Figure 6-2.

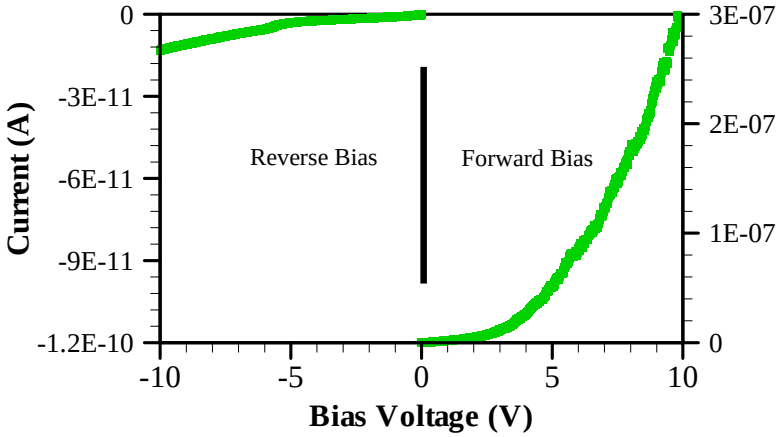

Figure 6-1: Forward and reverse bias characteristics of the pn junction, indicating negligible leakage current (< 14 *pA* at -10 *V*) (Device C3).

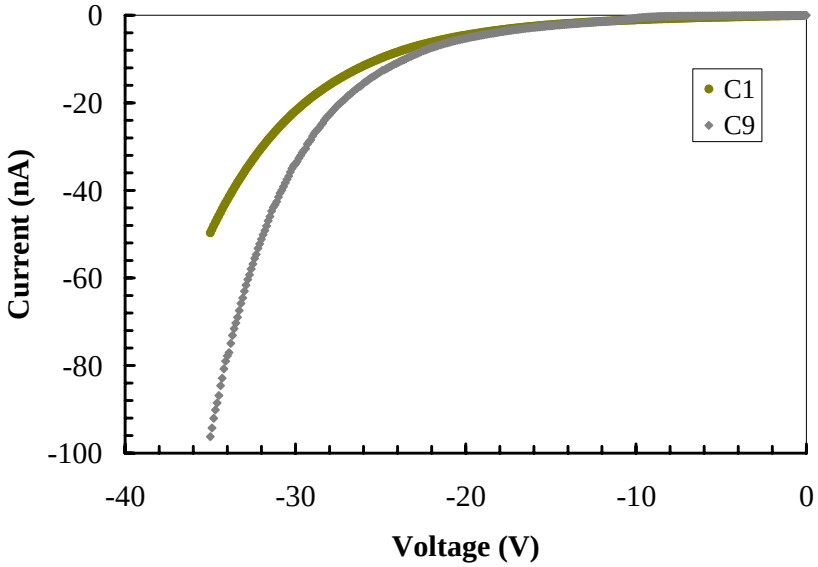

Figure 6-2: Reverse bias breakdown voltage of the pn junction for devices C1 and C9.

I-V measurements across the diffused resistors indicate an average resistance of around 2350 Ω for the actuating heater, 6300 Ω for the arc resistor and 7300 Ω for the

tapered resistor. The resistance values obtained for the different devices are tabulated in Table 6-2.

Table 6-2: Resistance of the diffused resistors (in $k\Omega$).

Device	Arc 1	Taper 1	Arc 2	Taper 1	Heater
C 1	6.26	7.46	6.13	7.34	2.34
C 3	6.55	7.44	6.64	7.14	2.62
C 9	6.29	7.53	6.07	7.76	2.10
Average	6.33	7.35	6.28	7.27	2.35
Theoretical	4.62	4.62	4.62	4.62	1.50

The interconnects display ohmic behavior as indicated by the linear variation of current and voltage in Figure 6-3. Average resistance values ranging from 10 Ω to 14 Ω were obtained for each interconnect depending on the thickness of the doped polysilicon layers (Figure 6-4).

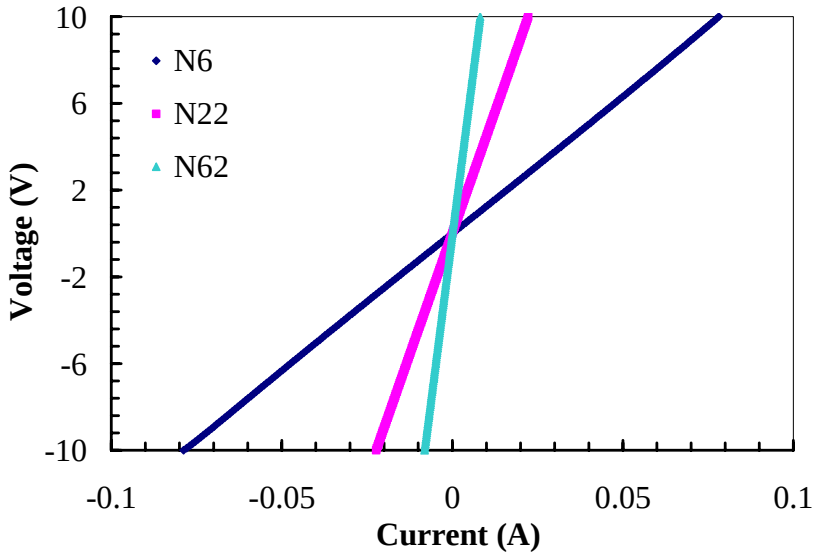

Figure 6-3: I-V characteristics for chains of 6, 22 and 62 ETWI.

This is comparable to the n-type ETWI (14 Ω (Chow et al. 2002)) and is satisfactory for use with our piezoresistive sensors, since the contribution to the overall resistance is less than 0.6 %. The theoretical minimum resistivity of boron-doped polysilicon is 2000 $\mu\Omega$-*cm* (Kamins 1990), which corresponds to 25 Ω for a 20 μm diameter, 400 μm long

conductor assuming uniform doping. However, an increase of 3 μm in the diameter can reduce the resistance to 12 Ω, which is consistent with our results.

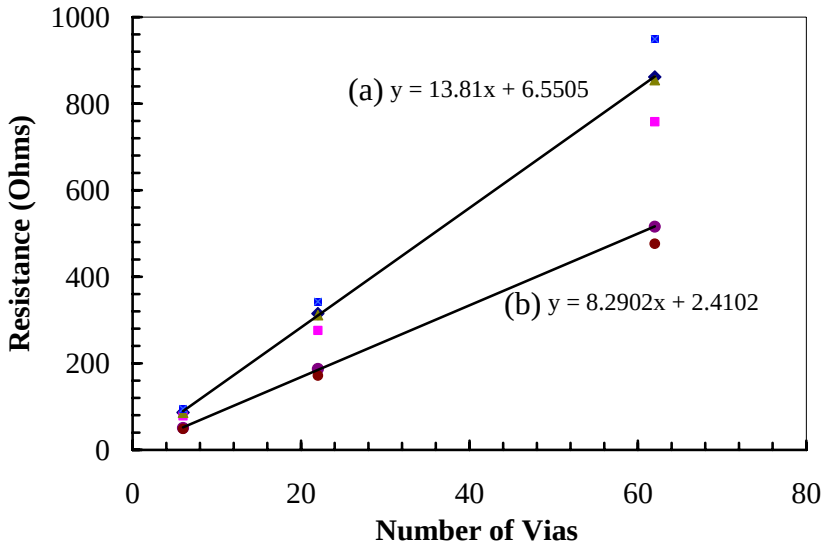

Figure 6-4: Plot illustrating the linear variation in the resistance of the ETWI with (a) 4 μm-thick and (b) 6 μm-thick doped polysilicon layers (slope indicates average ETWI resistance).

Although, the vias were designed to be 20 μm in diameter, several factors including mask erosion, overetch steps, simultaneous lateral etching can cause an increase in the diameter. In addition, doping crowding effects caused by oxidation can result in increased conduction.

Capacitance vs. Voltage Characteristics

The high frequency capacitance vs. voltage curve for varying bias voltage (-20 V to 20 V) between the substrate and the ETWI is shown in Figure 6-5. This curve is typical for an n-type substrate MOSC where an asymptotic maximum capacitance is observed at large positive voltages when the n-type substrate is in accumulation and a minimum capacitance is seen at negative voltages when the substrate is inverted. The measured capacitance is lower than the theoretical ETWI capacitance (Chow et al. 2002) due to the floating SOI substrate used in the ETWI process. In the SOI wafer used for the

fabrication of the acoustic transducer, the active silicon layer is separated from the bulk substrate by a thin (4000 *Å*) oxide layer. Thus requiring separate n^+ contacts for the active silicon layer and the bulk substrate. In the first generation design, a contact to the bulk substrate was not provided.

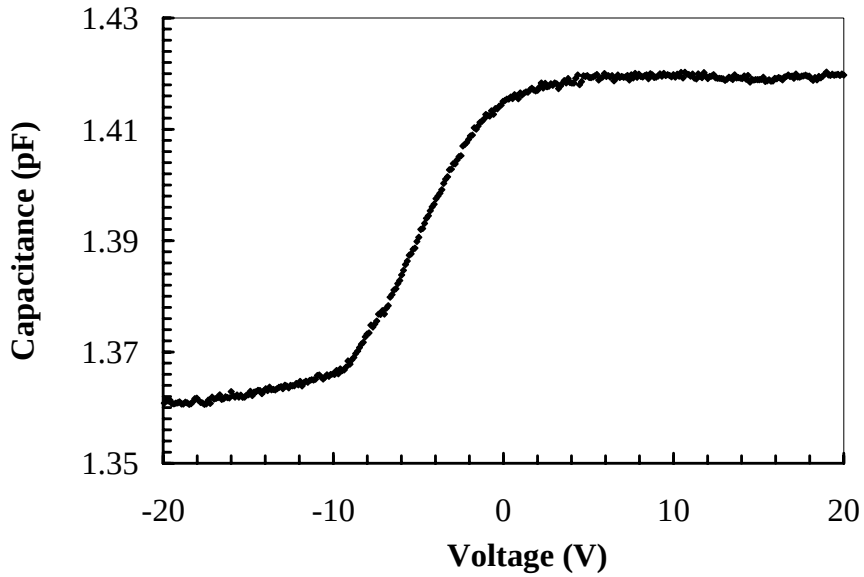

Figure 6-5: High-frequency (1 *MHz*) capacitance vs. voltage characteristics for a chain of 22 interconnects.

Noise Floor Spectra

The study of the electrical noise floor of a device is required to determine the minimum detectable signal (MDS). The voltage noise PSD of the sensor is plotted in Figure 6-6. As indicated**,** the voltage noise PSD is dominated by *1/f* noise at low frequencies. The MDS was calculated by taking the square root of the noise PSD and dividing by the sensitivity of the device to obtain pressure. Additional plots of the set-up noise from the amplifier and EMI and a sensor with front-side contacts are also shown for comparison. Since one application of the ETWI is to connect the sensor's small-signal output to nearby signal-conditioning electronics, the noise contributed by the interconnect itself must be minimal.

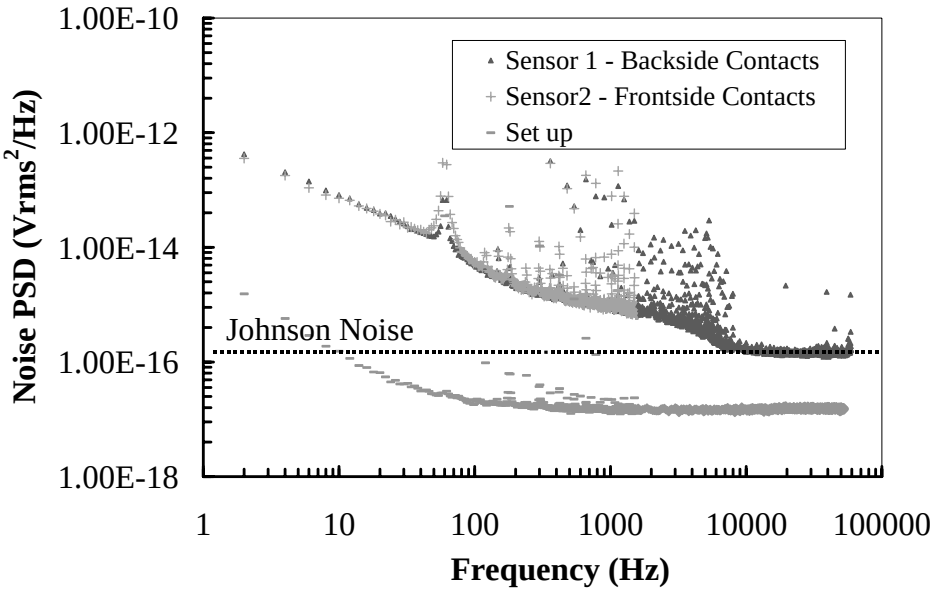

Figure 6-6: Noise power spectral density of the sensor at a bridge bias of 9 *V* (devices tested C1 and C3).

The results indicate a negligible noise contribution from the ETWI. The *1/f* noise intersects the thermal noise ($\approx 1.34\ mPa/\sqrt{Hz}$) at approximately 60 *kHz*, making the device only Johnson noise limited at the operating frequencies, with a MDS of 36.5 *dB* for a 1 *Hz* bin centered at 60 *kHz*. The "spikes" in the data are due to the deterministic interference at 60 *Hz* and 20 *kHz* and their harmonics.

Mechanical Characterization

Surface vibration measurements were performed on multiple devices using the scanning laser vibrometer. A visualization of the first three vibration modes of the thermoelastic resonator in response to a periodic chirp signal with a 3 *V* dc offset is shown in Figure 6-7. Figure 6-8 shows a plot of the vibration amplitude measured at the center of the diaphragm as a function of excitation frequency. In this case, the diaphragm was excited using a harmonic ac voltage (7 *V*) at varying frequencies superimposed on a dc voltage (7 *V*) to reduce frequency doubling of the output signal.

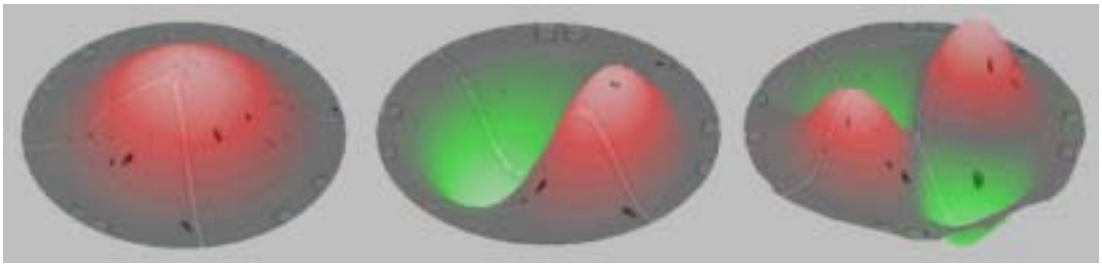

(0, 0) mode
Frequency: 58 *kHz*
Maximum amplitude: 50 *nm*

(1, 0) mode
Frequency: 108 *kHz*
Maximum amplitude: 100 *pm*

(2, 0) mode
Frequency: 186 *kHz*
Maximum amplitude: 7 *pm*

Figure 6-7: Visualization of the first three vibration modes of the thermoelastic resonator using the scanning laser vibrometer.

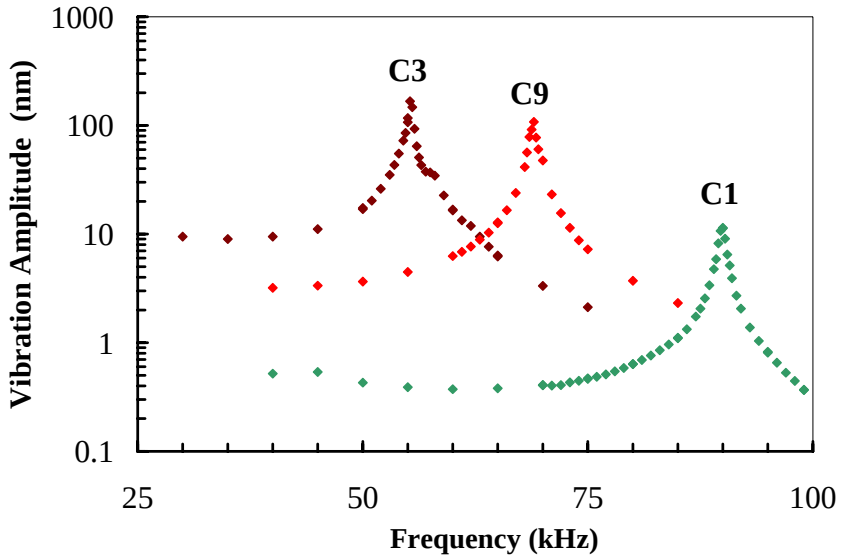

Figure 6-8: Plot of the vibration amplitude measured at the center of the diaphragm as a function of excitation frequency for varying thickness of the silicon layer.

As seen in Figure 6-8, the diaphragms exhibit a gain of more than 20 *dB* in the vibration amplitude at resonance. The measured vibration amplitude and quality (Q) factor of the resonators are tabulated in Table 6-3. The Q-factor of the resonator is defined as the ratio of the vibration energy to the energy dissipated per cycle (Stemme 1990). It can be calculated from the amplitude-frequency spectrum (Figure 6-8) by dividing the resonant frequency of the diaphragm by the frequency bandwidth at the 3 *dB* attenuation point (Stemme 1990)

$$Q = \frac{f_{res}}{\Delta f_{3dB}}. \qquad (6.1)$$

Table 6-3: Mechanical characteristics of the thermoelastic resonators.

Device label	Silicon thickness (μm)	Buckling height (μm)	Resonant frequency (kHz)	Amplitude at resonance (nm)	Quality factor
C1	10	0	90	11.3	60
C3	8	2	55	167	37
C9	5	8	69	108	34.5

Measurements made on transducers with varying silicon thickness indicate a relationship between the diaphragm thickness and the vibration characteristics (amplitude, resonant frequency and buckling height) as shown in Table 6-3. As the thickness is reduced from 10 μm to 8 μm, an increase in the vibration amplitude (15x) is observed. This is due to a net increase in the in-plane compressive load on the diaphragm. Since the compressive stress induced by the thermal oxide layer is fixed, a decrease in the silicon thickness proportionately increases the overall compressive load on the diaphragm and due to the slope $\partial w/\partial r$ of the deformed plate, the in-plane compressive load (N_o) produces an added bending effect. Consequently, an increase in the in-plane load increases its contribution to the overall bending effect. This is true for in-plane loads less than the critical buckling load ($N_o < N_{cr}$). According to linear buckling theory (Timoshenko and Krieger 1959 and Soderkvist and Lindberg 1994) the (static) transverse deflection due to in-plane compressive loads is zero in the pre-buckling state ($N_o < N_{cr}$) and unlimited with an unknown direction in the post-buckled state. It can be seen from Equation (4.42) that a value of the stiffness parameter, k corresponding to the first root of the Bessel function $\left(J_1(k) = 0\right)$ produces a singularity in the transverse deflection of the plate. The compressive load at which the singularity occurs is known as the critical buckling load

$$N_{cr} = 14.68 \frac{D^*}{a^2}. \qquad (6.2)$$

The critical buckling loads for various diaphragm thicknesses assuming clamped and simply supported boundary conditions are tabulated in Table 6-4. The boundary conditions represent limiting cases and in practice, the built-in edge of the diaphragm would have a finite rotational compliance.

Table 6-4: Critical buckling loads.

Device label	Silicon thickness (μm)	Critical buckling load (N/m) (simply supported edge)	Critical buckling load (N/m) (clamped edge)
C1	10	295.2	1031.8
C3	8	161.7	565.3
C9	5	48.3	168.9

In micromachined resonators, the fabrication-induced stress is usually constant, the value being fixed by the process parameters. In this case the compressive stress in the oxide layer is assumed to be 300 *MPa* which corresponds to a compressive load of 210 *N/m*. Therefore, the critical buckling load corresponds to a minimum thickness of the diaphragm below which it would buckle under the compressive load as shown in Figure 6-9.

However, this is based on the assumption of full symmetry and the omission of deflection-induced axial strain. In reality, factors such as the asymmetrical vibrating structure and transverse loading can cause significant transverse deflection before the critical buckling load as seen from the experimental data (Device C3).

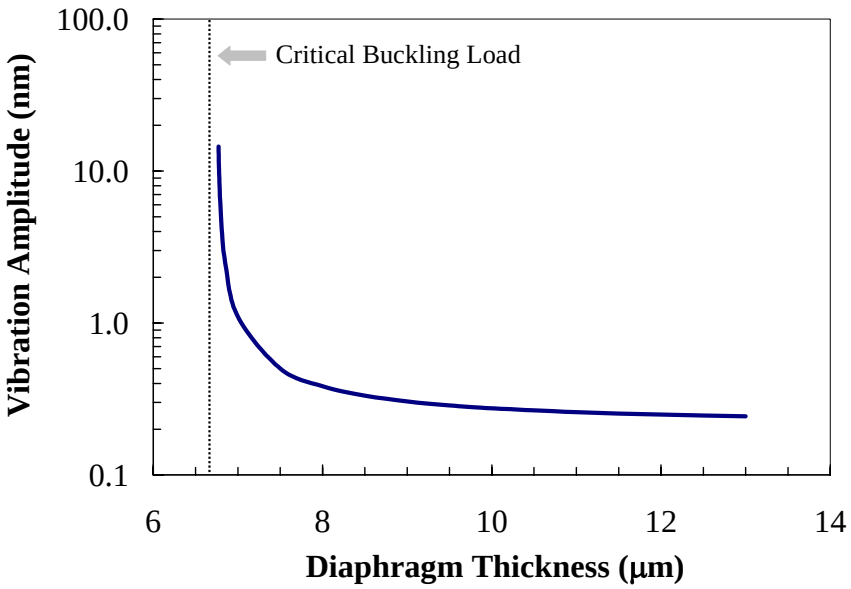

Figure 6-9: Vibration amplitude of a 1 *mm*-diameter diaphragm calculated at the center as function of the diaphragm thickness.

The buckling like transverse deflection, defined as quasibuckling, of compressively and transversely loaded structures has been investigated by Soderkvist and Lindberg (1994). According to Soderkvist and Lindberg (1994), the vibration amplitude is finite at the buckling load with a smooth transition to one of the stable post-buckling states. In the post-buckled state, the vibration amplitude is no longer a function of the diaphragm thickness but instead depends on the buckled height of the diaphragm (Hornung and Brand 1999). The vibration amplitude decreases with increasing buckling height (or in-plane load) of the strain-hardened diaphragm. This effect is illustrated in Figure 6-8 by the comparatively smaller vibration amplitude of the thinnest diaphragm (Device C9) with a buckled height of 8 μm.

It has been found that the resonant frequency reaches a minimum (Soderkvist and Lindberg 1994) and the vibration amplitude is at its maximum value for diaphragms with compressive loads close to the critical buckling load as shown in Figure 6-10 and Figure 6-11. In addition to the significant increase in the vibration amplitude, a lower resonant

frequency translates to longer wavelengths (3.8 *mm* at 90 *kHz*, 6.23 *mm* at 55 *kHz*), which would be beneficial for operating the sensors in the wavy interface.

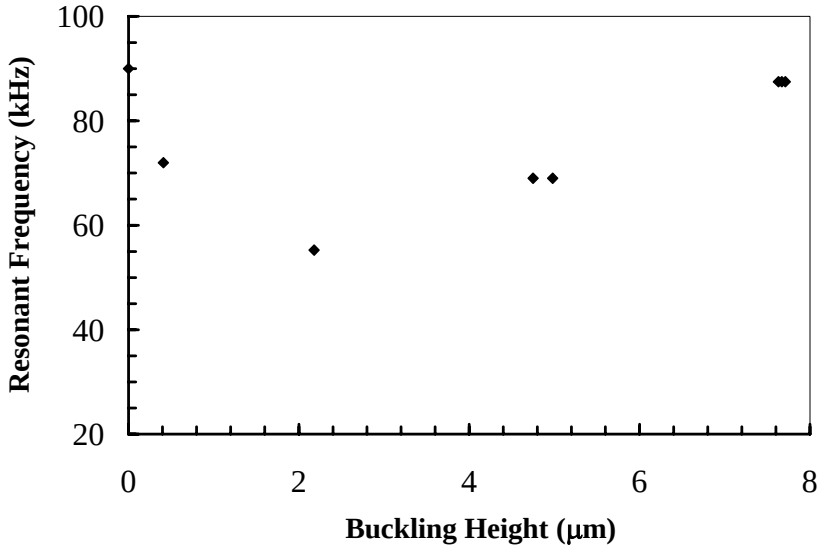

Figure 6-10: Resonant frequency of the thermoelastic resonators as a function of their buckled height measured at the center (data represents 7 devices).

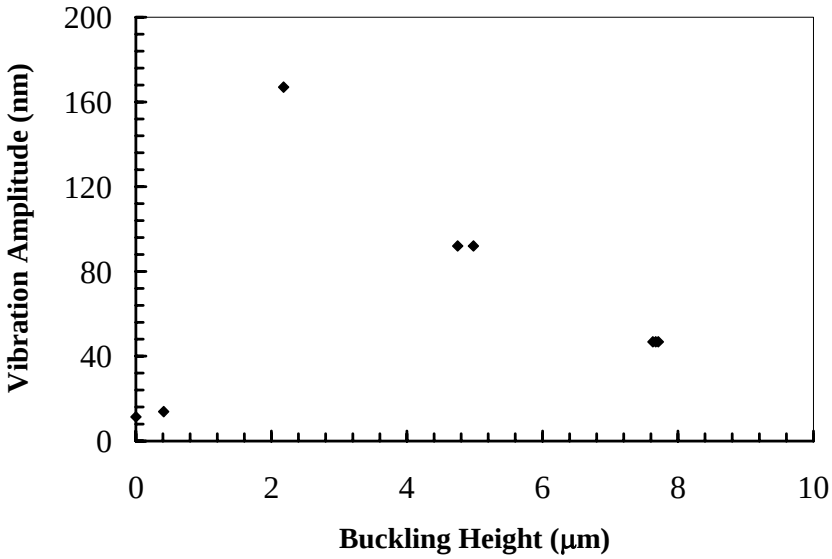

Figure 6-11: Vibration amplitude of the thermoelastic resonator as a function of the buckled height both measured at the center of the diaphragm (data represents 7 devices).

In addition to the fabrication-induced stress, the static component of the input power produces a static temperature distribution that introduces additional stresses in the diaphragm.

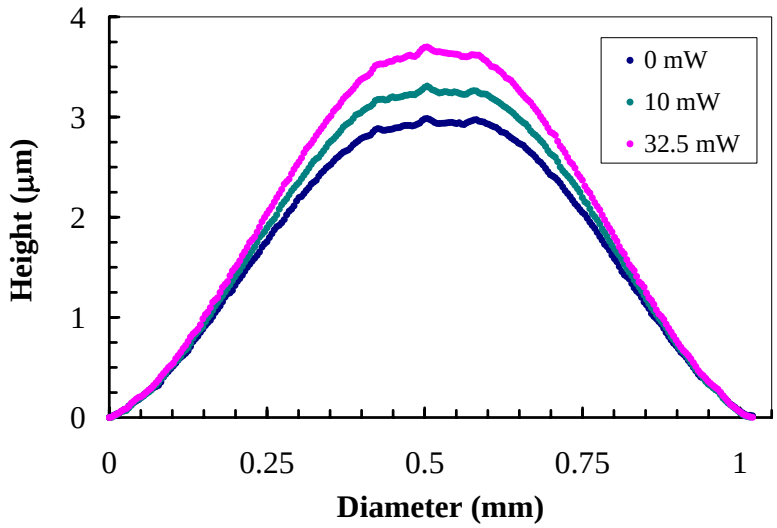

Figure 6-12: Deflection mode shape as a function of static power.

The additional stress induced by the static heating, observed from the increasing buckled height (Figure 6-12), affects the resonant frequency and vibration amplitude of the diaphragm. A plot of the change in the buckling height and resonant frequency caused by the change in the static power are shown in Figure 6-13 and Figure 6-14.

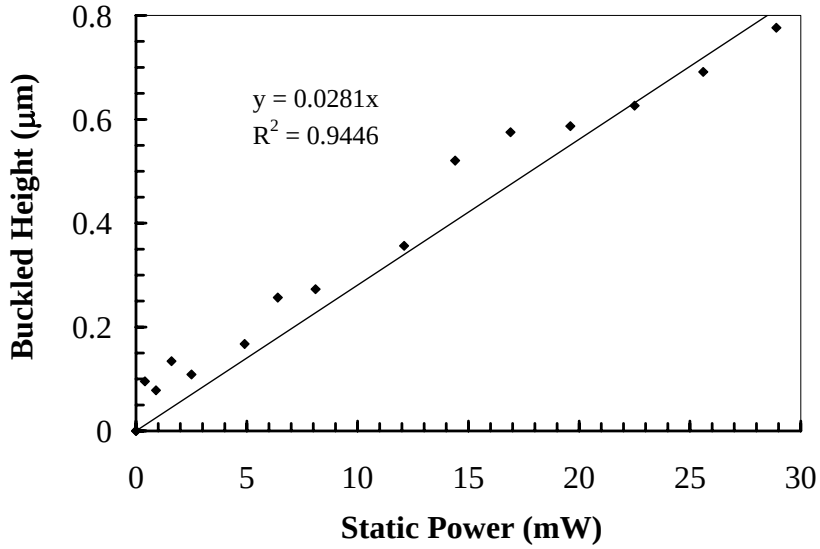

Figure 6-13: Change in the buckled height of the diaphragm as a function of static power.

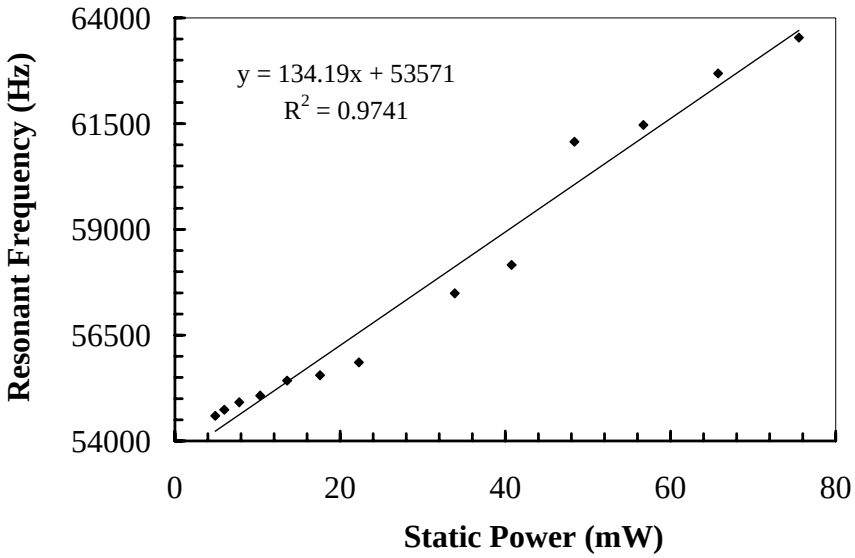

Figure 6-14: Resonant frequency of the diaphragm as a function of static power.

Acoustic Characterization-Receiver

The results of the acoustic characterization of the transducer used in a receiving mode are presented in the following section.

Linearity

The dynamic response of the sensor to varying sound pressure levels up to 140 *dB* (ref 20 μPa) obtained in the normal incidence plane wave tube is shown in Figure 6-15.

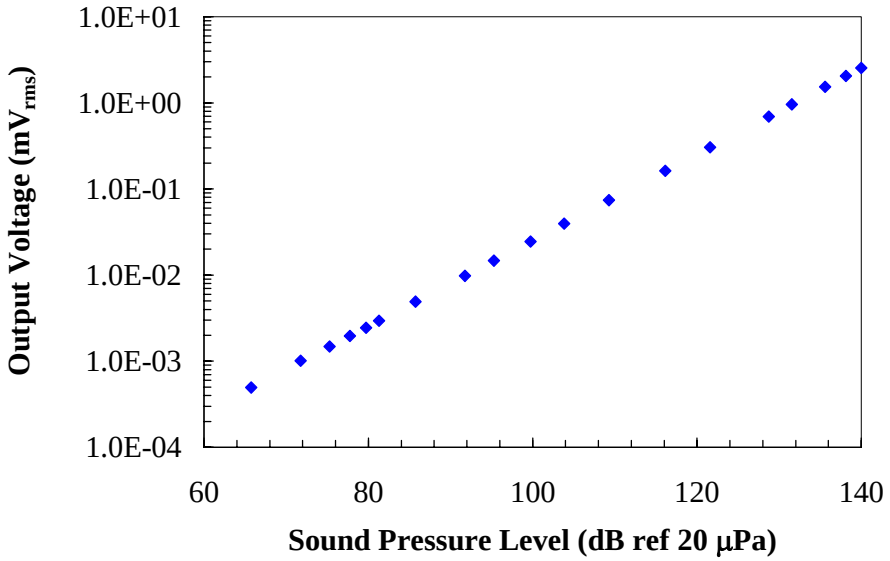

Figure 6-15: Plot illustrating the device linearity in sensing acoustic pressure perturbations (up to 140 *dB*) at a frequency of 1 *kHz* (Device C3).

The results indicate a linear response to acoustic pressure perturbations over four orders of magnitude (60-140 *dB*). The measured sensitivity at 1 *kHz* is 1.415 ± 0.0002 *μV/V.Pa*, or equivalently, -118.4 *dB* ± 1.4 *dB* ref 1 *V/V.Pa*.

Frequency Response

Figure 6-16 shows the magnitude frequency response of the sensor calibrated in the grazing incidence PWT and the normal incidence tube using a constant amplitude tone of 110 *dB*. The plot indicates a flat frequency response with an average sensitivity of 0.98 *μV/(V.Pa)* or equivalently –120.2 *dB* re 1 *V/(V.Pa*) with a standard deviation of 1 *dB* over measured frequency range (compared to a theoretical sensitivity of 1.28 *μV/V.Pa*). A flat frequency response is required for correlation and spectral analysis of the measured data.

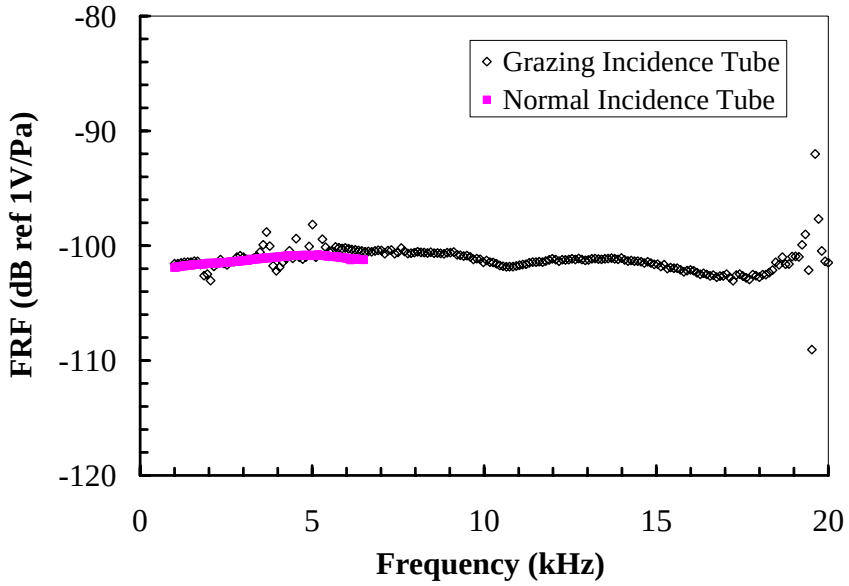

Figure 6-16: Magnitude of the sensor frequency response function to a constant sound pressure level of 110 *dB* (Device C3).

The results obtained from the grazing incidence PWT indicate data scatter at low frequencies. These variations may be attributed to the non-ideal propagation characteristics of the tube, including a compliant boundary condition and an area change at the tube termination. The same frequency range (1-6 *kHz*) tested in the normal

incidence tube indicates a flat sensor response. The scatter observed near 20 *kHz* is due to the propagation of higher order modes.

Acoustic Characterization-Transmitter

The directional characteristic of the generated acoustic field is shown in Figure 6-17. The plot indicates a drop in sound pressure level with increasing angle from the diaphragm axis. At an angle of 90^o the sound pressure level is reduced to 40% of the maximum on-axis value. Theoretically, a sensor with Helmholtz number $ka<1$ should exhibit omni-directional radiation pattern as explained in Chapter 4. However, this holds for a radiator mounted on an infinite baffle. The observed focusing of the sound field may be attributed to the packaging of the transducer, which is recessed in a square depression of 0.5 *mm*. A detailed schematic of the transducer package is provided in Appendix D.

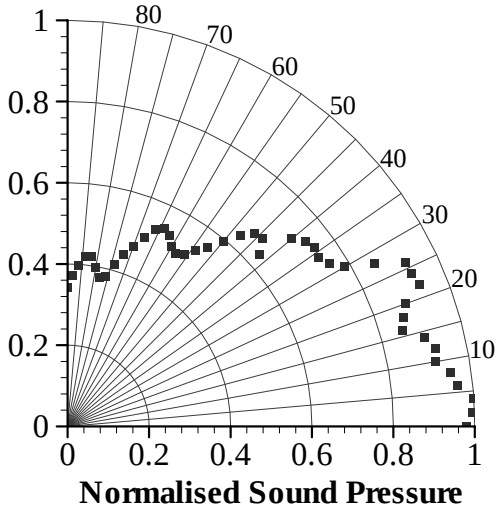

Figure 6-17: Directivity of the generated acoustic field at a frequency of 60 *kHz* (Device C3) ($ka = 0.55$).

Sound pressure measurements versus distance from the diaphragm surface are plotted in Figure 6-18. A transmitter source level of 50 *dB* (ref 20 μPa) at an operating

frequency of 60 *kHz* was obtained by extrapolating the graph to 1 *m*. The plot also shows the characteristic inverse relation between sound pressure level and distance.

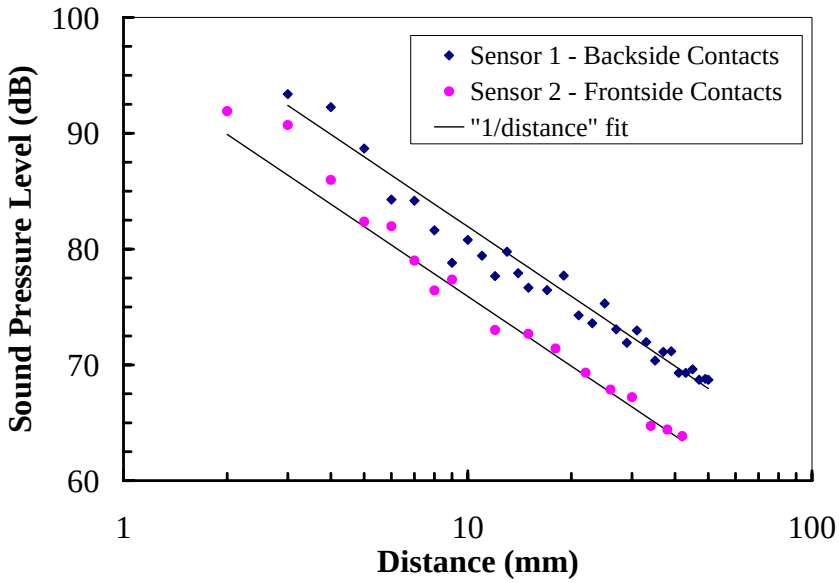

Figure 6-18: Sound pressure level of generated acoustic field as a function of radial distance, at a frequency of 60 *kHz* (Device C3 and C9).

The far-field for the transducer operating at 60 *kHz* is established at a distance of 0.15 *mm*, known as the Rayleigh distance (Blackstock 2000)

$$R_o = \frac{ka^2}{2}. \qquad (6.3)$$

The oscillations in the data are due to scattering from the microphone surface that results in the formation of a standing wave between the transmitter and the microphone. The scattering effect is reduced with increasing distance from the transmitter.

Table 6-5 compares the physical dimensions and operational characteristics of the micromachined acoustic resonator with that of a conventional ultrasonic transducer. The performance of the commercial transducer is superior in terms of transmitting and receiving sensitivities, however, it should be noted that the design of the micromachined transducer is not optimized. The main goal of the first-generation acoustic proximity

sensor was prove the manufacturing feasibility of a transducer integrated with electrical through-wafer interconnects.

Table 6-5: Comparison of the MEMS-based acoustic transducer with a conventional ultrasonic transducer.

	MEMS-Based transducer (Device C3)	Conventional transducer (Massa E-152)
Dimensions	1 *mm*-diameter, 9 μm-thick (resonator) 5 *mm* x 5 *mm* (chip size)	11.1 *mm*-diameter, 10.1 *mm*-thick (packaged transducer)
Resonant frequency	55 *kHz*	73 *kHz*
Bandwidth (untuned)	1 *kHz*	1 *kHz*
Transmitting sensitivity (untuned) (ref: 20 μPa at 0.305 *m*)	55 *dB* (at 60 *kHz*)	88 *dB* (at 73 *kHz*)
Receiving sensitivity (untuned) (ref: 1 *V/Pa*)	-101 *dB* (off resonance)*	-42 *dB* (at resonance)
Total beam angle	110 deg	60 deg
Power	40 *mW*	10 *mW*

* Predicted sensitivity at resonance $\approx$-81 *dB*.

Proximity Sensing

Figure 6-19 compares the true distance of a sound-hard boundary with that obtained using the continuous-wave (CW) phase-shift technique.

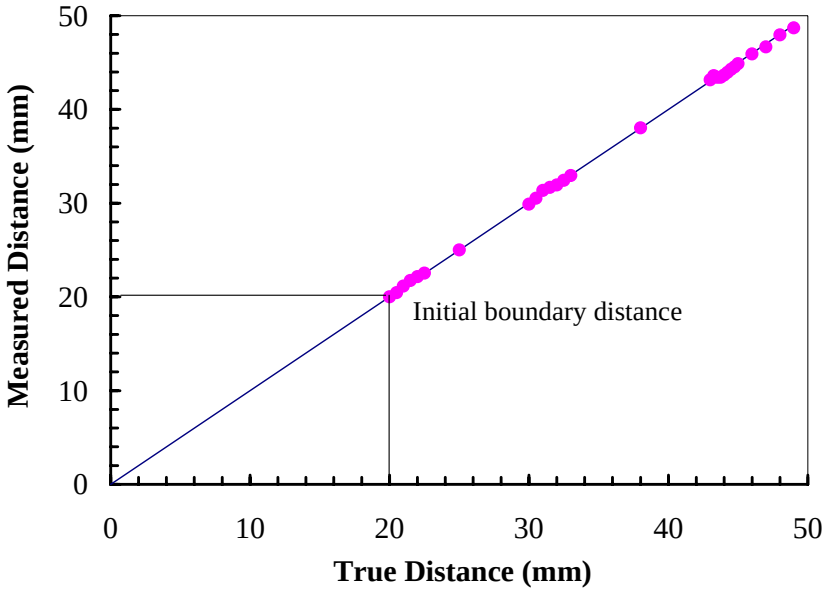

Figure 6-19: Plot of the true distance versus the measured distance obtained using a CW phase-shift technique.

The measured phase of the acoustic wave can be related to the time-delay τ by

$$\phi = 2\pi f \tau, \qquad (6.4)$$

where f is the operating frequency. The time delay together with the knowledge of the acoustic velocity in the medium is used to calculate the distance to the boundary. This experiment, however, is only a proof-of-concept demonstration of proximity sensing using the acoustic transducers and the actual performance of the system would depend to a large extent on the algorithm used (Barshan 2000, Li et al. 2002).

CHAPTER 7
CONCLUSIONS AND FUTURE WORK

This chapter summarizes the work presented in this thesis. A first-generation acoustic proximity sensor utilizing thermoelastic actuation and piezoresistive detection with integrated electrical through-wafer electrical interconnects has been developed. Concluding remarks are presented and potential paths for future work are discussed.

Conclusions

A thermoelastically actuated acoustic proximity sensor with integrated polysilicon-based electrical through-wafer interconnects has been developed. The rigorous theoretical modeling, fabrication and preliminary characterization of the device were presented. The analytical model for the thermoelastic actuation of the composite diaphragm incorporates for the first time several key aspects relevant to micromachined thermal actuators that have not been considered in previously reported models. Specifically the composite structure of the actuator has been considered in both the thermal and the mechanical analysis, the diffused heater has been more accurately represented with an internal heat source and finally the effects of in-plane heat conduction and fabrication-induced stresses on the vibration characteristics of the diaphragm have been included in the analysis. Comparison of the model with a coupled thermal-mechanical finite element simulation shows excellent agreement with significantly faster computation time for the analytical model. The analytical model developed here can be easily incorporated into optimization tools in Matlab thus enabling

faster design optimization. The structure of the analytical model is modular and can be easily adapted to include second order effects such as convective boundary conditions, compliance of the plate boundary and the effects of radiation without significantly altering the analysis procedure. The main goal of the theoretical analysis, however, was to provide a tool that quickly identifies to the first-order the optimum operating point of the resonator given the large number of design parameters. It has been observed from experimental data that maximum sound pressure level of the radiated acoustic field is obtained for resonators with in-plane compressive load very close to the buckling load and the analytical modeling of the vibration of a buckled diaphragm may be mathematically very intensive. If the analytical model provides an estimate of the optimum design parameters, it can be further refined using numerical techniques and incorporating more realistic sensor operating conditions. For instance, the analytical model can be used to identify the buckling load for a given set of design parameter. Next using finite element techniques the vibration characteristics of the diaphragm at the buckling load can be calculated while also relaxing the simplifying assumptions of the analytical model. The combination of analytical and numerical techniques may be more optimal than pursuing only one technique entirely.

Preliminary electrical, mechanical and acoustic characterization of the device indicate a transmitter source level of 50 *dB* (ref 20 μPa) at an operating frequency of 60 *kHz*, a receiving sensitivity of 0.98 $\mu V/(V\ Pa)$, a flat frequency response over the measured range of 1-20 *kHz*, a linear response from 60-140 *dB*, negligible leakage current for the junction-isolated diffused piezoresistors (< 14 *pA* at -10 *V*), low

interconnect resistance of 14 Ω, and a minimum detectable signal of 36.5 *dB* for a 1 *Hz* bin centered at 60 *kHz*, at a bias of 9 *V*.

While the first-generation acoustic transducer is not optimized in terms of performance and does not yet reach the specifications of a commercial ultrasound transducer, the manufacturing feasibility of the MEMS-based transducer with integrated electrical through-wafer interconnects has been demonstrated. The advantages of the MEMS-based transducer in terms of performance and device packaging can be compared to commercial transducers after the development of an optimized second-generation transducer.

Future Work

Future work in the area of device modeling could involve improving the analytical model by incorporating more realistic compliant boundary conditions, effects of damping and geometric non-linearities in the strain-displacement relationship. The physical validity of the model can then be accessed by comparing with direct measurements of the diaphragm vibration obtained using a laser vibrometer. However, a direct comparison of the model with experimental data will require more detailed and precise measurements of the transducer geometry and in-plane stresses. Finally, the model could be coupled with formal optimization tools to maximize the sound radiation efficiency of the resonator.

The fabrication of the ETWI presented here is a preliminary investigation into p-type ETWI for MEMS sensors/actuators. Accurate C-V characteristics and the ETWI noise floor could not be extracted due to the lack of a proper contact to the bulk silicon substrate in the SOI wafer process. Future work should focus on fabrication process modifications to better suit a SOI wafer. *In-situ* doped polysilicon deposition techniques

could be explored for both the n-type (using a silane:phosphine:nitrogen mixture) and p-type (using a mixture of silane and boron- trichloride) ETWI and compared to the existing method in terms of ETWI characteristics as well as deposition rates. Planarity is a critical issue for integration of the pre-process ETWI with an accompanying MEMS sensor/actuator. Techniques such as chemical mechanical polishing could be investigated towards this end.

For performance enhancement in a proximity-sensing scheme, directional acoustic sources could be investigated by increasing the size of the diaphragm relative to the generated acoustic wavelength. This can potentially reduce cross-talk between the transducers enabling faster algorithms. Separate transmitters and receivers should be considered instead of an integrated transducer since the optimum diaphragm design for the generation of acoustic waves and its detection are significantly different. There is a significant level of capacitive coupling (on the order of the acoustic signal) between the transducers (transmitter and receiver) that needs to the addressed through better packaging and by modifying the transducer fabrication process to include a top-side metal layer to shield the electromagnetic signal.

APPENDIX A
PROCESS TRAVELER

The process flow for the fabrication of the integrated acoustic proximity sensor and ETWI is presented.

Wafer: 4" n-type (100) SOI, 4000 *Å*-thick buried oxide layer, 12 μm-thick silicon overlayer, 3-5 *ohm-cm*.

Masks:

- Labels - **LM**
- Bond pads - **BPM**
- Holes - **HM**
- Piezoresistors - **PRM**
- Heater - **HTM**
- Contact openings through oxide front surface – **C1M**
- Contact openings through oxide back surface – **C2M**
- Metal front surface **– MIM**
- Metal back surface **– M2M**
- Contact through nitride- **PM**
- DRIE - **DRM**
- Scribe lines - **SM**
- Signal mask **- SGM**
- Substrate contact - **SCM**

Process Steps

Start with SOI wafer (n-Si CZ <100> 3-5 Ω-*cm*) with 13 μm silicon on 4000 *Å* BOX.

Scribe and etch

a. Scribe wafers.

b. DI rinse.

c. Measure wafer thickness.

1. Pattern and etch holes for bond pads and through wafer vias

d. Pre-oxidation clean.

e. Grow 1000 *Å* of dry SiO_2 at 1100 ^oC on both sides of the wafer.

f. Coat and pattern resist/oxide on scribe side (BPM). This step puts alignment marks in the oxide.

Singe - 150 ^oC for 15 *min*
Coat HMDS - 2000 rpm for 30 *sec*
Coat resist (1μm, SPR3612) - spin at 5700 rpm for 45 *sec*
Evalign using BPM for 2 *sec*, hard contact
Develop
Bake - 110 ^oC for 60 *min*
Descum (Drytek) - 30 *sec* to clear holes
BHF (6:1) - 90 *sec* of standard oxide etch (etch rate 900 *Å/min*)
Piranha - 20 *min*, dump rinse, spin dry (resist strip)

g. Coat and pattern resist/oxide on non-scribed side (BPM). This step puts alignment marks in the oxide.

h. Coat and pattern resist through hole mask on both sides (HM). Align with alignment marks of step 2c-2d.

Singe - 150 ^oC for 5 *min*
Coat 10 μm on scribe side
HMDS on both sides
Coat resist (SPR220) at 1700 *rpm* for 70 *sec* and 5000 *rpm* for 1 *sec* edge bead removal
Bake on hotplate - 120 *sec*
Coat 10 μm on non-scribe side
Softbake - 110 ^oC oven for 90 *min*
Let wafers sit in air for 10+ *hrs*

Expose with Hole mask on scribe side (HM)
EValign in vacuum contact mode and expose for 30 *sec*
Expose with Hole mask on non-scribe side (HM)
Develop both sides
LDD26W by hand ~ 3-5 *min*
Note: Don't do post bake, as it tends to crack the resist (either immediately or in the STS etcher)

2. Etch Through-Wafer Vias (TWV) using deep reactive ion etch (DRIE)

a. Etch alignment marks.

STS etch - 2 *min* on scribed side and 2 *min* on non-scribed side

b. Etch from scribe side up to the BOX – tape over major resist blemishes.

c. Etch oxide using buffered HF (or Plasma).

d. Etch from non-scribe side halfway - tape over resist blemishes.

STS etch for ~210 *min*

e. Continue with step (b) - finish TWV

STS etch for ~210 *min* and 30 *min* timed overetch with support wafer

f. Ash strip resist.

3. Clean etch polymer

Acetone, isopropanol and blow dry
5 *min* oxygen plasma
20 *min* piranha
5 *min* oxygen plasma

4. Deposit thin films

a. Deposit LPCVD Oxide isolation layer

Oxidation diffusion clean - sulfuric/peroxide, HF, HCL/peroxide
Deposit 2 μm oxide (wet) at 1150 ^{o}C for 8 *hrs*

b. Deposit LPCVD polysilicon ground conduction layer

LPCVD diffusion clean
Deposit 2 μm polysilicon - 2 *hrs* and 45 *min*
Inspect - make sure light passes through all holes

c. Dope polysilicon with Boron

LPCVD diffusion clean
Boron dope poly

d. Clean borosilicate glass formed over the polysilicon and diffusion clean.

e. Repeat polysilicon deposition and doping (4b - 4d).

5. Fill TWV holes

a. Deposit 3 μm of polysilicon.

b. Dope surface polysilicon with boron

LPCVD diffusion clean
Boron dope polysilicon
Clean Borosilicate glass formed over the polysilicon and diffusion clean

c. Drive in boron

LPCVD diffusion clean

Anneal at 1000 ^{o}C for 1 *hr*

6. Pattern polysilicon bond pads

a. Coat both sides with 10 μm resist.

b. Expose scribed side with SGM mask (Clear field).

c. Expose non-scribed side with SGM mask (Clear field).

d. Develop.

e. Plasma etch polysilicon from the top surface, stopping on the oxide.

f. Etch polysilicon from the backside, stopping on the oxide.

Note: Repeat (e) and (f) in steps of 1-2 μm, to prevent wafer bow.

g. Strip resist

Acetone, isopropanol and blow dry
20 *min* piranha, dump rinse and spin dry

h. Etch pads to a height of 1-2 μm or if possible make it planar with the oxide (use profile-meter to measure height).

7. Pattern and diffuse heater

Spin photoresist on front surface and pattern heater mask. Alignment marks make sure that the heater resistor is aligned to the center of the diaphragm. This mask also creates alignment marks for the next layer.

a. Coat and pattern heater mask on scribe side (HTM) using SPR220.

b. Etch Oxide.

c. Heater implantation

Ion implant - dopant: boron, energy: 170 *keV*, dose: 1e13 cm^{-2}
7 degree tilt, blanket front surface using photoresist as a screen.
This forms the p^{++} heater of the resonator.

d. Ash photoresist.

e. Anneal at 1100 ^{o}C for 130 *min* in inert ambient.

8. Pattern and diffuse piezoresistors

Spin photoresist on front surface and pattern piezoresistors mask. Alignment marks make sure that the piezoresistors are aligned to the edge of the diaphragm. This mask also creates alignment marks for the next layer.

a. Coat and pattern Piezoresistor mask on scribe side using SPR 220.

b. Etch Oxide.

c. Piezoresistor implantation

Ion implant – dopant: boron, energy: 85 *keV*, dose: 8E13 cm^{-2}

d. Ash photoresist.

9. Oxide growth

Pre-oxidation clean - top and bottom surfaces.
Grow 7000 *Å* of high-quality passivation oxide (dry-wet-dry)

Temp = 950 ^{o}C, time=100 *min*
Temp = 950 ^{o}C, time=245 *min*
Temp = 950 ^{o}C, time=100 *min*

10. Substrate contact

a. Spin photoresist on front surface and pattern substrate contact (SCM) mask.

b. Etch Oxide.

c. Ion implant- dopant: phosphorus, energy: 85 *keV*, dose: 8E13 cm^{-2}.

d. Ash strip resist.

e. Anneal at 900 ^{o}C for 15 *min* in inert ambient.

11. Pattern front and back contact cuts

a. Spin photoresist on front and back surfaces and pattern contact cut masks (CIM & C2M).

b. De-scum using oxygen plasma - Note: contact holes PR, 1 *min* to insure clearing.

c. Etch oxide.

d. Ash photoresist.

12. Metallization

a. Pre-metal piranha clean. Very short HF dip, do not remove more than *50 Å*.

b. Sputter 1.4 μm Al (1% - Si) to avoid high contact resistance due to "spiking".

c. Coat both sides with 10 μm resist.

d. Softbake 110 ^{o}C oven for 90 *min*.

e. Let wafers sit in air for 10+ *hrs*.

f. Expose scribed side with M1M.

g. Expose non-scribed side with M2M.

h. Develop both sides.

i. Etch Aluminum both sides

PAN etch - Plasma based metal etch

j. Clean up Al/Si etch - freckle etch for a few minutes (to remove silicon precipitates).

k. Strip resist

Acetone, isopropanol and blow dry
O_2 asher

l. Forming gas anneal.

13. Nitride Passivation

Deposit PECVD nitride 3300 $\AA$ on the top surface.

14. Pattern nitride contacts

a. Spin photoresist on front surface and pattern contact cut mask (PM).

b. Etch nitride - dry etch.

c. Ash photoresist.

15. DRIE for membrane release (will include cleave lines)

Spin photoresist on both surfaces and pattern back surface for DRIE (DRM). This produces the thin silicon diaphragm of the proximity sensor.

a. Coat and pattern diaphragm mask on non-scribe side (DRM) using SPR 220.

b. Plasma etch silicon (~400 μm) up to the BOX. The buried oxide serves as the etch stop for the DRIE.

c. Etch oxide (6:1 BOE).

d. Ash photoresist.

APPENDIX B
PIEZORESISTOR DESIGN

FLOOPS® Input Files

The FLOOPS® input files used for simulating the process of ion implantation and anneal are included here.

(A) Heater

This program simulates the final (boron) doping profile in the silicon layer after ion implantation, activation anneal and the growth of a thermal oxide layer

```
*****************************************************
line x loc=-0.005 tag=oxi spacing=0.01
line x loc=0 tag=top spacing=0.01
line x loc=3 spacing=0.01 tag=bot1
line x loc=3.1 spacing=0.01 tag=bot2
region oxide xlo=oxi xhi=top
region silicon xlo=top xhi=bot1
region silicon xlo=bot1 xhi=bot2

init
strip oxide
implant boron dose=1e13 energy=170
sel z=log10(Boron+1)
plot.1d
diffuse temp=1100 time=130
diffuse temp = 950 dry  time = 100.0
diffuse temp = 950 wet time = 245.0
diffuse temp = 950 dry time = 100.0
sel z=log10(Boron+1)
plot.1d bound !cle

set cout [open resdata2 w]
puts $cout [print.1d]
close $cout
sel z=log10(8.79e14)
plot.1d !cle
*****************************************************
```

(B) Piezoresistors

This program simulates the final (boron) doping profile in the silicon layer after ion implantation, activation anneal and the growth of a thermal oxide layer

```
**********************************************************
line x loc=-0.005 tag=oxi spacing=0.01
line x loc=0 tag=top spacing=0.01
line x loc=3 spacing=0.01 tag=bot1
line x loc=3.1 spacing=0.01 tag=bot2

region oxide xlo=oxi xhi=top
region silicon xlo=top xhi=bot1
region silicon xlo=bot1 xhi=bot2

init
strip oxide
implant boron dose=8e13 energy=85

sel z=log10(Boron+1)
plot.1d bound !cle
diffuse temp=900 time=15
diffuse temp = 950 dry  time = 100.0
diffuse temp = 950 wet time = 245.0
diffuse temp = 950 dry time = 100.0
sel z=log10(Boron+1)
plot.1d bound !cle

set cout [open prdata w]
puts $cout [print.1d]
close $cout
sel z=log10(8.79e14)
plot.1d !cle
**********************************************************
```

Resistance Calculation

This section provides details of the discretization technique used to calculate the resistance of an arc-shaped piezoresistor under zero load condition.

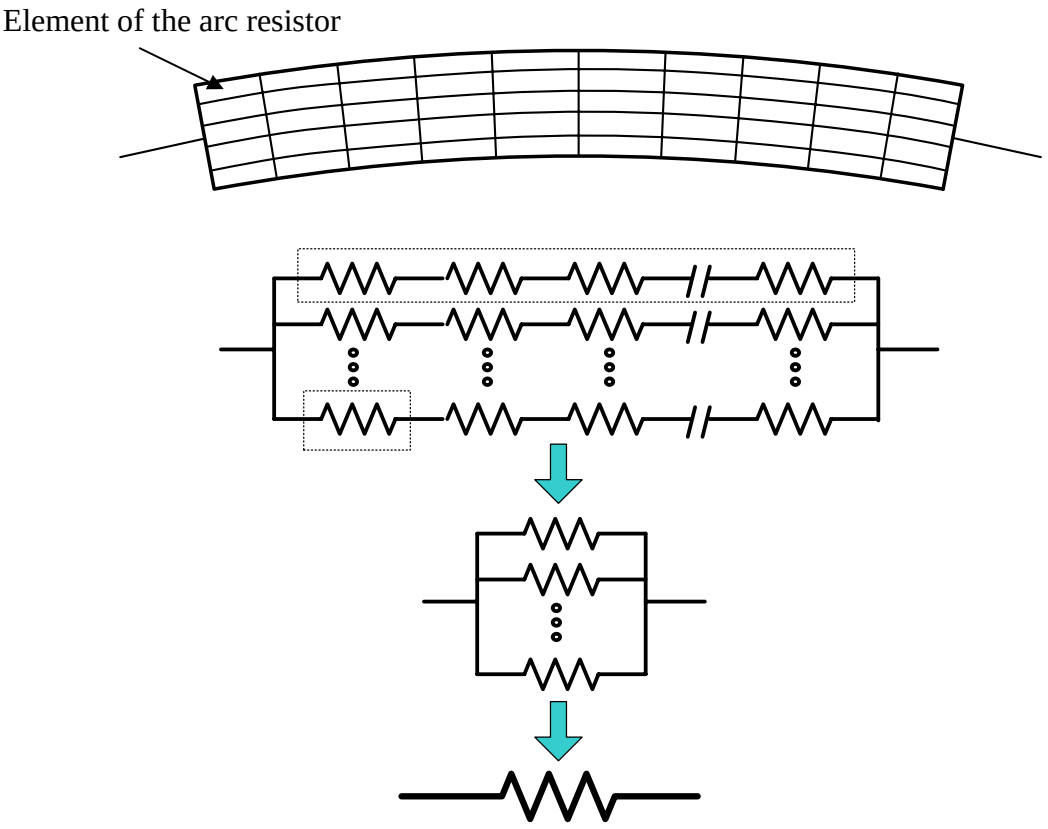

Figure B-1: A schematic of the discretized arc piezoresistor and the equivalent resistor model illustrating the series connection of the elements in the circumferential direction and the parallel connection of the segments in the radial direction.

The resistor is discretized into infinitesimal elements (Figure B-1) of length, $dl = r d\theta$ and area, $dA = t dr$, where r is the radius of the center point of the element and t is the thickness of the resistor. The resistance of an individual element is given by

$$R_{element} = \rho \frac{r d\theta}{t dr}, \qquad \text{(B.1)}$$

where ρ is the resistivity. For a given arc angle, $d\theta$ the resistors are in parallel in the radial direction and in series in the circumferential direction as shown in Figure B-1. The

total resistance of the elements in series can be obtained by adding the resistances of the individual elements, which in the limiting case is replaced by an integral

$$R_{segment} = \int_0^{\theta} \rho \frac{r d\theta}{t dr} = \rho \frac{r\theta}{t dr}. \qquad \text{(B.2)}$$

The total resistance of the piezoresistor is then obtained by adding (integrating) the segments in parallel

$$\frac{1}{R_{arc}} = \int_{r_a}^{r_b} \frac{t dr}{\rho \theta r}, \qquad \text{(B.3)}$$

that results in

$$R_{arc} = \frac{\rho}{t} \frac{\theta}{\ln(r_b / r_a)}, \qquad \text{(B.4)}$$

where r_a and r_b represent the inner and outer radius of the resistor and θ is the arc angle.

A similar procedure is adopted for the tapered resistor

$$R_{taper} = \frac{\rho}{t} \frac{\ln(r_b / r_a)}{\theta}. \qquad \text{(B.5)}$$

The resistance modulation of the individual elements is obtained by substituting the values of π, σ and R in the following equations

$$\frac{\Delta R}{R_{taper}} = \sigma_r(r)\pi_l(\theta) + \sigma_t(r)\pi_t(\theta) \qquad \text{(B.6)}$$

and

$$\frac{\Delta R}{R_{arc}} = \sigma_t(r)\pi_l(\theta) + \sigma_r(r)\pi_t(\theta). \qquad \text{(B.7)}$$

After calculating the resistance modulation of an individual element the procedure described above is used to calculate the total resistance modulation of the piezoresistor. An iterative process is used to arrive at the optimum arc and tapered piezoresistor sizes (Figure B-2) that have equal mean resistance values and equal but opposite sign modulations.

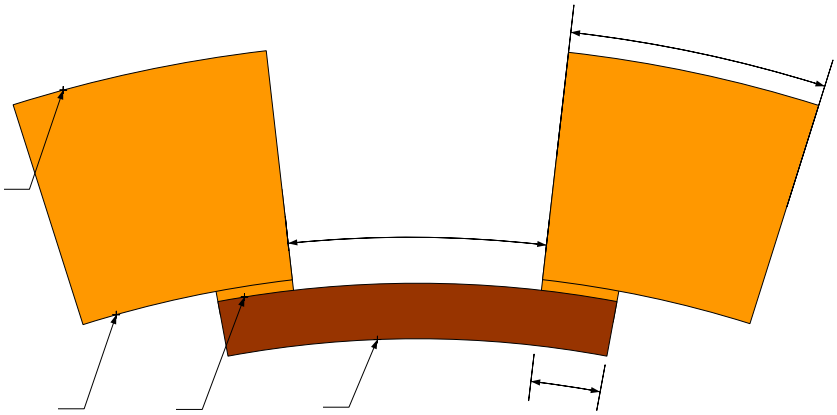

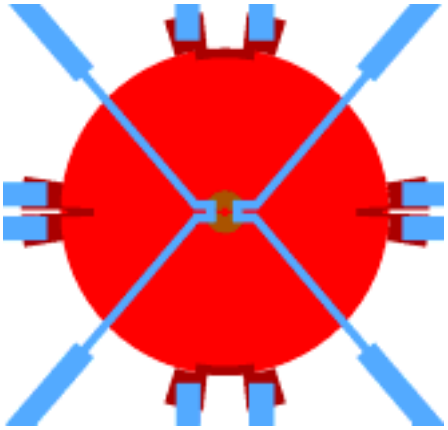

R 614

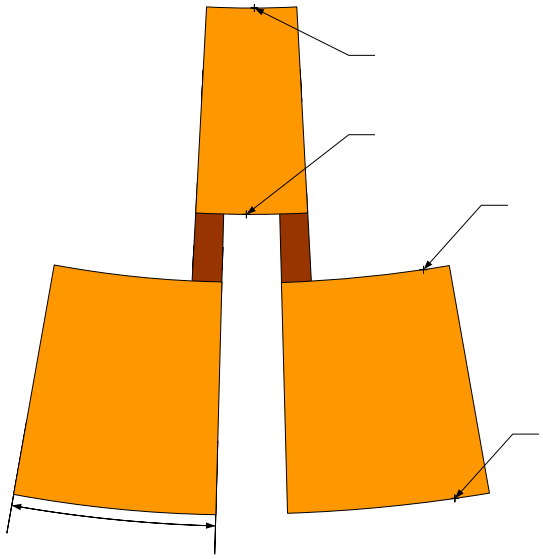

Figure B-2: Piezoresistor geometry and layout (all dimensions are in *mm*).

R 504

APPENDIX C
THERMAL ACTUATION OF A COMPOSITE DIAPHRAGM

In the following sections, the 2-D temperature distribution in the composite diaphragm is calculated using the Fourier heat conduction model, which is then used to derive the thermoelastic forcing functions. The plate governing equations are then formulated using the equations of motion and the linear thermoelastic constitutive relations.

Heat Conduction Model

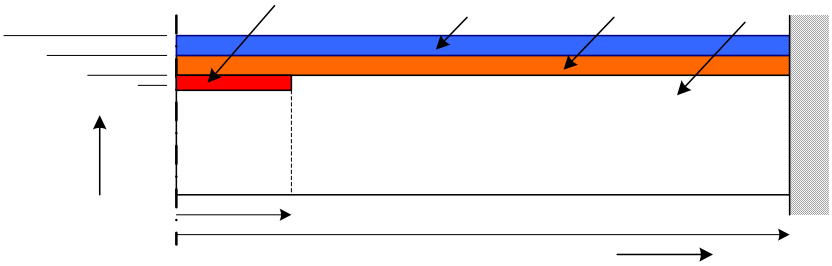

Figure C-1: Axisymmetric model of the composite diaphragm consisting of three transversely isotropic layers and a diffused resistive heater (H_1, H_2, H_3 and H_{Heat} represent distances from the reference plane).

The governing equation for heat conduction in the individual layers of a 3-layered composite diaphragm (Figure C-1) based on Fourier's law is given by (Ozisik 1993)

$$\alpha_1\left(\nabla^2 T_1 + \frac{1}{k_1} g_1(r,z,t)\right) = \frac{\partial T_1}{\partial t}; \quad 0 < z < H_1, \tag{C.1}$$

$$\alpha_2 \nabla^2 T_2 = \frac{\partial T_2}{\partial t}; \quad H_1 < z < H_2, \tag{C.2}$$

and $$\alpha_3 \nabla^2 T_3 = \frac{\partial T_3}{\partial t}; \quad H_2 < z < H_3, \tag{C.3}$$

where α and k represent the thermal diffusivity and the thermal conductivity of the individual layers, $g_1(r,z,t)$ represents an internal heat source within layer 1

$$g_1(r,z,t) = g_o \int_0^b \delta(r)\, dr \int_{H_{Heat}}^{H_1} \delta(z)\, dz \, \cos(\omega t), \tag{C.4}$$

and ∇^2 is the axisymmetric Laplacian operator in cylindrical coordinates,

$$\nabla^2 = \frac{1}{r}\frac{\partial}{\partial r}\left(r\frac{\partial}{\partial r}\right) + \frac{\partial^2}{\partial z^2}. \tag{C.5}$$

The diaphragm is assumed to be thermally insulated on the top and bottom surfaces,

$$\left.\frac{\partial T_1}{\partial z}\right|_{z=0} = 0 \text{ and } \left.\frac{\partial T_3}{\partial z}\right|_{z=H_3} = 0. \tag{C.6}$$

Additionally, the heat conduction in the diaphragm is assumed to be symmetric about the center, and the edge is maintained at ambient temperature,

$$\left.\frac{\partial T_i}{\partial r}\right|_{r=0} = 0 \text{ and } T_i\big|_{r=a} = T_\infty. \tag{C.7}$$

The layers are assumed to be in perfect thermal contact denoted by the continuity of temperature and heat flux,

$$T_1 = T_2 \; ; \; k_1 \frac{\partial T_1}{\partial z} = k_2 \frac{\partial T_2}{\partial z} \text{ at } z = H_1 \tag{C.8}$$

and $$T_2 = T_3 \; ; \; k_2 \frac{\partial T_2}{\partial z} = k_3 \frac{\partial T_3}{\partial z} \text{ at } z = H_2. \tag{C.9}$$

The solution to the two-dimensional, transient heat conduction problem described above is obtained using Green's functions. In order to simplify the solution procedure, a variable transformation is first performed

$$\breve{T} = T - T_\infty. \tag{C.10}$$

This transformation shifts the temperature at the diaphragm edge to zero, thus making all the boundary conditions homogenous.

Green's Function Solution Technique

The use of Green's function for solving non-homogenous, transient heat conduction problems with energy generation, non-homogenous boundary and initial conditions can be found in several references (Morse and Feshback 1953, Carslaw and Jaeger 1986, Beck et al. 1992, Ozisik 1993). In this section the technique is used to solve a two-dimensional, transient heat conduction problem with internal energy generation in a three-layer composite medium. In order to define a Green's function the following auxiliary problem is considered in the same region

$$\alpha_i\left(\nabla^2 G_i+\frac{1}{k}\delta\left(r-r'\right)\delta\left(z-z'\right)\delta\left(t-\tau\right)\right)=\frac{\partial G_i}{\partial t}\qquad t>\tau \quad \text{(C.11)}$$

with the requirement that $G_i=0$ for $t<\tau$ known as the causality condition (Morse and Feshback 1953). This is similar to Equation (C.1) except the source term in Equation (C.11) is represented by a delta function that defines a line source located at (r',z') releasing its energy instantaneously at $t=\tau$. The boundary conditions are the homogenous versions of the original problem. In this case, they are similar to Equations (C.6) - (C.9),

$$\left.\frac{\partial G_1}{\partial z}\right|_{z=0}=0\,,\ \left.\frac{\partial G_3}{\partial z}\right|_{z=H_3}=0,$$

$$\left.\frac{\partial G_i}{\partial r}\right|_{r=0}=0\,,\ G_i\big|_{r=a}=0,$$

$$G_1=G_2\ ;\quad k_1\frac{\partial G_1}{\partial z}=k_2\frac{\partial G_2}{\partial z}\ \text{ at }\ z=H_1,$$

and

$$G_2=G_3\ ;\ k_2\frac{\partial G_2}{\partial z}=k_3\frac{\partial G_3}{\partial z}\ \text{ at }\ z=H_2.$$

The function $G_i\left(r,z,t\middle|r',z',\tau\right)$ satisfying the auxiliary problem (Equation (C.11)) is referred to as the Green's function for the two-dimensional transient heat conduction

problem described by Equations (C.1) - (C.3). The physical significance of the Green's function is that it represents the temperature at any location (r, z) and at time t due to an instantaneous source at (r', z') releasing its energy at $t=\tau$, in a region that is initially ($t<\tau$) at zero temperature and with homogenous boundary conditions. The elegance of this technique is that the solution to the original problem can be represented entirely in terms of the Green's function and the same function can be used to handle additional non-homogeneities arising from the boundary or initial conditions provided the geometry of the problem remains unaltered. Therefore, once the Green's function is known, the temperature distribution in the region can be readily computed.

The derivation of the temperature distribution or in other words the derivation of the solution to the non-homogenous transient heat conduction problem in terms of the Green's function can be found in several references (Morse and Feshback 1953, Carslaw and Jaeger 1986, Beck et al. 1992, Ozisik 1968) and is presented here for the case of a three-dimensional problem with non-homogenous boundary conditions and internal heat generation (the derivation has been adapted from Ozisik (1968)). The governing equations satisfied by T (Equations (C.1) - (C.3)) and G (Equation (C.11)) are expressed as functions of $\boldsymbol{r}'$ and τ,

$$\nabla'^2 T + \frac{1}{k} g(\boldsymbol{r}', \tau) = \frac{1}{\alpha}\frac{\partial T}{\partial \tau}, \quad \tau < t, \tag{C.12}$$

and

$$\nabla'^2 G + \frac{1}{\alpha}\delta(\boldsymbol{r}' - \boldsymbol{r})\delta(\tau - t) = -\frac{1}{\alpha}\frac{\partial G}{\partial \tau} \qquad \tau > t, \tag{C.13}$$

where $\boldsymbol{r}'$ is a three dimensional spatial vector defining the location of the source. The negative sign in right-hand side of Equation (C.13) is a result of the causality condition

and the Laplacian operator is with respect to $\boldsymbol{r}'$. Multiplying Equation (C.12) by *G* and Equation (C.13) by *T* and subtracting gives

$$\left(G\nabla'^2T - T\nabla'^2G\right) + \frac{1}{k}g(\boldsymbol{r}',\tau)G - \frac{1}{\alpha}\delta\left(\boldsymbol{r}'-\boldsymbol{r}\right)\delta\left(\tau-t\right)T = \frac{1}{\alpha}\frac{\partial\left(GT\right)}{\partial\tau}. \tag{C.14}$$

The resulting equation is then integrated with respect to the spatial variables $\boldsymbol{r}'$ and with respect to the time variable τ over the interval 0 to *t*

$$\int_\tau d\tau \int_R \left(G\nabla'^2T - T\nabla'^2G\right)d\boldsymbol{r}' + \frac{1}{k}\int_\tau d\tau \int_R g(\boldsymbol{r}',\tau)G\,d\boldsymbol{r}' - \frac{1}{\alpha}\int_\tau \delta\left(\tau-t\right)d\tau$$
$$\cdot \int_R \delta\left(\boldsymbol{r}'-\boldsymbol{r}\right)T\,d\boldsymbol{r}' = \frac{1}{\alpha}\int_R \left[GT\right]_0^t\, d\boldsymbol{r}'. \tag{C.15}$$

The volume integral in Equation (C.15) is replaced by a surface integral via Green's theorem

$$\int_R \left(G\nabla'^2T - T\nabla'^2G\right)\,d\boldsymbol{r}' = \int\left(G\,\frac{\partial T}{\partial n_l} - T\,\frac{\partial G}{\partial n_l}\right)\,ds, \tag{C.16}$$

where $\partial/\partial n_l$ represents differentiation along a direction normal to the boundary surface *l*. The term involving delta functions can be simplified to

$$\int_\tau \delta\left(\tau-t\right)\,d\tau \int_R \delta\left(\boldsymbol{r}'-\boldsymbol{r}\right)\,T\left(\boldsymbol{r}',\tau\right)\,d\boldsymbol{r}' = T\left(\boldsymbol{r},t\right), \tag{C.17}$$

and evaluating the term on the right-hand side at the limits gives

$$\left[GT\right]_0^t = -G\big|_{\tau=0}\;T\big|_{\tau=0} = -G\big|_{\tau=0}\;F\left(\boldsymbol{r}'\right) \tag{C.18}$$

since [*GT*] vanishes at $t=\tau$. In Equation (C.18) ***F(r')*** represents an arbitrary initial condition. Thus the solution to a three-dimensional, non-homogenous, transient heat conduction problem with heat generation and non-homogenous boundary and initial conditions can be expressed in terms of Green's function as

$$T(\mathbf{r},t) =$$

$$\int G\big|_{\tau=0} F(\mathbf{r}')\, d\mathbf{r}' + \frac{\alpha}{k}\iint g(\mathbf{r}',\tau)\, G\, d\mathbf{r}' d\tau + \alpha \iint \left(G\,\frac{\partial T}{\partial n_i} - T\,\frac{\partial G}{\partial n_i} \right) ds\, d\tau, \quad \text{(C.19)}$$

where the first term on the right-hand side is the contribution of the initial condition and the second and third terms represent contributions from the energy generation and non-homogenous boundary conditions. For the case of a composite region the Green's function G is replaced by G_{ij}, where i represents a layer in the composite (Figure C-1) and j represents the contribution of the non-homogenous terms in the layers. For example, G_{12} represents the Green's function in layer 1 due to an impulsive source in layer 2 or in other words the temperature distribution in layer 1 due to an impulsive source in layer 2. Thus, for a two-dimensional transient heat conduction problem in a three-layer composite slab with energy generation in layer 1, zero initial condition and homogenous boundary conditions the solution is of the form (Ozisik 1993)

$$T_i(r,z,t) = \int_{\tau=0}^{t} \partial\tau \int_{r'}\int_{z'} G_{i1}\left(r,z,t\middle|r',z',\tau\right)\frac{\alpha_1}{k_1}\, g(r',z',\tau)\, r'\, dr'\, dz'. \quad \text{(C.20)}$$

The next step in the solution procedure is to determine the analytical form of the Green's function. Several techniques have been reported in the literature for determining Green's functions including Laplace transforms, method of images and separation of variables (Morse and Feshback 1953, Ozisik 1968, Carslaw and Jaeger 1986, Beck et al. 1992). This analysis is based on the separation of variables technique adapted from Ozisik (1968). Separation of variables is a commonly used technique for solving homogenous transient heat conduction problems subject to a prescribed initial condition and it has been shown by Ozisik (1993) that the solution to the homogenous problem can be rearranged to obtain the Green's function at $\tau = 0$, $G\left(r,z,t\middle|r',z',0\right)$. Additionally, by

replacing *t* with *(t-τ)* in the homogenous solution, the Green's function for the non-homogenous transient heat conduction problem can be obtained. Thus the Green's function solution technique requires the solution to the homogenous heat conduction problem in the composite medium described by

$$\alpha_i \nabla^2 \theta_i(r,z,t) = \frac{\partial \theta_i(r,z,t)}{\partial t}, \quad i = 1,2,3, \tag{C.21}$$

with homogenous versions of the boundary conditions described by Equations (C.6) - (C.9),

$$\left.\frac{\partial \theta_1}{\partial z}\right|_{z=0} = 0\,,\ \left.\frac{\partial \theta_3}{\partial z}\right|_{z=H_3} = 0, \tag{C.22}$$

$$\left.\frac{\partial \theta_i}{\partial r}\right|_{r=0} = 0\,,\ \theta_i(a) = 0, \tag{C.23}$$

$$\theta_1 = \theta_2\ ; \quad k_1 \frac{\partial \theta_1}{\partial z} = k_2 \frac{\partial \theta_2}{\partial z} \text{ at } z = H_1, \tag{C.24}$$

and

$$\theta_2 = \theta_3\ ; \quad k_2 \frac{\partial \theta_2}{\partial z} = k_3 \frac{\partial \theta_3}{\partial z} \text{ at } z = H_2, \tag{C.25}$$

and a constant initial condition of $\theta(0) = \theta_o$ throughout the region. To solve Equation (C.21) analytically, it is first simplified by reducing the number of independent variables to two, such that $\theta = \theta(z,t)$. The *r* variable is eliminated via the application of finite Hankel transform (Sneddon 1951) on the governing equation and the boundary conditions. The transformed equations are then solved using separation of variables.

Finite Hankel Transform

The technique of finite Hankel transform is used to eliminate the *r* variable from Equation (C.21) thus reducing the number of independent variables. The Hankel transform and its inverse pair are mathematically defined as

$$\bar{\theta}\left(\varepsilon,z,t\right)=\int_0^a r\,\theta\left(r,z,t\right)J_o\left(\varepsilon_m r\right)dr \tag{C.26}$$

and

$$\theta_i\left(r,z,t\right)=\frac{2}{a^2}\sum_m \bar{\theta}_i\,\frac{J_o\left(\varepsilon_m r\right)}{\left[J_1\left(\varepsilon_m a\right)\right]^2}, \tag{C.27}$$

where ε_m are roots of $J_o\left(\varepsilon_m a\right)=0$ and is based on the radial boundary conditions for the problem. The transformed Laplacian operator in *r*, ∇_r^2 is reduced to

$$\int_0^a r\left(\frac{\partial^2\theta}{\partial r^2}+\frac{1}{r}\frac{\partial\theta}{\partial r}\right)J_o\left(\varepsilon_m r\right)dr=-\varepsilon_m^2\bar{\theta} \tag{C.28}$$

for a boundary condition of $\theta(r=a)=0$. Rewriting Equation (C.21) in terms of the transformed variable $\bar{\theta}\left(\varepsilon,z,t\right)$ gives

$$-\varepsilon_m^2\alpha_i\,\bar{\theta}_i+\alpha_i\frac{\partial^2\bar{\theta}_i}{\partial z^2}=\frac{\partial\bar{\theta}_i}{\partial t}. \tag{C.29}$$

Equation (C.29) can now be solved using the separation of variables technique.

Assuming $\bar{\theta}_i\left(\varepsilon,z,t\right)=Z_i\left(z\right)\Gamma\left(t\right)$, the separated equation is of the form

$$\alpha_i\left(\frac{1}{Z_i}\frac{\partial^2 Z_i}{\partial z^2}-\varepsilon_m^2\right)=\frac{1}{\Gamma}\frac{\partial\Gamma}{\partial t}=-\lambda^2. \tag{C.30}$$

where λ is the separation constant. The solution for $\Gamma\left(t\right)$ is of the form

$$\Gamma\left(t\right)=c_1\,e^{-\lambda^2 t} \tag{C.31}$$

and $Z_i\left(\lambda,\varepsilon,z\right)$ satisfies the following eigenvalue problem

$$\frac{\partial^2 Z_i}{\partial z^2}+\left(\frac{\lambda^2}{\alpha_i}-\varepsilon_m^2\right)Z_i=0, \tag{C.32}$$

subject to

$$\frac{\partial Z_1}{\partial z}=0 \text{ at } z=0, \tag{C.33}$$

$$Z_1=Z_2;\quad k_1\frac{\partial Z_1}{\partial z}=k_2\frac{\partial Z_2}{\partial z} \text{ at } z=H_1, \tag{C.34}$$

$$Z_2=Z_3;\quad k_2\frac{\partial Z_2}{\partial z}=k_3\frac{\partial Z_3}{\partial z} \text{ at } z=H_2, \tag{C.35}$$

and $$\frac{\partial Z_3}{\partial z} = 0 \text{ at } z = H_3. \quad \text{(C.36)}$$

The general solution to the eigenvalue problem is

$$Z_{inm}(z) = A_{inm} \sin\left(\frac{\lambda_{nm}^2}{\alpha_i} - \varepsilon_m^2\right)^{\frac{1}{2}} z + B_{inm} \cos\left(\frac{\lambda_{nm}^2}{\alpha_i} - \varepsilon_m^2\right)^{\frac{1}{2}} z, \quad i = 1,2,3, \quad \text{(C.37)}$$

where *i* is an individual layer of the composite, $Z_{inm} \equiv Z_i(\lambda_{nm}, z)$ and the subscript *nm* implies an infinite number of discrete eigenvalues $\lambda_{1m} < \lambda_{2m} < \lambda_{3m} < \ldots \lambda_{nm}$ for every value of ε_m $(\varepsilon_1 < \varepsilon_2 < \ldots \varepsilon_m)$ and corresponding eigenfunctions Z_{inm}. The six coefficients ($A_{1,2,3}$ and $B_{1,2,3}$) in Equation (C.37) are determined from the six boundary and interface conditions. However, the coefficients can be determined only as a multiple of an arbitrary constant, since the system of equations (Equations (C.33) - (C.36)) is homogenous. The transcendental equation for the determination of the eigenvalues λ_{nm} results from the requirement of a non-trivial solution for the system of homogenous equations. The eigenvalues are therefore obtained by setting the determinant of the coefficients $A_{1,2,3}$ and $B_{1,2,3}$ equal to zero. Substituting the eigenfunction into Equation (C.33) results in

$$A_{1nm} \cos\left(\left(\frac{\lambda^2}{\alpha_1} - \varepsilon_m^2\right)^{\frac{1}{2}} 0\right)\left(\frac{\lambda^2}{\alpha_1} - \varepsilon_m^2\right)^{\frac{1}{2}} - B_{1nm} \sin\left(\left(\frac{\lambda^2}{\alpha_1} - \varepsilon_m^2\right)^{\frac{1}{2}} 0\right)\left(\frac{\lambda^2}{\alpha_1} - \varepsilon_m^2\right)^{\frac{1}{2}} = 0, \quad \text{(C.38)}$$

which implies $A_{1nm} = 0$. We set $B_{1nm} = 1$ and solve for the other coefficients in terms of B_1. Substituting the eigenfunction into the interface continuity conditions at $z = H_1$ (Equation (C.34)) for temperature and heat flux gives

$$(1)\cos\left(\left(\frac{\lambda^2}{\alpha_1}-\varepsilon_m^2\right)^{\frac{1}{2}}H_1\right)=A_{2nm}\sin\left(\left(\frac{\lambda^2}{\alpha_2}-\varepsilon_m^2\right)^{\frac{1}{2}}H_1\right)+B_{2nm}\cos\left(\left(\frac{\lambda^2}{\alpha_2}-\varepsilon_m^2\right)^{\frac{1}{2}}H_1\right),$$

(C.39)

and

$$-k_{12}\sin\left(\left(\frac{\lambda^2}{\alpha_1}-\varepsilon_m^2\right)^{\frac{1}{2}}H_1\right)=A_{2nm}\cos\left(\left(\frac{\lambda^2}{\alpha_2}-\varepsilon_m^2\right)^{\frac{1}{2}}H_1\right)-B_{2nm}\sin\left(\left(\frac{\lambda^2}{\alpha_2}-\varepsilon_m^2\right)^{\frac{1}{2}}H_1\right)$$

(C.40)

respectively, where $k_{12}=k_1\left(\frac{\lambda^2}{\alpha_1}-\varepsilon_m^2\right)^{\frac{1}{2}}\Big/k_2\left(\frac{\lambda^2}{\alpha_2}-\varepsilon_m^2\right)^{\frac{1}{2}}$. Similarly, substituting the eigenfunction into the interface continuity conditions at $z=H_2$ (Equation (C.35)) gives

$$A_{2nm}\sin\left(\left(\frac{\lambda^2}{\alpha_2}-\varepsilon_m^2\right)^{\frac{1}{2}}H_2\right)+B_{2nm}\cos\left(\left(\frac{\lambda^2}{\alpha_2}-\varepsilon_m^2\right)^{\frac{1}{2}}H_2\right)=$$
$$A_{3nm}\sin\left(\left(\frac{\lambda^2}{\alpha_3}-\varepsilon_m^2\right)^{\frac{1}{2}}H_2\right)+B_{3nm}\cos\left(\left(\frac{\lambda^2}{\alpha_3}-\varepsilon_m^2\right)^{\frac{1}{2}}H_2\right)$$

(C.41)

and

$$k_{23}\left[A_{2nm}\cos\left(\left(\frac{\lambda^2}{\alpha_2}-\varepsilon_m^2\right)^{\frac{1}{2}}H_2\right)-B_{2nm}\sin\left(\left(\frac{\lambda^2}{\alpha_2}-\varepsilon_m^2\right)^{\frac{1}{2}}H_2\right)\right]=$$
$$A_{3nm}\cos\left(\left(\frac{\lambda^2}{\alpha_3}-\varepsilon_m^2\right)^{\frac{1}{2}}H_2\right)-B_{3nm}\sin\left(\left(\frac{\lambda^2}{\alpha_3}-\varepsilon_m^2\right)^{\frac{1}{2}}H_2\right),$$

(C.42)

where $k_{23}=k_2\left(\frac{\lambda^2}{\alpha_2}-\varepsilon_m^2\right)^{\frac{1}{2}}\Big/k_3\left(\frac{\lambda^2}{\alpha_3}-\varepsilon_m^2\right)^{\frac{1}{2}}$. The boundary condition at $z=H_3$ gives

$$A_{3nm}\cos\left(\left(\frac{\lambda^2}{\alpha_3}-\varepsilon_m^2\right)^{\frac{1}{2}}H_3\right)-B_{3nm}\sin\left(\left(\frac{\lambda^2}{\alpha_3}-\varepsilon_m^2\right)^{\frac{1}{2}}H_3\right)=0. \quad \text{(C.43)}$$

Equations (C.38) - (C.43) can be represented in matrix form

$$[M]\begin{bmatrix}B_1=1\\A_2\\B_2\\A_3\\B_3\end{bmatrix}=\begin{bmatrix}0\\0\\0\\0\\0\end{bmatrix} \quad \text{(C.44)}$$

where

$$[M]=\begin{bmatrix}
\cos\left(\left(\frac{\lambda^2}{\alpha_1}-\varepsilon_m^2\right)^{\frac{1}{2}}H_1\right) & -\sin\left(\left(\frac{\lambda^2}{\alpha_2}-\varepsilon_m^2\right)^{\frac{1}{2}}H_1\right) & -\cos\left(\left(\frac{\lambda^2}{\alpha_2}-\varepsilon_m^2\right)^{\frac{1}{2}}H_1\right) & 0 & 0\\
-k_{12}\sin\left(\left(\frac{\lambda^2}{\alpha_1}-\varepsilon_m^2\right)^{\frac{1}{2}}H_1\right) & -\cos\left(\left(\frac{\lambda^2}{\alpha_2}-\varepsilon_m^2\right)^{\frac{1}{2}}H_1\right) & \sin\left(\left(\frac{\lambda^2}{\alpha_2}-\varepsilon_m^2\right)^{\frac{1}{2}}H_1\right) & 0 & 0\\
0 & \sin\left(\left(\frac{\lambda^2}{\alpha_2}-\varepsilon_m^2\right)^{\frac{1}{2}}H_2\right) & \cos\left(\left(\frac{\lambda^2}{\alpha_2}-\varepsilon_m^2\right)^{\frac{1}{2}}H_2\right) & -\sin\left(\left(\frac{\lambda^2}{\alpha_3}-\varepsilon_m^2\right)^{\frac{1}{2}}H_2\right) & -\cos\left(\left(\frac{\lambda^2}{\alpha_3}-\varepsilon_m^2\right)^{\frac{1}{2}}H_2\right)\\
0 & k_{23}\cos\left(\left(\frac{\lambda^2}{\alpha_2}-\varepsilon_m^2\right)^{\frac{1}{2}}H_2\right) & -k_{23}\sin\left(\left(\frac{\lambda^2}{\alpha_2}-\varepsilon_m^2\right)^{\frac{1}{2}}H_2\right) & -\cos\left(\left(\frac{\lambda^2}{\alpha_3}-\varepsilon_m^2\right)^{\frac{1}{2}}H_2\right) & \sin\left(\left(\frac{\lambda^2}{\alpha_3}-\varepsilon_m^2\right)^{\frac{1}{2}}H_2\right)\\
0 & 0 & 0 & \cos\left(\left(\frac{\lambda^2}{\alpha_3}-\varepsilon_m^2\right)^{\frac{1}{2}}H_3\right) & -\sin\left(\left(\frac{\lambda^2}{\alpha_3}-\varepsilon_m^2\right)^{\frac{1}{2}}H_3\right)
\end{bmatrix}. \quad \text{(C.45)}$$

The complete solution for the transformed variable $\bar{\theta}$ in any layer *i* is then constructed as

$$\bar{\theta}_i\left(\varepsilon_m,z,t\right)=\sum_n C_{nm}\,e^{-\lambda_{nm}^2 t}\,Z_i\left(z\right), \quad \text{(C.46)}$$

which satisfies the differential Equation (C.29) and the boundary conditions and it is further constrained to satisfy the initial condition

$$\bar{\theta}_o\left(\varepsilon_m,z\right)=\sum_n C_{nm}\,Z_i\left(z\right). \quad \text{(C.47)}$$

The constant C_{nm} is obtained by using the orthogonality relation of the eigenfunctions and is of the form

$$C_{nm}=\frac{1}{N_n}\sum_i\frac{k_i}{\alpha_i}\int_{z_i}^{z_{i+1}}Z_i\left(z\right)\bar{\theta}_o\,dz, \quad \text{(C.48)}$$

where

$$N_n = \frac{k_1}{\alpha_1}\int_0^{H_1} Z_1^2(z')\,dz' + \frac{k_2}{\alpha_2}\int_{H_1}^{H_2} Z_2^2(z')\,dz' + \frac{k_3}{\alpha_3}\int_{H_2}^{H_3} Z_3^2(z')\,dz'. \quad \text{(C.49)}$$

Taking the inverse Hankel transform, defined by

$$\theta_i(r,z,t) = \frac{2}{a^2}\sum_m \bar{\theta}_i \frac{J_o(\varepsilon_m r)}{J_1^2(\varepsilon_m a)}$$

of Equation (C.46) gives the homogenous temperature distribution $\theta(r,z,t)$ as

$$\theta_i(r,z,t) = \frac{2}{a^2}\sum_m\sum_n \frac{J_o(\varepsilon_m r)}{J_1^2(\varepsilon_m a)}\frac{1}{N_n} e^{-\lambda_{nm}^2 \cdot t} Z_i(z)$$
$$\cdot\ \theta_o \int_0^a r' J_o(\varepsilon_m r')\,dr' \left[\frac{k_1}{\alpha_1}\int_0^{H_1} Z_1(z')\,dz' + \frac{k_2}{\alpha_2}\int_{H_1}^{H_2} Z_2(z')\,dz' + \frac{k_3}{\alpha_3}\int_{H_2}^{H_3} Z_3(z')\,dz'\right] \quad \text{(C.50)}$$

The solution of the homogenous problem define by Equation (C.21) can now be expressed in terms of Green's functions as

$$\theta_i(r,z,t) = \int_{z'=0}^{H_1}\int_{r'=0}^{a} G_{i1}(r,z,t|r',z',\tau)_{\tau=0}\, F_1(r',z')\,dr'\,dz' +$$
$$\int_{z'=H_1}^{H_2}\int_{r'=0}^{a} G_{i2}(r,z,t|r',z',\tau)_{\tau=0}\, F_2(r',z')\,dr'\,dz' + \int_{z'=H_2}^{H_3}\int_{r'=0}^{a} G_{i3}(r,z,t|r',z',\tau)_{\tau=0}\, F_3(r',z')\,dr'\,dz'. \quad \text{(C.51)}$$

where $F_i(r,z)$ is the initial condition in a given layer. Comparing Equation (C.51) with Equation (C.50) we can extract the Green's function for the non-homogenous problem

$$G_{i1}(r,z,t|r',z',\tau) = \sum_m\sum_n \frac{k_1}{\alpha_1}\,\frac{2}{a^2}\frac{r' J_o(\varepsilon_m r')}{J_1^2(\varepsilon_m a)}\,\frac{Z_1(z')}{N(\lambda_{nm})} J_o(\varepsilon_m r) Z_i(z) e^{-\lambda_{nm}^2(t-\tau)}.$$

Using the Green's function the steady-state temperature distribution in the individual layers of the composite diaphragm resulting from the time-harmonic joule heating of the diffused heater is evaluated using Equation (C.20) as

$$T_i(r,z,t) = \mathrm{Re}\left(\sum_m \sum_n g_o \frac{b}{\varepsilon_m} J_1(\varepsilon_m b) \int_{H_{heat}}^{H_1} Z_1(z')\, dz' \; \frac{2\, J_o(\varepsilon_m r)}{a^2\, J_1^2(\varepsilon_m a)} \; \frac{Z_i(z)}{N(\lambda_{nm})} \left(\frac{e^{j\omega t}}{\lambda_{nm}^2 + j\omega} \right) \right) \tag{C.52}$$

where a and b are the radius of the diaphragm and the heater, respectively, g_o (W/m^3) is the magnitude of the heat source [£], λ_{nm} and ε_m are eigenvalues, J_o and J_1 are Bessel functions of the first kind, ω is the frequency of the time-harmonic heat source. Once the unsteady temperature field is known, the integrated thermal forces and moments can be computed.

In the following sections, the transverse vibration of the composite diaphragm resulting from the time-varying two-dimensional temperature distribution is derived.

Plate Analysis

The equilibrium equations for any radial section of the axisymmetric plate (Figure C-2) are given by (Timoshenko and Woinowsky-Krieger 1959, Leissa 1993, Reddy 1996)

$$\frac{\partial}{\partial r}(N_r) + \frac{1}{r}(N_r - N_\theta) = 0 \tag{C.53}$$

$$\frac{\partial}{\partial r}(M_r) - Q_r + \frac{1}{r}(M_r - M_\theta) = 0 \tag{C.54}$$

and

$$\frac{1}{r}\frac{\partial}{\partial r}(rQ_r) - N_o \frac{1}{r}\frac{\partial}{\partial r}\left(r\frac{\partial w}{\partial r} \right) = \rho_A \ddot{w}, \tag{C.55}$$

where $\ddot{w} = \partial^2 w / \partial t^2$, N_r and N_θ are force resultants (Figure C-2) in the radial and circumferential directions

$$N_r = \int_z \sigma_r\, dz\,; \quad N_\theta = \int_z \sigma_\theta\, dz. \tag{C.56}$$

Similarly, M_r and M_θ are the moment resultants (Figure C-2)

[£] A joule heat fraction of 1 was assumed in the thermomechanical model, i.e., the thermal power was set equal to the electrical power I^2R.

$$M_r = \int_z \sigma_r \, z \, dz \; ; \quad M_\theta = \int_z \sigma_\theta \, z \, dz, \tag{C.57}$$

Q_r is the transverse shear force resultant (Figure C-2)

$$Q_r = \int_{z_1} \tau_{rz} \, dz, \tag{C.58}$$

and ρ_A is the areal density (kg/m^2) of the composite plate

$$\rho_A = \int_z \rho \, dz. \tag{C.59}$$

In the equations of motion only the inertial term associated with the transverse acceleration of the plate has been retained and the initial in-plane compressive force, $N_r = N_\theta = N_o$, is assumed to be much larger than the incremental forces induced by the deflection of the plate.

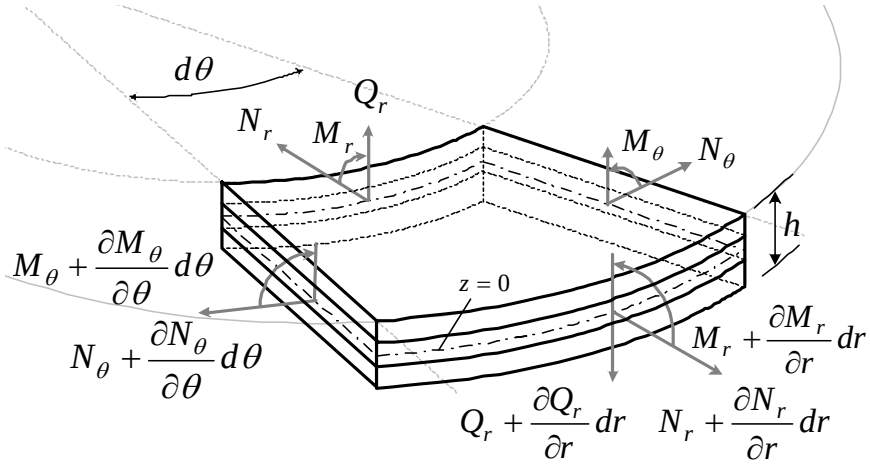

Figure C-2: Force and moment resultants on an element of the circular plate.

The radial and transverse displacements based on Kirchoff's plate theory are

$$u(r,z,t) = u_o(r,t) - z\frac{\partial w}{\partial r} \tag{C.60}$$

and

$$w(r,z,t) = w_o(r,t), \tag{C.61}$$

where the radial displacement *u* is a linear function of the axial coordinate *z* and the transverse displacement *w* is independent of thickness. The subscript "o" denotes

reference plane values. The radial and circumferential strain-displacement relationship can then be expressed as

$$\varepsilon_{rr} = \varepsilon_{rr}^{o} + z\,\kappa_r \tag{C.62}$$

and

$$\varepsilon_{\theta\theta} = \varepsilon_{\theta\theta}^{o} + z\,\kappa_\theta, \tag{C.63}$$

where κ_r and κ_θ are the radial and circumferential curvatures

$$\kappa_r = -\frac{\partial^2 w}{\partial r^2}$$

and

$$\kappa_\theta = -\frac{1}{r}\frac{\partial w}{\partial r}.$$

The strains in the reference plane $(z = 0)$ are

$$\varepsilon_{rr}^{o} = \frac{\partial u_o}{\partial r}$$

and

$$\varepsilon_{\theta\theta}^{o} = \frac{u_o}{r}.$$

The thermoelastic stress-strain relationships for a transversely isotropic, linear elastic material are

$$\begin{Bmatrix} \sigma_{rr} \\ \sigma_{\theta\theta} \end{Bmatrix} = \begin{bmatrix} Q_{11} & Q_{12} \\ Q_{12} & Q_{22} \end{bmatrix} \left(\begin{Bmatrix} \varepsilon_{rr}^{o} \\ \varepsilon_{\theta\theta}^{o} \end{Bmatrix} + z \begin{Bmatrix} \kappa_r \\ \kappa_\theta \end{Bmatrix} - T(r,z,t) \begin{Bmatrix} \gamma_r \\ \gamma_\theta \end{Bmatrix} \right), \tag{C.64}$$

where [Q] is the material stiffness matrix, $\gamma = \gamma_r = \gamma_\theta$ is the coefficient of thermal expansion and $T(r,z,t)$ is the non-uniform temperature distribution. For a transversely isotropic material the stiffness matrix is

$$[Q] = \frac{E}{1-\nu^2} \begin{bmatrix} 1 & \nu \\ \nu & 1 \end{bmatrix},$$

where E is the Young's modulus and ν is the Poisson's ratio distributions in the composite plate. The force and moment resultants are obtained by integrating the constitutive relations (Equation (C.64)) through the thickness of the composite plate and are given by

$$\begin{Bmatrix} N_r \\ N_\theta \end{Bmatrix} = [A]\begin{Bmatrix} \varepsilon^o_{rr} \\ \varepsilon^o_{\theta\theta} \end{Bmatrix} + [B]\begin{Bmatrix} \kappa_r \\ \kappa_\theta \end{Bmatrix} - \begin{Bmatrix} N^T_r \\ N^T_\theta \end{Bmatrix} \tag{C.65}$$

and

$$\begin{Bmatrix} M^T_r \\ M^T_\theta \end{Bmatrix} = [B]\begin{Bmatrix} \varepsilon^o_{rr} \\ \varepsilon^o_{\theta\theta} \end{Bmatrix} + [D]\begin{Bmatrix} \kappa_r \\ \kappa_\theta \end{Bmatrix} - \begin{Bmatrix} M^T_r \\ M^T_\theta \end{Bmatrix}, \tag{C.66}$$

where $[A] = \int_z [Q]\,dz$ is the extensional stiffness matrix, $[B] = \int_z [Q]\,z\,dz$ is the flexural-extensional coupling matrix and $[D] = \int_z [Q]\,z^2\,dz$ is the flexural stiffness matrix. The thermoelastic coupling generates both a thermal force

$$\begin{bmatrix} N^T_r \\ N^T_\theta \end{bmatrix} = \int_z \gamma\, T(r,z,t)[Q]\,dz \tag{C.67}$$

and a thermal moment

$$\begin{bmatrix} M^T_r \\ M^T_\theta \end{bmatrix} = \int_z \gamma\, T(r,z,t)[Q]\,z\,dz. \tag{C.68}$$

The governing displacement equations are derived by substituting the strain-displacement relations (Equations (C.62) and (C.63)) and the constitutive relations (Equations (C.65) and (C.66)) into the Equations of motion (Equations (C.53) - (C.55)). The resulting equations in terms of the radial and transverse displacements are of the form:

$$A_{11}\left\{\frac{\partial^2 u_o}{\partial r^2} + \frac{1}{r}\frac{\partial u_o}{\partial r} - \frac{u_o}{r^2}\right\} - B_{11}\left\{\frac{\partial^3 w}{\partial r^3} + \frac{1}{r}\frac{\partial^2 w}{\partial r^2} - \frac{1}{r^2}\frac{\partial w}{\partial r}\right\} = \frac{\partial}{\partial r}\left(N^T_r\right) \tag{C.69}$$

and

$$B_{11}\left\{\frac{\partial^3 u_o}{\partial r^3} + \frac{2}{r}\frac{\partial^2 u_o}{\partial r^2} - \frac{1}{r^2}\frac{\partial u_o}{\partial r} + \frac{u_o}{r^3}\right\} - D_{11}\left\{\frac{\partial^4 w}{\partial r^4} + \frac{2}{r}\frac{\partial^3 w}{\partial r^3} - \frac{1}{r^2}\frac{\partial^2 w}{\partial r^2} + \frac{1}{r^3}\frac{\partial w}{\partial r}\right\}$$
$$- N_o\left(\frac{\partial^2 w}{\partial r^2} + \frac{1}{r}\frac{\partial w}{\partial r}\right) = \frac{\partial^2}{\partial r^2}\left(M^T_r\right) + \frac{1}{r}\frac{\partial}{\partial r}\left(M^T_r\right) + \rho_A \ddot{w}. \tag{C.70}$$

Replacing u_o in Equation (C.70) with *w* from Equation (C.69) and simplifying results in a governing equation exclusively in terms of the transverse displacement *w*

$$D^{*}\nabla^{4}w+N_{o}\nabla^{2}w+\rho_{A}\ddot{w}=\frac{B_{11}}{A_{11}}\left(\nabla^{2}N_{r}^{T}\right)-\left(\nabla^{2}M_{r}^{T}\right), \qquad \text{(C.71)}$$

where $D^{*}=D_{11}-\frac{B_{11}^{2}}{A_{11}}$. Equation (C.71) represents the thermally forced vibration of the composite plate where the forcing functions arise from the non-uniform temperature and material property distributions in the plate. The general solution to Equation (C.71) consists of two parts, a complementary solution to the homogenous part of the equation and a particular solution satisfying the forcing functions. The forcing functions are derived from the temperature field

$$T_{i}\left(r,z,t\right)=\mathrm{Re}\left(\sum_{m}\sum_{n}g_{o}\ f\left(\lambda_{nm},\varepsilon_{m}\right)\ e^{j\omega t}\ J_{o}\left(\varepsilon_{m}r\right)Z_{i}\left(z\right)\right) \qquad \text{(C.72)}$$

where

$$f\left(\lambda_{nm},\varepsilon_{m}\right)=\left(\frac{1}{\lambda_{nm}^{2}+j\omega}\right).\left(\frac{2b\,J_{1}\left(\varepsilon_{m}b\right)}{a^{2}\,\varepsilon_{m}\ J_{1}^{2}\left(\varepsilon_{m}a\right)}\right)\left(\frac{1}{N\left(\lambda_{nm}\right)}\int_{H_{heater}}^{H_{1}}Z_{1}\left(z'\right)dz'\right). \qquad \text{(C.73)}$$

The generated thermal force and moment according to Equations (C.67) and (C.68) are

$$N_{r}^{T}\left(r,t\right)=\sum_{m}\sum_{n}g_{o}\ f\left(\lambda_{nm},\varepsilon_{m}\right)\ e^{j\omega t}\ J_{o}\left(\varepsilon_{m}r\right)\left(\sum_{i}\int_{H_{i-1}}^{H_{i}}\gamma_{i}\left(Q_{11}^{(i)}+Q_{12}^{(i)}\right)Z_{i}\left(z\right)dz\right) \qquad \text{(C.74)}$$

and

$$M_{r}^{T}\left(r,t\right)=\sum_{m}\sum_{n}g_{o}\ f\left(\lambda_{nm},\varepsilon_{m}\right)e^{j\omega t}\ J_{o}\left(\varepsilon_{m}r\right)\ \left(\sum_{i}\int_{H_{i-1}}^{H_{i}}\gamma_{i}\left(Q_{11}^{(i)}+Q_{12}^{(i)}\right)Z_{i}\left(z\right)z\,dz\right). \qquad \text{(C.75)}$$

Therefore the governing equation is of the form,

$$\nabla^{4}w+\frac{N_{o}}{D^{*}}\nabla^{2}w+\frac{\rho_{A}}{D^{*}}\ddot{w}=\sum_{m}\sum_{n}\frac{1}{D^{*}}\zeta\left(\lambda_{nm},\varepsilon_{m}\right)\ e^{j\omega t}\ J_{o}\left(\varepsilon_{m}r\right) \qquad \text{(C.76)}$$

where

$$\zeta\left(\lambda_{nm},\varepsilon_m\right)=\varepsilon_m^2\ f\left(\lambda_{nm},\varepsilon_m\right)g_o\left(\begin{array}{l}\left(\sum_i\int_{H_{i-1}}^{H_i}\gamma_i\left(Q_{11}^{(i)}+Q_{12}^{(i)}\right)Z_i\left(z\right)z\,dz\right)-\\ \frac{B_{11}}{A_{11}}\left(\sum_i\int_{H_{i-1}}^{H_i}\gamma_i\left(Q_{11}^{(i)}+Q_{12}^{(i)}\right)Z_i\left(z\right)dz\right)\end{array}\right). \tag{C.77}$$

Assuming a harmonic time-dependence for the plate deflection, of the form

$$w\left(r,t\right)=\mathrm{Re}\left(w(r)\,e^{j\omega t}\right), \tag{C.78}$$

results in a differential equation in terms of the spatial coordinates

$$\nabla^4 w(r)+\frac{N_o}{D^*}\nabla^2 w(r)-\frac{\rho_A\,\omega^2}{D^*}\,w(r)=\frac{1}{D^*}\sum_m\sum_n\zeta\left(\lambda_{nm},\varepsilon_m\right)J_o\left(\varepsilon_m r\right). \tag{C.79}$$

The homogenous part of the governing Equation (C.79) can be expressed as

$$\left(\nabla^2-\xi^2\right)\left(\nabla^2+\psi^2\right)w=0, \tag{C.80}$$

where

$$\xi^2=\frac{N_o}{2D^*}\left[\sqrt{1+\frac{4\rho_A\omega^2D^*}{N_o^2}}-1\right] \tag{C.81}$$

and

$$\psi^2=\frac{N_o}{2D^*}\left[\sqrt{1+\frac{4\rho_A\omega^2D^*}{N_o^2}}+1\right]. \tag{C.82}$$

The complete solution to the homogenous equation is obtained by superimposing the solutions to the equations

$$\left(\nabla^2+\psi^2\right)w_1=0 \tag{C.83}$$

and

$$\left(\nabla^2-\xi^2\right)w_2=0. \tag{C.84}$$

Equations (C.83) and (C.84) represent the 0^{th} order Bessel's equation and Modified Bessel's equation respectively and have general solutions of the form

$$w_1\left(r\right)=c_1\,J_o\left(\psi r\right)+c_2\,Y_o\left(\psi r\right) \tag{C.85}$$

and

$$w_2\left(r\right)=c_3\,I_o\left(\xi r\right)+c_4\,K_o\left(\xi r\right). \tag{C.86}$$

Thus the complementary solution to Equation (C.79) is of the form

$$w(r) = c_1 J_o(\psi r) + c_2 Y_o(\psi r) + c_3 I_o(\xi r) + c_4 K_o(\xi r). \qquad \text{(C.87)}$$

In order to satisfy the forcing functions, a particular solution, of the form

$$w_p(r) = c_5 J_o(\varepsilon_m r) \qquad \text{(C.88)}$$

is assumed, where c_5 is an arbitrary constant. The particular solution is then substituted into Equation (C.79) and simplified to solve for the constant c_5

$$c_5 = \sum_m \sum_n \frac{1}{D^*} \frac{\zeta(\lambda_{nm}, \varepsilon_m)}{\varepsilon_m^4 - \frac{N_o}{D^*}\varepsilon_m^2 - \xi^2\psi^2}. \qquad \text{(C.89)}$$

Therefore, the general solution to Equation (C.79) is

$$w(r) = c_1 J_o(\psi r) + c_2 Y_o(\psi r) + c_3 I_o(\xi r) + c_4 K_o(\xi r) + \sum_m \sum_n \frac{1}{D^*} \frac{\zeta(\lambda_{nm}, \varepsilon_m)}{\varepsilon_m^4 - \frac{N_o}{D^*}\varepsilon_m^2 - \xi^2\psi^2} J_o(\varepsilon_m r). \qquad \text{(C.90)}$$

The four constants are solved using plate boundary conditions that consist of finite values at the center and clamped conditions at the edge,

$$w(0) < \infty; \quad \left.\frac{\partial w}{\partial r}\right|_{r=0} < \infty, \qquad \text{(C.91)}$$

and

$$w(a) = 0; \quad \left.\frac{\partial w}{\partial r}\right|_{r=a} = 0, \qquad \text{(C.92)}$$

Substituting the governing equation into the boundary conditions results in the following expression for the transverse deflection of the composite plate

$$w(r,t) = \mathrm{Re}\left(\left[c_1 J_o(\psi r) + c_3 I_o(\xi r) + \sum_m \sum_n \frac{1}{D^*} \frac{\zeta(\lambda_{nm}, \varepsilon_m)}{\varepsilon_m^4 - \frac{N_o}{D^*}\varepsilon_m^2 - \xi^2\psi^2} J_o(\varepsilon_m r) \right] e^{j\omega t} \right),$$

where

$$c_1 = -c_3 \left(\frac{I_o(\xi a)}{J_o(\psi a)} \right) - \sum_m \sum_n \frac{1}{D^*} \left(\frac{\zeta(\lambda_{nm}, \varepsilon_m)}{\varepsilon_m^4 - \frac{N_o}{D^*}\varepsilon_m^2 - \xi^2\psi^2} \right) \left(\frac{J_o(\varepsilon_m a)}{J_o(\psi a)} \right) \qquad \text{(C.93)}$$

and

$$c_3 = \sum_m \sum_n \frac{1}{D^*} \left(\frac{\zeta\left(\lambda_{nm}, \varepsilon_m\right)}{\varepsilon_m^4 - \frac{N_o}{D^*}\varepsilon_m^2 - \xi^2 \psi^2} \right) \left(\frac{J_o\left(\psi a\right) J_1\left(\varepsilon_m a\right) \varepsilon_m - J_o\left(\varepsilon_m a\right) J_1\left(\psi a\right) \psi}{I_o\left(\xi a\right) J_1\left(\psi a\right) \psi + J_o\left(\psi a\right) I_1\left(\xi a\right) \xi} \right). \tag{C.94}$$

APPENDIX D
SENSOR PACKAGE

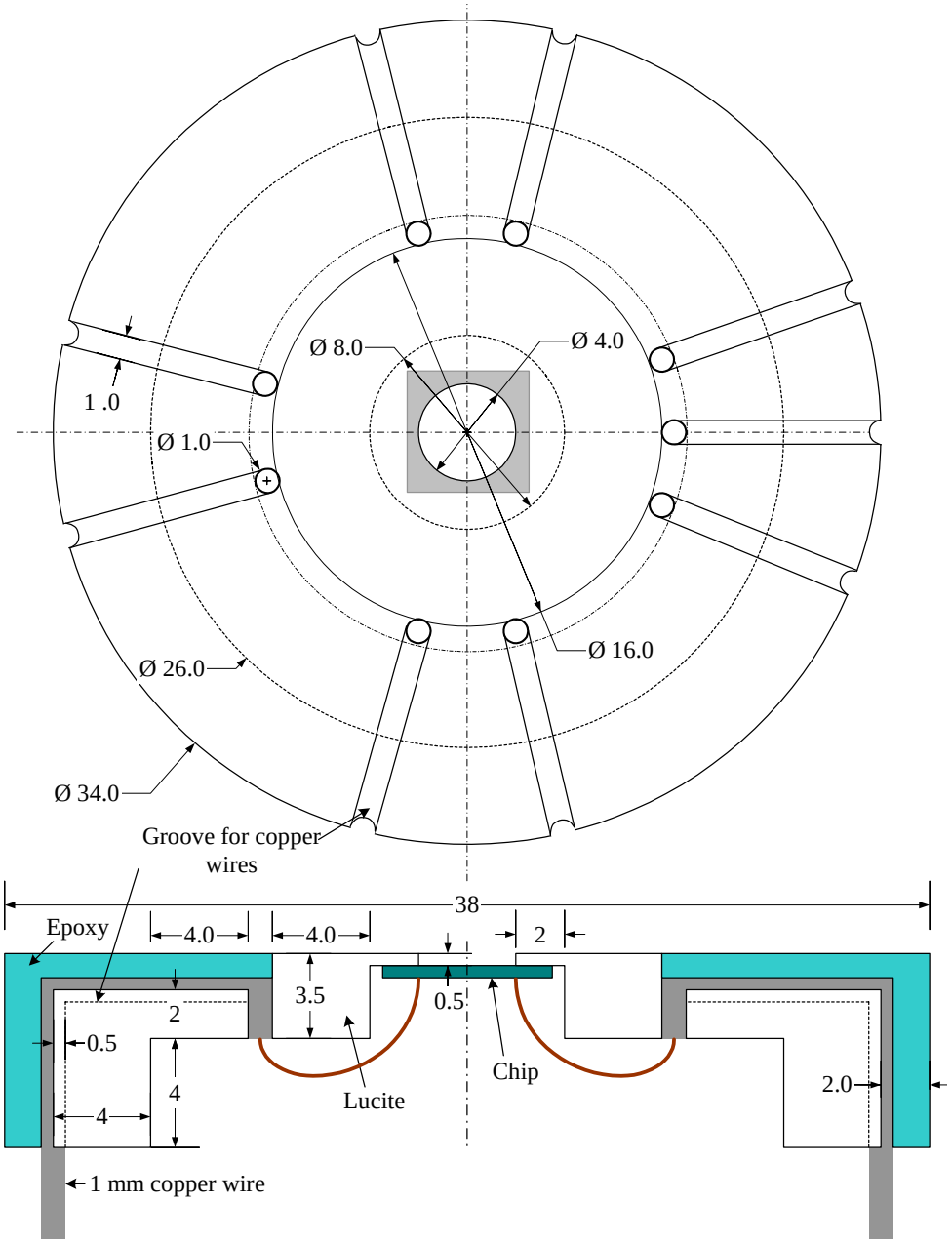

Figure D-1: Lucite package for the acoustic proximity sensor to enable testing of the integrated sensor/ETWI (all dimensions are in *mm*).

LIST OF REFERENCES

Al Sarawi, S. F., Abbott, D., and Franzon, P. D., “A Review of 3-D Packaging Technology,” *IEEE Transactions on Components Packaging and Manufacturing Technology: Part B-Advanced Packaging*, vol. 21, pp. 2-14, 1998.

Antonelli, L., Walsh, K., and Alberg, A., “Laser Interrogation of the Air-Water Interface for In-Water Sound Detection: Initial Feasibility Tests,” *138th Meeting of the Acoustical Society of America*, Columbus, OH, 1999.

Ashley, S., "Warp Drive Underwater," *Scientific American*, vol. 284, pp. 70-79, 2001.

Arnold, D. P., Nishida, T., Cattafesta, L., and Sheplak, M., "MEMS-Based Acoustic Array Technology," *Journal of the Acoustical Society of America*, vol.113, no.1, pp. 289-298, 2002.

Barshan, B., "Fast Processing Techniques for Accurate Ultrasonic Range Measurement," *Measurement Science and Technology*, vol. 11, pp. 45-50, 2000.

Batchelor, G. K., *An Introduction to Fluid Dynamics*, Cambridge University Press, New York, pp. 485, 1967.

Beck, J. V., Cole, K. D., Haji-Sheikh, A., and Litkouhi, B., *Heat Conduction using Green's Functions*, Hemisphere, Washington D.C, 1992.

Bernstein, J., Finberg, S., Houston, K., Niles, L., Chen, H., Cross, L., Li, K., and Udayakumar, K., "Integrated Ferroelectric Monomorph Transducers for Acoustic Imaging," *ISAF '96, Proceedings of the Tenth IEEE International Symposium on Applications of Ferroelectrics*, vol. 1, pp. 19-26, 1996.

Bernstein, J. J., Finberg, S. L., Houston, K., Niles, L. C., Chen, H. D., Cross, L. E., Li, K. K., and Udayakumar, K., "Micromachined High Frequency Ferroelectric Sonar Transducers," *IEEE Transactions on Ultrasonics, Ferroelectrics and Frequency Control*, vol. 44, no. 5, pp. 960-969, 1997.

Bernstein, J. J., Bottari, J., Houston, K., Kirkos, G., Miller, R., Xu, B., Ye, Y., and Cross, L. E., "Advanced MEMS Ferroelectric Ultrasound 2D Arrays," *IEEE Ultrasonics Symposium*, vol. 2, pp. 1145-1153, 1999.

Bernstein, J. J., Bottari, J., Houston, K., Kirkos, G., Miller, R., Xu, B., Ye, Y. and Cross, L. E., "High Sensitivity MEMS Ultrasound Arrays by Lateral Ferroelectric Polarization," *Solid-State Sensor and Actuator Workshop*, Hilton Head, SC, pp. 281-284, 2000.

Bhardwaj, S., "Noise Measurements in Silicon Piezoresistors for S/N Optimization of Piezoresistive MEMS Microphones," M.S Thesis, Electrical and Computer Engineering, University of Florida, Gainesville, FL, 2001.

Blackstock, D. T., *Fundamentals of Physical Acoustics*, Wiley Interscience, New York, NY, 2000.

Brand, O., Baltes, H., and Baldenweg, U., "Membrane Resonators in Bipolar and CMOS IC Technology," *Transducers '93, International Conference on Solid-State Sensors and Actuators*, pp. 646-649, 1993.

Brand, O., Baltes, H., and Baldenweg, U., "Ultrasound Transducers using Membrane Resonators Realized with Bipolar IC Technology," *Microelectromechanical Systems '94*, pp. 33-38, 1994.

Brand, O., Hornung, M., Baltes, H., and Hafner, C., "Ultrasound Barrier Microsystem for Object Detection Based on Micromachined Transducer Elements," *Journal of Microelectromechanical Systems*, vol. 6, no. 2, pp. 151-160, 1997.

Brand, O., and Baltes, H., "Micromachined Resonant Sensor: An Overview," *Sensors Update*, vol. 4, VCH-Wiley, Weinheim, 1997.

Brantley, W. A., "Calculated Elastic Constants for Stress Problems Associated with Semiconductor Devices," *Journal of Applied Physics*, vol. 44, pp. 534-535, 1973.

Brysek, J., Petersen, K., Mallon, J. R., Christel, L., and Pourahmadi, F., "Silicon Sensors and Microstructures: A First Effort to Integrate an Interdisciplinary Body of Material on Silicon Sensor and Microstructure Technology," *NovaSensor*, 1988.

Carslaw, H. S., and Jaeger, J. C., *Conduction of Heat in Solids*, Oxford University Press, London, 1986.

Chandrasekaran, V., Cain, A., Nishida, T., and Sheplak, M., "Dynamic Calibration Technique for Thermal Shear Stress Sensors with Variable Mean Flow," *38th Aerospace Sciences Meeting and Exhibition*, Reno, NV, 2000.

Chandrasekaran, V., Chow, E. M., Kenny, T. W., Nishida, T., and Sheplak, M., “Through Wafer Electrical Interconnects For MEMS Sensors,” *Proceedings of the ASME*, November 11-16, New York, 2001.

Chandrasekaran, V., Chow, E. M., Kenny, T. W., Nishida, T., Sankar, B. V., Cattafesta, L. N., and Sheplak, M., "Thermoelastically Actuated Acoustic Proximity Sensor with Integrated Electrical Through-Wafer Interconnects," *Solid-State Sensor and Actuator Workshop*, Hilton Head, SC, pp. 102-107, 2002.

Chow, E. M., Soh, H. T., Partridge, A., Harley, J. A., Kenny, T. W., Quate, C. F., Abdollahi-Alibeik, S., McVittie, J. P., and McCarthy, A., "Fabrication of High-Density Cantilever Arrays and Through-Wafer Interconnects," *Solid-State Sensor and Actuator Workshop*, Hilton Head, SC, pp. 220-224, 1998.

Chow, E. M., Soh, H. T., Lee, H. C., Adams, J. D., Minne, S. C., Yaralioglu, G., Atalar, A., Quate, C. F., and Kenny, T. W., "Integration of Through-Wafer Interconnects with a Two-Dimensional Cantilever Array," *Sensors and Actuators A*, vol. A83, no. 1-3, pp. 118-123, 2000.

Chow, E. M., Chandrasekaran, V., Partridge, A., Nishida, T., Sheplak, M., Quate, C. F., and Kenny, T. W., "Process Compatible Polysilicon-Based Electrical Through-Wafer Interconnects in Silicon Substrates," *Journal of Microelectromechanical Systems*, vol. 11, no. 1057-7157, pp. 631-640, 2002.

Christensen, C., Kersten, P., Henke, S., and Bouwstra, S., "Wafer Through-Hole Interconnections with High Vertical Wiring Densities," *IEEE Transactions on Components, Packaging, and Manufacturing Technology, Part A*, vol. 19, no. 4, pp. 516-522, 1996.

Gerlach, G., Schroth, A., and Pertsch, P., "Influence of Clamping Conditions on Microstructure Compliance," *Sensors and Materials*, vol. 8, no. 2, pp. 79-98, 1996.

Goldberg, H. D., Breuer, K. S., and Schmidt, M. A., "A Silicon Wafer-Bonding Technology for Microfabricated Shear-Stress Sensors with Backside Contacts," *Solid-State Sensor and Actuator Workshop*, Hilton Head, SC, pp. 111-115, 1994.

Gururaj, S., "Design of a Piezoresistive Pressure Sensor with In-Plane Compressive Stresses and Diffused Resistors," M.S Thesis, Mechanical and Aerospace Engineering, University of Florida, Gainesville, FL, 2003.

Harley, J. A., and Kenny, T. W., "1/f Noise Considerations for the Design and Process Optimization of Piezoresistive Cantilevers," *Journal of Microelectromechanical Systems*, vol. 9, no. 2, pp. 226-235, 2000.

Heschel, M., Kuhmann, J. F., Bouwstra, S., and Amskov, M., “Stacking Technology for a Space Constrained Microsystem,” *Journal of Intelligent Material Systems and Structures*, vol. 9, pp. 749-54, 1998.

Hornung, M., Brand, O., Paul, O., and Baltes, H., "Ultrasound Transducer for Distance Measurements," *Tranducers '97, International Conference on Solid-State Sensors and Actuators*, pp. 441-444, 1997.

Hornung, M., Brand, O., Paul, O., and Baltes, H., "Long-Term Stability of Membrane Transducers for Proximity Sensing," *Proceedings of the SPIE - The International Society for Optical Engineering*, pp. 251-259, 1998.

Hornung, M. R., and Brand, O., *Micromachined Ultrasound-Based Proximity Sensors*, Kluwer Academic Publishers, Boston, MA, 1999.

Irie, T., and Yamada, G., "Thermally Induced Vibration of Circular Plate," *Bulletin of the Japan Society of Mechanical Engineers*, vol. 21, no. 162, pp. 1703-1709, 1978.

Jin, X., Ladabaum, I., and Khuri-Yakub, B. T., "The Microfabrication of Capacitive Ultrasonic Transducers," *Journal of Microelectromechanical Systems*, vol. 7, no. 3, pp. 295-302, 1998.

Jin, X. C., Degertekin, F. L., Calmes, S., Zhang, X. J., Ladabaum, I., and Khuri-Yakub, B. T., "Micromachined Capacitive Transducer Arrays for Medical Ultrasound Imaging," *IEEE Ultrasonics Symposium*, vol. 2, pp. 1877-1880, 1998.

Jin, X., Ladabaum, I., Degertekin, F. L., Calmes, S., Khuri-Yakub, B. T., "Fabrication and Characterization of Surface Micromachined Capacitive Ultrasonic Immersion Transducers," *Journal of Microelectromechanical Systems*, vol. 8, no. 1, pp. 100-114, 1999.

Kamins, T. I., "Design Properties of Polycrystalline Silicon (For Sensor Application)," *Sensors and Actuators A (Physical)*, vol. A23, no. 1-3, pp. 817-824, 1990.

Kanda, Y., "A Graphical Representation of the Piezoresistance Coefficients in Silicon," *IEEE Transactions on Electron Devices*, vol. ED-29, no. 1, pp. 64-70, 1982.

Kerr, D. R., and Milnes, A. G., "Piezoresistance of Diffused Layers in Cubic Semiconductors," *Journal of Applied Physics*, vol. 34, no. 4, pp. 727-731, 1963.

Lammerink, T. S. J., Elwenspoek, M., Van Ouwerkerk, R. H., Bouwstra, S., and Fluitman, J. H. J., "Performance of Thermally Excited Resonators," *Sensors and Actuators A*, vol. 21-23, pp. 352-356, 1990.

Lammerink, T. S. J., Elwenspoek, M., and Fluitman, J. H. J., "Thermal Actuation of Clamped Silicon Microbeams," *Sensors and Materials*, vol. 3, pp. 217-238, 1992.

Law, M. E., and Cea, S. M., "Continuum Based Modeling of Silicon Integrated Circuit Processing: An Object Oriented Approach," *Computational Materials Science*, vol. 12, no. 4, pp. 289-308, 1998.

Lecoffre, Y., *Cavitation Bubble Trackers*, A.A. Balkema, Brookfield, VT, 1999.

Leissa, A., *Vibrations of Plates*, Acoustical Society of America, 1993.

Li, X., Lasson, E., Sheplak, M., and Li, J., "Phase-Shift Based Time Delay Estimators for Proximity Acoustic Sensors," *IEEE Journal of Oceanic Engineering*, vol. 27, no. 1, pp. 47-56, 2002.

Li, X., Wu, R., Sheplak, M., and Li, J., "Multifrequency CW-Based Time-Delay Estimation for Proximity Ultrasonic Sensors," *IEE Proceedings - Radar, Sonar, and Navigation*, vol. 149, no. 2, pp. 53-59, 2002.

Linder, S., Baltes, H., Gnaedinger, F., and Doering, E., "Fabrication Technology for Wafer Through-Hole Interconnections and Three-Dimensional Stacks of Chips and Wafers," *Proceedings IEEE Micro Electro Mechanical Systems, An Investigation of Micro Structures, Sensors, Actuators, Machines and Robotic Systems*, pp. 349-354, 1994.

Lynnworth, L. C., Nguyen, T. H., Smart, C. D., and Khrakovsky, O. A., "Acoustically Isolated Paired Air Transducers for 50-, 100-, 200-, or 500-kHz Applications," *IEEE Transactions on Ultrasonics, Ferroelectrics, and Frequency Control*, vol. 44, no. 5, pp. 1087-1100, 1997.

Madou, M. J., *Fundamentals of Microfabrication*, CRC Press, Boca Raton, FL, 1997.

Manthey, W., Kroemer, N., and Magori, V., "Ultrasonic Transducers and Transducer Arrays for Application in Air," *Measurement Science and Technology*, vol. 3, pp. 249-261, 1992.

Massa, D. P., "Choosing an Ultrasonic Sensor for Proximity or Distance Measurement," *Sensor Magazine*, vol. 16, no. 2, 1999.

Mason, W. P., Forst, J. J., and Tornillo, L. M., "Recent Developments in Semiconductor Strain Transducers," *Proceedings of the Instrumentation Society of America, 15th Annual Conference*, pp. 110-120, 1962.

Mockl, T., Magori, V., and Eccardt, C., "Sandwich-Layer Transducer-A Versatile Design for Ultrasonic Transducers Operating in Air," *Sensors and Actuators A*, vol. 21-23, pp. 687-692, 1990.

Morse, P. M., and Feshback, H., *Methods of Theoretical Physics*, McGraw-Hill, New York, 1953.

Motorola, *Sensor Device Data/Handbook*, Phoenix, AZ: Motorola, Inc., fourth edition, 1998.

Ozisik, M. N., *Boundary Value Problems of Heat Conduction*, Dover Publications, Inc., New York, 1968.

Ozisik, M. N., *Heat Conduction*, Wiley Interscience, New York, 1993.

Papila, M., Haftka, R. T., Nishida, T., and Sheplak, M., "Piezoresistive Microphone Design Pareto Optimization: Tradeoff between Sensitivity and Noise Floor," *AIAA Paper 2003-1632*, Norfolk, VA, pp. 2003.

Paul, O., and Baltes, H., "Mechanical Behavior and Sound Generation Efficiency of Thermomechanically Driven Multilayered, Prestressed, Elastically Clamped Plates," *Journal of Micromechanics and Microengineering*, vol. 9, no. 1, pp. 19-29, 1999.

Pfann, W. G., and Thurston, R. N., "Semiconducting Stress Transducers Utilizing the Transverse and Shear Piezoresistance Effect," *Journal of Applied Physics*, vol. 32, pp. 2008-2019, 1961.

Pierret, R. F., *Semiconductor Device Fundamentals*, Addison-Wesley Publishing Company Inc., New York, NY, 1996.

Reddy, J. N., *Mechanics of Laminated Composite Plates: Theory and Analysis*, CRC Press, Boca Raton, FL, 1996

Rossi, M., *Acoustics and Electroacoustics*, Artech House, Norwood, MA, 1988.

Scheeper, P. R., Olthuis, W., and Bergveld, P., "A Review of Silicon Microphones," *Sensors and Actuators A*, vol. 44, pp. 1-11, 1994.

Senocak, I., "Computational Methodology for the Simulation of Turbulent Cavitating Flows," Ph.D. Dissertation, Department of Mechanical and Aerospace Engineering, University of Florida, Gainesville, FL, 2002.

Senturia, S. D., *Microsystem Design*, Kluwer Academic Publishers, MA, 2001.

Sheplak, M., Breuer, K. S., and Schmidt, M. A., "A Wafer-Bonded, Silicon-Nitride Membrane Microphone with Dielectrically-Isolated, Single-Crystal Silicon Piezoresistors," *Solid-State Sensor and Actuator Workshop*, Hilton Head, SC, pp. 23-26, 1998.

Sheplak, M., and Dugundji, J., "Large Deflections of Clamped Circular Plates under Initial Tension and Transitions to Membrane Behavior," *Journal of Applied Mechanics*, vol. 65, pp. 107-115, 1998.

Sleva, M. Z., Briggs, R. D., and Hunt, W. D., "A Micromachined Poly(vinylidene Fluoride-Trifluorethylene) Transducer for Pulse-Echo Ultrasound Applications," *IEEE Transactions on Ultrasonics, Ferroelectrics, and Frequency Control*, vol. 43, no. 2, pp. 257-262, 1996.

Sleva, M. Z., Hunt, W. D., and Briggs, R. D., "Focusing Performance of Epoxy- and Air-Backed Polyvinylidene Fluoride Fresnel Zone Plates," *Journal of the Acoustical Society of America*, vol. 96, no. 3, pp. 1627-1633, 1994.

Smith, C. S., "Piezoresistance Effect in Germanium and Silicon," *Physical Review*, vol. 94, no. 42-49, 1954.

Sneddon, I. N., *Fourier Transforms*, McGraw Hill, New York, 1951.

Soderkvist, J., and Lindberg, U., "Characteristics of Quasi Buckling," *Sensors and Materials*, vol. 6, no. 5, pp. 293-309, 1994.

Soh, H. T., Yue, C. P., McCarthy, A., Ryu, C., Lee, T. H., Wong, S. S., and Quate, C. F., "Ultra-Low Resistance, Through-Wafer Via (TWV) Technology and its Applications in Three Dimensional Structures on Silicon," *Japanese Journal of Applied Physics, Part 1 (Regular Papers, Short Notes & Review Papers)*, vol. 38, no. 4B, pp. 2393-2396, 1999.

Stemme, G., "Resonant Silicon Sensors," *Journal of Micromechanics and Microengineering*, vol. 1, pp. 113-125, 1991.

Sze, S. M., *Semiconductor Sensors*, Wiley-Interscience, New York, NY, 1994.

Timoshenko, S., and Woinowsky-Krieger, S., *Theory of Plates and Shells*, McGraw-Hill, New York, 1959.

Tolstoy, I., and Clay, C. S., *Ocean Acoustics*, Acoustical Society of America, 1987.

Tufte, O. N., Chapman, P. W., and Long, D., "Silicon Diffused Element Piezoresistive Diaphragms," *Journal of Applied Physics*, vol. 33, pp. 3322-3327, 1962.

Tufte, O. N., and Long, D., "Recent Developments in Semiconductor Piezoresistive Devices," *Solid-State Electronics*, vol. 6, pp. 323-338, 1963.

Tufte, O. N., and Stelzer, E. L., "Piezoresistive Properties of Silicon Diffused Layers," *Journal of Applied Physics*, vol. 34, no. 2, pp. 313-318, 1963.

Williams, E. G., *Fourier Acoustics*, Academic Press, New York, 1999.

Wu, J. H., Del Alamo, J. A., and Jenkins, K. A., "A High Aspect-Ratio Silicon Substrate-Via Technology and Applications: Through-Wafer Interconnects for Power and Ground and Faraday Cages for SOC Isolation," *IEDM 2000, International Electron Devices Meeting*, pp. 477-480, 2000.

BIOGRAPHICAL SKETCH

Venkataraman Chandrasekaran received a B.E. degree in mechanical engineering from Annamalai University, Tamil Nadu, India, and a M.S. degree in aerospace engineering from the University of Florida, Gainesville, FL, in 1998 and 2000 respectively. He is currently a doctoral student in the Department of Mechanical and Aerospace Engineering at the University of Florida. His graduate research on micromachined devices focuses on electroacoustic transducers and shear-stress sensors. His master's thesis involved the characterization of a micromachined thermal shear stress sensor, including a novel in-situ dynamic calibration technique using acoustic plane waves. His dissertation focuses on the development of a first generation MEMS-based acoustic proximity sensor with integrated electrical through-wafer interconnects for backside contacts.